UPC   CTTC

Numerical simulation of frost growth and densification using deformable and static grids

Heat and Mass Technological Centre
Departament de Màquines i Motors Tèrmics
Universitat Politècnica de Catalunya

Eduard Bartrons Casademont
Doctoral Thesis

Numerical simulation of frost growth and densification using deformable and static grids

Eduard Bartrons Casademont

PHD THESIS

submitted to the

Departament de Màquines i Motors Tèrmics
E.S.E.I.A.A.T.
Universitat Politècnica de Catalunya

in partial fulfillment of the requirements for the degree of

Doctor of Philosophy in Thermal Engineering of the Universitat Politècnica de Catalunya

Terrassa, Juliol 2018

Numerical simulation of frost growth and densification using deformable and static grids

Eduard Bartrons Casademont

Thesis Supervisor

Dr. Carlos D. Pérez-Segarra

Thesis Co-Director

Dr. Pedro A. Galione

Committee Board

Dr. Antonio Lecuona-Neumann
Universidad Carlos III de Madrid

Dr. Joaquim Rigola
Universitat Politècnica de Catalunya

Dr. Federico Favre
Universidad de la República

External Referees

Dr. Ricardo Vinuesa
Linné FLOW Centre, KTH Royal Institute of Technology

Dr. Sean Lovett
Schlumberger Cambridge Research

Dedico la tesi

a la meva mare, al meu pare,

a la Nona i a l'avi,

a l'Àlex i al meu germà,

i a la Jorgina.

Let us now deal with the most remarkable conditions which are produced in and around the earth, summarizing them in the barest outline. There are two kinds of exhalation which rise continually from the earth into the air above us, composed of small particles and entirely invisible, except that sometimes in the mornings they are seen rising from rivers and streams. Of these one kind being given off from the earth is dry and resembles smoke, while the other being exhaled from the element of moisture is damp and vaporous. From the latter are produced mist and dew and the various forms of frost, clouds and rain and snow and hail; . . . Dew is moisture of fine composition falling from a clear sky; ice is water congealed in a condensed form from a clear sky; hoar-frost is congealed dew, and dew-frost is dew which which is half congealed.

Aristotle, 4th century BC.

ii

Agraïments

Vull utilitzar aquestes línies per recordar les peripècies viscudes els darrers anys de doctorat. Aquestes, juntament amb la gent que hi ha estat involucrada, han estat les que m'han permès desenvolupar-me personal i professionalment.

Després de renunciar a emprendre el doctorat als Estats Units per enyorança a Barcelona i l'Empordà, vaig assegurar una posició a Londres a un any vista. Recordo que en David em va fer una de les cartes de recomanació que ho va fer possible. Al cap d'uns mesos, l'amor va fer que decidís quedar-me i intentar realitzar el doctorat a Catalunya. Sempre recordaré l'escalfor que em van transmetre en David i l'Assensi en aquella primera reunió, i en la que des d'un primer moment em van voler acollir al CTTC.

Els primers sis mesos de doctorat van ser emocionants. Vaig conèixer el Kike, amb qui vam aprendre junts les bases dels mètodes numèrics i del CFD. Entremig va arribar l'Ali, recent sortit del forn en temes d'occident. Amb ells dos ràpidament vam generar una amistat que ara veig infracturable.

Em va "tocar" el despatx 313, pertanyent al 3r pis del TR5. És el pis del bosc tropical, en el qual, en certs períodes de l'any, tocava treure el matxet per fer-se pas cap al bany. Al 313 he compartit despatx amb en Ramiro i l'Octavi de llavors ençà. Ells han estat els informàtics que m'han ajudat i donat totes les eines necessàries per fer-me la vida més fàcil durant els últims quatre anys.

Aquell primer estiu vam marxar amb la Jorgina a voltar el sud-est asiàtic, i després de molta feina i il·lusió, començàrem a viure junts al carrer més alegre de Barcelona.

El 2015 va ser un any de lectura bibliogràfica, i amb una part important de desenvolupament en temes de programació. En Carles em va facilitar llibres de referència del camp de la tranferència de calor, amb infinitat de correlacions empíriques. Amb en Giorgos vam crear la base dels solvers implícits a *TermoFluids*, i en Chiva es va oferir sempre, incondicionalment, a resoldre els dubtes que m'anaven sorgint.

Entre cafès i converses una mica pujades de to que compartiem entre els companys del lab (les de l'Héctor eren sempre, sens dubte, les guanyadores), va arribar el dia en què marxàrem a Crackòvia. Per uns quants era la nostra primera ponència en un congrés internacional. Podria escriure un llibre sencer de les aventures que vam viure amb l'Assensi, en Muela, el Fede, l'Ivette, el Néstor, el Firas i l'Ali, entre altres. I en especial dels últims dies extres que vam viure a Varsòvia amb l'Eugenio i el Kike.

Poc després vaig començar a interactuar amb el Pedro, i mig any més tard vaig anar a Montevideo. Vam fer molta feina, i molts *asados*! Sempre recordaré les cerveses amb el Dani, el teatre Solís amb l'Ana, les converses de meteorologia amb en Pisio, i l'accent forçat català d'en Pedro Curto. I la Sole i la pitita, l'Aina, amb qui vaig poder compartir moments molt especials.

Vaig presentar la feina feta a Uruguay a Denver, Colorado, aquell mateix juny de 2017. Va ser la culminació del doctorat, el moment en què vaig veure que la cova tenia sortida, i que en podia entreveure ja la llum. Al congrés vaig conèixer un munt de gent, en especial l'Albert, en Periklis i la Lima. A la casa d'estil victorià on estava instal·lat hi vivia l'Ian, amb qui vam crear un lligam molt estret: segurament gràcies al Bluegrass Festival de Telluride, i posterior tornada a Denver en aquell Nissan Rogue, per les Muntanyes Rocoses, amb *pull over* inclòs de la policía estatal. I és clar, tot això després d'estar un setmana caminant entre parcs nacionals i dormint al sac..

A final d'any vaig fer la maleta, i a principi de gener de 2018 vaig marxar a Cambridge, UK, on vaig realitzar una altra estada de col·laboració, amb el professor Nikos Nikiforakis. Al Laboratory for Scientific Computing hi vaig conèixer el Sean, en Tomé, en Knut, el Lukas, en Nandan i en Murray, entre altres. Recordo molt bé els passejos a Granchester amb la Celsa, en bicicleta, i les pintes del Blue Ball Inn, protegit sota la pluja, les finestres enteladas i els gossos ajaguts davant la roent llar de foc. Els *brunch* de *networking* dels diumenges a Selwyn, i l'encant de conte de la ciutat.

De tornada a Barcelona vaig trobar el meu estimat estudi a Gràcia, on després de poc més d'un mes hi vaig poder anar a viure, i disfrutar de les vistes amb els amics. El Chaco, que sempre m'ha recolzat i qui m'ha donat un cop de mà amb l'anglès, el Jaume, l'amic i veí a qui sempre li agrairé l'ajuda que em va donar el temps d'obres, i el Joan, que sempre m'ha sabut fer tocar de peus a terra.

Vaig tornar de visita a Montevideo mentres acabava d'escriure la tesi. Quan sorgien problemes de LaTeX, el Guillem, amb qui hem compartit moltes converses de ciència ficció, d'astronomia i de física en general, era la persona que me'ls resolia.

Han passat anys. Incontables converses d'aeroacústica del Jesús, les ajudes del Nacho en temes de malla mòbil. Sant Joans a Sant Pol de Mar a casa la Gina, anades i vingudes al Mas i a Menorca. Grans viatges a París, Turquia, Creta i Iran.. Molts sopars a Can Punyetes amb en Ramon, les visites d'en Pierre, cafès amb la Nina, casoris com el de la Nora i l'Octavi, i les centenars pujades a la Mola de dinars ràpids. Això sí, la que les ha englobat a totes i cada una d'elles, queda tancada amb la culminació d'aquesta tesi. I és per això que us agraeixo, a tots els que hi sou mencionats, haver pogut compartir aquests moments amb mi.

Abstract

The present thesis aims at developing a basis for the numerical simulation of the growth and densification of macroscopic frost sheets. Notwithstanding the fact that icing has still a long way to fully understand its physics, this work is potentially important, since a broad range of empirical correlations as well as the implementation of formerly neglected physical effects are studied herewith. In particular, this research is focused on developing methodologies for three-dimensional meshes, capable to predict the frost growth and densification of complex geometries. In addition, it is important to mention that within the *Heat and Mass Transfer Technological Center* (CTTC) research group, this thesis is the first attempt of modelling this phenomenon from a multi-dimensional aspect.

This work comprises five chapters. The first one is an introduction to icing and frost formation. The main motives that urge to numerically simulate frosting are detailed. Moreover, the different methods and approaches to model frosting are presented. From these, the main objectives and outline of the thesis are derived.

The next two chapters are the core of this dissertation, which comprehend the two developed methods. In particular, the contents of these two chapters have been submitted or published in international journals and conferences. Hence, they are written to be self-contained and only minor changes have been introduced with respect to the original papers. Consequently, some theoretical and numerical contents, as the definition of some thermo-physical properties, are repeated.

In detail, the second chapter introduces a model that simulates the frost growth and densification using a moving mesh method. First, the most relevant empirical correlations used to describe the frost layer conductivity and diffusivity among others are tested by means of parametric studies. A thorough discussion on the performance of such parameters is made, emphasizing the fact of using diffusion resistance factors above 1.0 in order to capture the frost growth. The best-fitted solutions validate the model input combinations which give good agreements against experimental data under certain experimental conditions. Furthermore, the method is tested against a 2D numerical case, highlighting the main advantages of using a deformable grid, i.e. the accurate tracking of the air-frost interface.

The third chapter introduces a fixed-grid-porous-media method capable of simulating the growth and densification of frost sheets. In pursuance of finding out possible explanations to the needed artificially enhanced diffusion resistance factors, a velocity field is calculated across all the domain. A porous media treatment is given to the frost layer, whereas the transported temperature and vapour density are used to define the thermophysical state of each cell, which might enable phase change. The method is tested with a study case of a duct flow with a non-homogeneously cooled lower boundary. The influence of accounting for the convection, as well as the

enhanced diffusion resistance factors within the frost layer, are studied.

The last two chapters contain the concluding remarks, as well as ideas on how the present work could be continued. At the end, there are two appendices including material which may be useful in order to follow some parts of this work. It has been placed apart so that the normal reading of the thesis is not disturbed.

Contents

List of Figures

List of Tables

Nomenclature

Latin symbols

c_p	specific heat capacity, J/(kgK)
C	Darcian source term constant, kg/(m^{3}s)
D	diffusivity, m^2/s
D_h	hydraulic diameter, m
h	enthalpy, J/kg
h_{sv}	latent heat of sublimation, J/kg
h_c	convective heat transfer coefficient, W/(m^{2}K)
h_m	mass transfer coefficient, m/s
$\vec{j}$	diffusion mass flux, kg/(m^{2}s)
$\dot{m}$	water vapour mass flux, kg/(m^{2}s)
$\dot{q}$	heat flux, W/m^2
$\mathbf{r}$	vector of residuals
S	Darcian source term coefficient, kg/(m^{3}s)
SSD	supersaturation degree
T	temperature, K (Celsius when specified)
p	pressure, Pa
u	averaged or seepage (Darcy) velocity $\varepsilon_v \cdot v$, m/s
v	velocity, m/s
V	volume, m^3
W	water vapour concentration, kg$_v$/kg$_{da}$
x	mole fraction
$\mathbf{x}$	vector of variables
y	coordinate, m
Y_v	water vapour concentration, kg$_v$/kg$_{ha}$

Greek symbols

α_r	relaxation factor
δ	relative error
δy	mesh displacement, m
Δy_{fs}	growth displacement, m

1

ε	porosity
λ	conductivity, W/mK
μ	diffusion resistance factor
ρ	density, kg/m^3
τ	tortuosity
$\dot{\omega}_i$	ice generation, kg/(m^{3}s)
$\dot{\omega}_v$	water vapour generation, kg/(m^{3}s)

Subscripts

av	averaged
da	dry air
dens	related to the densification of the frost layer
Δy	related to the increase of layer thickness
eff	effective
fl	frost layer (contains ice and humid air)
fs	frost surface
ha	humid air
i	ice
lat	latent
sat	saturated
t	total
v	water vapour
w	wall
x	related to the position in streamwise direction
0	initial value
∞	far field conditions

Superscripts

ℓ	current outer iteration
m	current inner iteration
n	current time step
q	iteration

$$1$$

Introduction

The main topic of this research is the development of new state-of-the-art numerical models to simulate the frost growth and densification. The conceived methods use finite volume approaches under either static or dynamic grids. In this introductory chapter, ice physics and, in particular frost formation, are presented. The different methods and approaches to model frosting are introduced. From these, the main objectives and outline of the thesis are derived.

1.1 Background of the research group

The Heat and Mass Transfer Technological Center (CTTC) was created in the 1990s, aiming to study the mathematical formulation, numerical resolution and experimental validation of fluid dynamics and heat and mass transfer phenomena, in order to develop and optimise thermal systems and equipment.

In the early 2000s, the existing group codes are generalized to create the CFD code called *TermoFluids* [1]. *TermoFluids* is the tool in which most of the group's research regarding numerical analysis is based upon.

The work developed in this thesis has been implemented into *TermoFluids*. The *TermoFluids* [1] code is a 3D unstructured parallel code that uses state-of-the-art numerical and physical models to perform accurate scientific analysis of engineering problems. Special care has been taken in its parallel performance, having a high efficiency in supercomputers. The development of the code has been a source of scientific publications in the most prominent scientific journals, which supports its reliability.

A finite volume collocated discretization of the Navier-Stokes equations is employed. This discretization is conservative because the implemented numerical schemes preserve the properties of the differential operators, i.e. discretization properties which ensure the kinetic-energy conservation and the stability of the numerical output.

(a) Third floor view at the CTTC.   (b) JFF cluster at the CTTC.

Figure 1.1: The CTTC facilities.

The CTTC works with the JFF HPC cluster (see Fig. 1.1), which has a total of 2304 cores (1024 processing cores 128 nodes of two Quad-core CPUs each and 1280 processing cores distributed in 40 nodes of 32 Cores each). It has an infiniband DDR 4X network interconnection between nodes with latencies of 2.25 microseconds with a 20Gbits/s bandwidth and and a high performance shared file system with storage of 240 Terabytes. The *TermoFluids* scalability in solving the Navier-Stokes equations has been recently tested up to 131072 CPU at the Argonne Leadership Computing Facility (ALCF) [2].

1.2 Ice

Ice is the solid state of water (H_2O). It is vastly found on oceans, rivers, streams and lakes, on land, and in the air. 12% of the globe is permanently covered in ice and snow, reaching 33% when taking into account seasonal snow. The enormous heat capacity associated with the phase change between water and ice (it takes 80 times as much heat to melt ice as to raise the temperature of the resulting water by one degree Celsius) keeps us from becoming too hot or too cold. In concert with other agents, ice also plays fascinating moderating roles. For example, snow covered surfaces reflect 80 to 90% of incoming solar radiation, whereas open sea water only 5%. The resulting ice-albedo feedback can lead to a fully frozen planet or to a hot, ice-free Earth if unchecked by other processes [3].

Ice is formed either by a process of solidification, when changing from a liquid to a solid state, or by desublimation, when changing directly from a gas to a solid state.
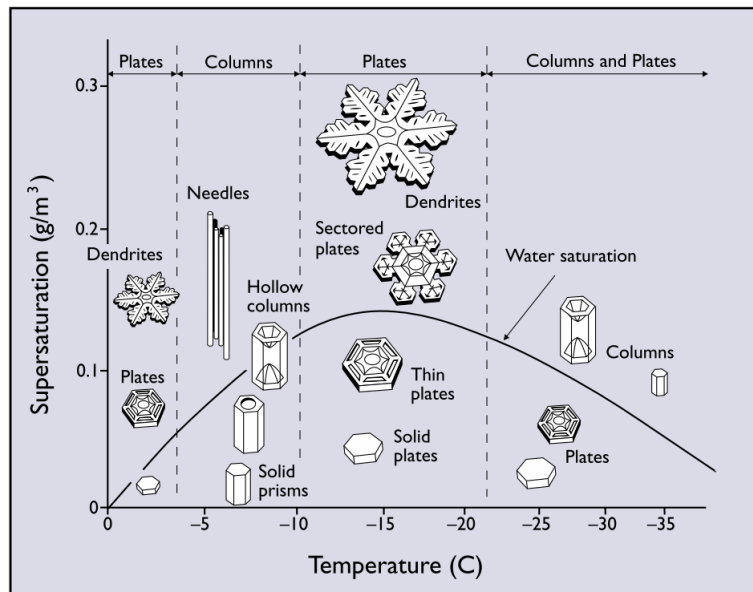
Figure 1.2: Snow crystal types adapted from Y. Furakawa (reprinted from Libbrecht [4]).

In the latter, a continuous desublimation of water vapour leads to the accumulation of ice by means of a process named frosting. The output macroscopical crystaline structure is called frost.

Depending on the enviromental conditions in which frost is being created, different crystal shapes are formed (see Fig. 1.2). The growth of these crystals on surfaces become large structures of frost. In particular, types of frost include hoar frost from deposition of water vapour from air of low humidity, white frost in humid conditions, window frost on glass surfaces, and advection frost from cold wind over cold surfaces (see Fig. 1.3), among others.

In order for such structures to grow, a thin layer of interconnected crystals must exist. This base is created by two possible incipient frosting modes: desublimation, which is a direct transformation of water vapour to ice, and condensation frosting, where the vapour first condenses into supercooled dew droplets which subsequently freeze.

(a) Hoar frost.

(b) White frost.

(c) Window frost.

(d) Advection frost.

Figure 1.3: Frost types: (a) hoar frost or radiation frost is typically formed in cold, clear nights, under low wind conditions, (b) white frost, made of needle-shaped crystals, forms under relative humidities above 90% and temperatures below -8°C, (c) window frost grows when a glass surface is exposed to a cold environment on one side, and moderately warm on the other, and (d) advection frost grows against the direction of the wind.

1.3 Frosting stages

Supersaturation of the vapour is required in order for a phase transition to happen. Such state is obtained by bringing humid air in contact with a surface whose temperature is below its corresponding dewpoint temperature. Depending on whether the aforementioned dewpoint temperature is below or above the freezing temperature (0°C at atmospheric pressure), the vapour will transition to the solid (ice) state or to liquid water, respectively. The formation of frost is governed by that very physical phenomenon. Nevertheless, depending on the arrangement of the ice structure on which such vapour is being deposited, the ice matrix will grow in a different manner.

Observations of the frost formation in the past 40 years have led to several interpretations of the physical stages undergone while the layer grows and densifies, each of them driven by a particular physical mechanism.

Hayashi *et al.* [5] divided the frosting process into three periods: the *crystal growth period*, the *frost layer growth period* and the *frost layer full growth period* (see Fig. 1.4). The first refers to an early growth period characterized by an initial heterogeneous nucleation and subsequent embryo growth, covering the cold surface as a thin layer of interconnected ice crystals. The second period consists in a uniform growth of the ice crystals, which interact with each other, resulting in a macroscopical porous layer. The third period is reached when the frost surface temperature reaches the melting point. From that point onwards, new deposition sites at the frost surface will form in liquid phase, which will soak into the frost layer, freezing in the inside. This cycle process continues periodically until the heat transfer condition reaches the equilibrium.

Later on, Tao *et al.* [6] suggested a slightly different division, separating Hayashi's *crystal growth period* into a first *dropwise condensation period*, with a later *solidified liquid tip growth period* (both periods shown in Fig. 1.5). The former two periods are followed by a *densification and bulk growth period*, which starts when the frost layer appears globally homogeneous and posseses the characteristics of a porous medium. Figure 1.5 shows the differences between Hayashi's and Tao's approaches.

Recent discoveries have led to a deeper understanding of the physical mechanisms of incipient frosting, in particular to condensation frosting. Nath *et al.* [7] summarized the stages of frost formation as follows:

1. Supercooled condensation. Consists in heterogeneous nucleation on a substrate, and subsequent growth.

2. Onset of freezing (see Fig. 1.6).

3. Frost halos. Due to the latent heat released when the droplet is freezing, water vapour can flow out from the ice interface. This creates an annular ring of
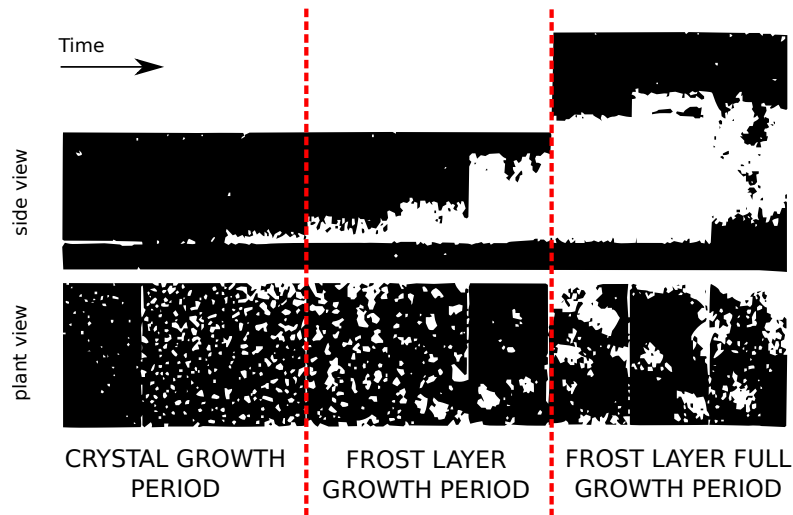
Figure 1.4: Hayashi's defined stages.

microdroplets around the frozen droplet which can quickly freeze over, calling them halos.

4. Interdroplet ice bridging and dry zones.

5. Percolation clusters and frost densification.

The first three stages are common with icing. It was long believed that each condensate droplet freezes in isolation due to heterogeneous or homogeneous nucleation without interacting with neighboring droplets. This is true for temperatures below $-40°C$ where the delay in nucleation time is negligible, and almost all the droplets freeze simultaneously [8]. However, for temperatures higher than $-40°C$, the vast majority of the droplets does not freeze in isolation, but rather are frozen by interdroplet interactions. The dominant mechanism of condensation frosting is that of interdroplet ice bridging (stage 4), where frozen droplets grow ice bridges towards their neighbouring liquid droplets to form an interconnected ice network. Because the liquid droplets sufficiently far from their neighbouring frozen droplet can completely evaporate, fueling the ice bridges, dry annular zones are created. Once the bridging among the ice crystals form a well-enough interconnected ice layer, the out-of-plane frost growth can happen (stage 5).

The present thesis is devoted to the numerical study of the frost densification stage, which corresponds to Hayashi's *frost layer growth period*, Tao's *densification and*
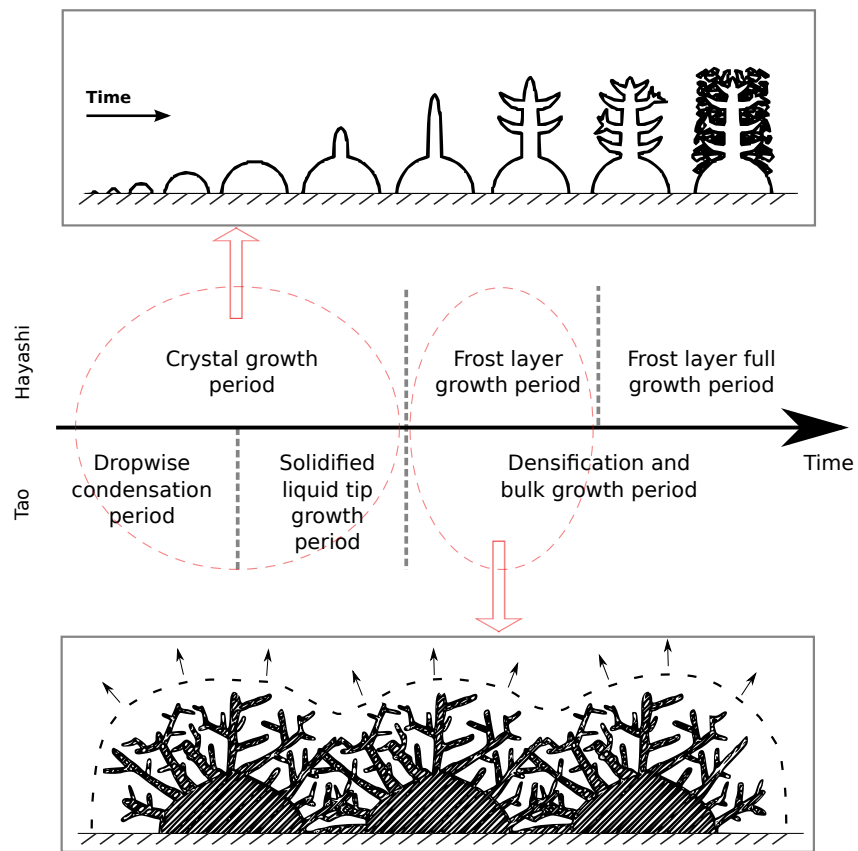
Figure 1.5: Stages Hayashi and Tao.
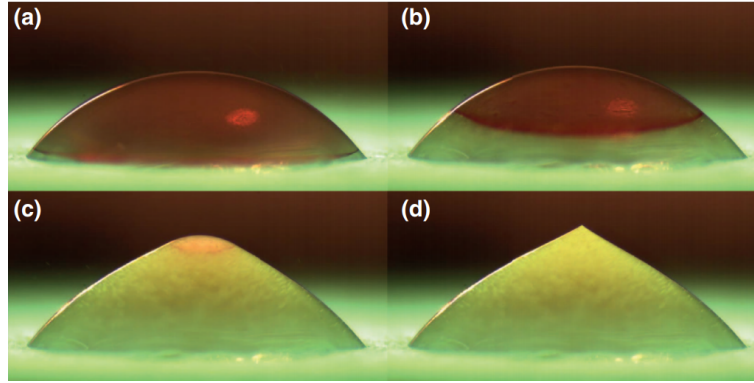
Figure 1.6: Condensated water droplet freezes from bottom (a) to top (d), ending with a tip singularity (reprinted from Enríquez *et al.* [9]).

bulk growth period or Nath's described stage 5. Despite nucleation and early stage models are not here studied, efforts have also been made in adding the capacity to the developed algorithms of accounting for the appearance of ice. Defrosting (melting of the frost surface when it reaches the melting point, and the subsequent liquid water penetration and final solidification) will not be treated in the present work, leaving it for future work (see Chapter 5).

1.4 Models of frost growth prediction

A comprehensive number of studies have modelled the frost densification stage from a macroscopical point of view. Based on how equations are set, frost growth models coupled with a free air flow region, using a finite volume approach, can be divided into two main blocks: the two-domain approach and the single-domain approach (see Fig. 1.7).

The two-domain approach consists in solving separately the frost and the free air regions. If the implemented frost growth model is 1D (see [10–15] among others), a mesh accounting for the frost domain is not specifically needed [16]. Moreover, it allows implementing a frost growth model with a zero frost thickness initial condition [15]. On the other hand, 2D and 3D frost growth models need a mesh to account for the frost domain, where distributions of the porosity, or the frost density, and the temperature are calculated. These models do need an initial frost thickness [17–19], as the mesh occupies a certain amount of volume. Despite the fact that the results for frost growth remain unaffected when using close to zero initial thicknesses [20], the region where frost will grow must be known in advance. Regardless of the im-

(a) Single domain approach. (b) Two domain approach.
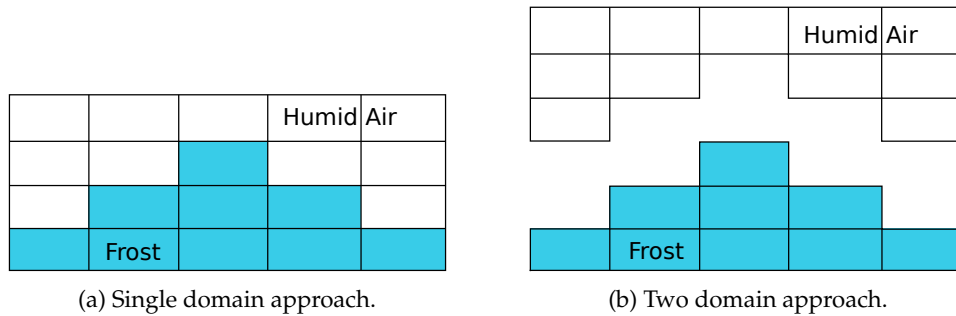
Figure 1.7: Approach types are dependent on grid set-up.

plemented frosting model, either static or dynamic meshes can be used. The first is more common in the literature, despite its inherent lack of accuracy when tracking the frost-air interface [16–18]. When dynamic meshes are used, an ALE formulation is set to correct the mass and energy fluxes due to the imposed grid deformations derived from the frost growth [6, 21–23]. The two domains are then coupled by means of a mass and energy balance at the frost-air interface along with a water vapour pressure condition.

There are just a few studies using single-domain approaches (see [24–26]). These do not need an initial frost thickness, fact that not only allows solving the appearance of frost, but also having several unconnected frost regions growing simultaneously. Similarly to the two-domain approach with a static mesh, the usage of fixed grids compared to deformable grids could dramatically reduce the simulation computational costs and resources, as the mesh does not need to readapt at each iteration. Furthermore, no extra communication between the two domains is required.

1.5   Objectives of the thesis

It is because the appearance of ice is so frequent on the Earth's surface , and thus coexists in our daily lives, it has always aroused an interest to humanity to understand its physics. More than 2000 years ago the Greeks had already an extraordinary understanding of the concept of phase transitions, and in particular, in regards to water. Indeed, in the fourth century BC, Aristotle correctly identified the two previously introduced modes of incipient frosting [27]. Nevertheless, it was not until 1657, soon after Galileo's death, that the experimentalists of the Florence Accademy of Cimento performed the first systematic experiments of water in an enclosed jar to validate Galileo's anti-Aristotelean claims: the most relevant, that ice is lighter than water [27].

We have come a long way since, and yet we have not. Despite the significant advances in the understanding of ice physics [4, 8, 28–31], we are far from solving the icing problem. From an economic standpoint, ice accretion is today a multibillion dollar problem. Indeed, icing and frosting cause malfunctioning in a wide variety of industrial applications (see Fig. 1.8), including aviation, aerospace, electrical transmission, hydropower, wind power, oil rigs and almost all modes of transportation [32].

For example, frost can form on aircraft wings either in-flight (when crossing supersaturated icing clouds [33]) and on-ground (tipically through nocturnal frost or cold soaked fuel frost). Weight is added and the aerodynamical performace reduced, causing severe damage and even plane crashes [34–37]. Icing and frosting have also been shown to cause mechanical damage to helicopter blades and fuselage [38], wind turbine failure [39], pose severe safety hazards to offshore oil exploration platforms [40], damage locks and dams [32, 41], and account for up to 40% of road accidents in winter [42, 43]. Accumulated frost on heat exchangers can reduce their heat transfer efficiency by as much as 50-75% [44, 45]. Furthermore, frosting can also cause mechanical damage to power transmission line systems, as well as induce electric faults, such as flashovers, due to insufficient clearances [46, 47]. Hence, providing robust numerical methods to predict the appearance and growth of frost is of key importance to counteract such undesired effects and, as a consequence, improving designs that enhance safety, increase the efficiency and avoid mechanical damage.

The available methods to solve the frost growth [10–15, 17, 19–21, 24, 48, 49] still lack a consensus on the empirical correlations used as input parameters of the models. Moreover, the fact of using fixed grids when solving the humid air - frost growth coupled problem lead to non-accurate trackings of the air-frost interface. Furthermore, despite a large portion of the frost sheet contains only about 10% of ice (the rest is humid air), no convective effects have yet been taken into account in single phase models. In this line, this thesis aims to:

- Develop a model that simulates the frost growth which tracks accurately the air-frost interface, by means of a dynamic mesh method.

- Develop a model capable to simulate the appearance and frost growth of complex geometries using a fixed grid.

The output of the present research not only contributes to a better understanding of the physics of frost growth phenomena, but also to the fact of providing new, robust and reliable models capable to simulate vast and complex geometries in 2D and 3D domains, which allow solving such physics on real industrial applications.
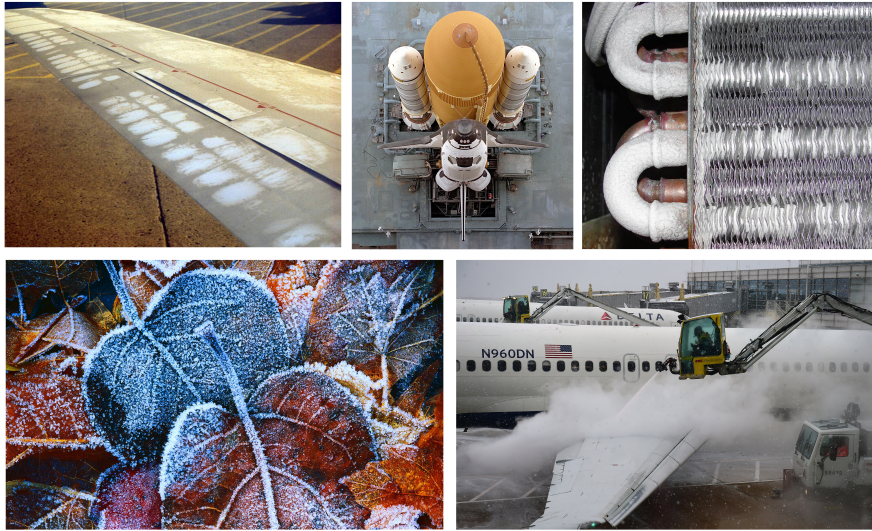
Figure 1.8: Industrial applications.

1.6 Outline of the thesis

The Heat and Mass Transfer Technological Center (CTTC) counts with an extensive experience in numerical and experimental fluid mechanics, and heat and mass transfer. Nevertheless, despite a first 0D model approach had been implemented by Oliet [50], frosting had not yet been studied in detail. Being this the first effort within the CTTC research group on this subject.

With the capabilities that the *TermoFluids* code offers, modelling the frost formation was not only a motivating challenge to adding such phenomenon into multiphysics problems, but also an incitement and ambition to deepen the understanding of both the physics involved in such a complex phenomenon (which include phase transitions and flow through porous media), as well as the applicability of formerly developed methods in regards of grid deformations.

The thesis consists of two main cores, contained in Chapters 2 and 3, which encompass from an accurate moving mesh method to solve the frost growth to a fixed grid method capable to easily adapt to complex geometries. In particular, the contents of these chapters have been submitted or published in international journals and conferences. Hence, they are written to be self-contained, and only minor changes have been introduced with respect to the original papers. Two appendices, which include material that may be useful in order to follow some parts of this work, have

been placed apart so that the normal reading of the thesis is not disturbed.

Chapter 2 is aimed, in detail, at developing a two-domain approach methodology, capable of simulating the frost growth (without solving the external flow in detail), in which the air-frost interface is tracked accurately by means of a dynamic mesh method. The developed methodology allows us to focus and obtain more insight into the physics of the frosting phenomenon, as well as the performance and suitability of various empirical inputs generally needed by frost growth models. Because of the large amount of empirical correlations available in the literature, 1D parametric tests are performed in order to extract relevant conclusions. Contrary to the already developed *TermoFluids* explicit solvers, a special effort is made on implementing implicit schemes which enable solutions to be computed in less computational time. The model is then validated by simulating a 2D case. The dynamic mesh method is thus proved to provide an excellent tracking of the air-frost interface.

After implementing and validating the methodology introduced in Chapter 2, a logical step was to add the external flow, computing it in a secondary mesh, that would also be deformed by the frost-air interface front. Nevertheless, the physical insights extracted from the performed numerical tests, i.e. that enhanced diffusion resistance factors must be used in order to capture the frost growth and densification, suggested that convective effects, despite the fact that they are usually neglected within the frost layer, might play an important role in the icing physics.

This is the main motivation of Chapter 3, where a model capable to solve the velocities within the frost layer is developed. The novel single-domain approach model hereby introduced accounts for the formation and sublimation of frost along with a momentum solver which takes into account the frost using a porous media treatment.

Finally, the concluding remarks (Chapter 4) are presented, and the future actions (Chapter 5) are discussed in detail.

References

[1] Termo fluids s.l., webpage: www.termofluids.com.

[2] R Borrell, J Chiva, O Lehmkuhl, G Oyarzun, I Rodríguez, and A Oliva. Optimising the termofluids cfd code for petascale simulations. *International Journal of Computational Fluid Dynamics*, 30(6):425–430, 2016.

[3] M Grae Worster. "Ice". *EUROMECH Fluid Mechanics Fellow 2006 Paper*.

[4] Kenneth G Libbrecht. The physics of snow crystals. *Reports on progress in physics*, 68(4):855, 2005.

[5] Y. Hayashi, A Aoki, S Adaohi, and K Hori. Study of frost properties correlating with frost formation types. *Journal of Heat Transfer*, 99(May 1977):239–45, 1977.

[6] Y.-X. Tao, R.W. Besant, and K.S. Rezkallah. A mathematical model for predicting the densification and growth of frost on a flat plate. *International Journal of Heat and Mass Transfer*, 36(2):353–63, 1993.

[7] Saurabh Nath, S Farzad Ahmadi, and Jonathan B Boreyko. A review of condensation frosting. *Nanoscale and Microscale Thermophysical Engineering*, 21(2):81–101, 2017.

[8] Thomas Koop. Homogeneous ice nucleation in water and aqueous solutions. *Zeitschrift für physikalische Chemie*, 218(11):1231–1258, 2004.

[9] Oscar R Enríquez, Álvaro G Marín, Koen G Winkels, and Jacco H Snoeijer. Freezing singularities in water drops. *Physics of fluids*, 24(9):091102, 2012.

[10] Kwan-Soo Lee, Sung Jhee, and Dong-Keun Yang. Prediction of the frost formation on a cold flat surface. *International Journal of Heat and Mass Transfer*, 46(20):3789–96, September 2003.

[11] Y.B. Lee and S.T. Ro. Analysis of the frost growth on a flat plate by simple models of saturation and supersaturation. *Experimental Thermal and Fluid Science*, 29(6):685–96, July 2005.

[12] Byeongchul Na and Ralph L. Webb. New model for frost growth rate. *International Journal of Heat and Mass Transfer*, 47:925–36, 2004.

[13] Christian JL Hermes, Robson O Piucco, Jader R Barbosa, and Cláudio Melo. A study of frost growth and densification on flat surfaces. *Experimental Thermal and Fluid Science*, 33(2):371–379, 2009.

[14] Amne El Cheikh and Anthony Jacobi. A mathematical model for frost growth and densification on flat surfaces. *International Journal of Heat and Mass Transfer*, 77:604–11, 2014.

[15] Max Kandula. Frost growth and densification in laminar flow over flat surfaces. *International Journal of Heat and Mass Transfer*, 54:3719–31, 2011.

[16] Donghee Kim, Chiwon Kim, and Kwan-Soo Lee. Frosting model for predicting macroscopic and local frost behaviors on a cold plate. *International Journal of Heat and Mass Transfer*, 82:135–142, 2015.

[17] Bernard Frankovic Kristian Lenic, Anica Trp. Transient two-dimensional model of frost formation on a fin-and-tube heat exchanger. *International Journal of Heat and Mass Transfer*, 52:22–32, 2009.

[18] JM Armengol, CT Salinas, J Xaman, and KAR Ismail. Modeling of frost formation over parallel cold plates considering a two-dimensional growth rate. *International Journal of Thermal Sciences*, 104:245–256, 2016.

[19] Chiwon Kim, Jaehwan Lee, and Kwan-Soo Lee. Numerical modeling of frost growth and densification on a cold plate using frost formation resistance. *International Journal of Heat and Mass Transfer*, 115:1055–1063, 2017.

[20] B.W. Jones and J.D. Parker. Frost formation with varying environmental parameters. *Journal of Heat Transfer*, 97(2):255–259, 1975.

[21] R. Le Gall, J.M. Grillot, and C. Jallut. Modelling of frost growth and densification. *International Journal of Heat and Mass Transfer*, 40(13):3177–87, 1997.

[22] Simon Ellgas and Michael Pfitzner. Modeling frost formation within a commercial 3-d cfd code. *Numerical Heat Transfer, Part A: Applications*, 53(5):485–506, 2007.

[23] Eduard Bartrons, Carles Oliet, Enrique GutiÃ©rrez, Alireza Naseri, and Carlos David PÃ©rez-Segarra. A finite volume method to solve the frost growth using dynamic meshes. *International Journal of Heat and Mass Transfer*, 124:615–628, 2018.

[24] J Cui, WZ Li, Y Liu, and ZY Jiang. A new time- and space-dependent model for predicting frost formation. *Applied Thermal Engineering*, 31:447–457, 2011.

[25] Xiaomin Wu, Qiang Ma, Fuqiang Chu, and Shan Hu. Phase change mass transfer model for frost growth and densification. *International Journal of Heat and Mass Transfer*, 96:11–19, 2016.

[26] Xiaomin Wu, Fuqiang Chu, and Qiang Ma. Frosting model based on phase change driving force. *International Journal of Heat and Mass Transfer*, 110:760–767, 2017.

[27] Jonathan Barnes et al. *Complete works of Aristotle, volume 1: The revised Oxford translation*, volume 1. Princeton University Press, 2014.

[28] Neville Horner Fletcher. *The chemical physics of ice*. Cambridge University Press, 1970.

[29] WF Budd and TH Jacka. A review of ice rheology for ice sheet modelling. *Cold Regions Science and Technology*, 16(2):107–144, 1989.

[30] Hans R Pruppacher, James D Klett, and Pao K Wang. *Microphysics of clouds and precipitation*. Taylor & Francis, 1998.

[31] G John Morris and Elizabeth Acton. Controlled ice nucleation in cryopreservation–a review. *Cryobiology*, 66(2):85–92, 2013.

[32] Susan Frankenstein and Andrew M Tuthill. Ice adhesion to locks and dams: past work; future directions? *Journal of Cold Regions Engineering*, 16(2):83–96, 2002.

[33] Kripa K Varanasi, Tao Deng, J David Smith, Ming Hsu, and Nitin Bhate. Frost formation and ice adhesion on superhydrophobic surfaces. *Applied Physics Letters*, 97(23):234102, 2010.

[34] RW Gent, NP Dart, and JT Cansdale. Aircraft icing. *Philosophical Transactions of the Royal Society of London A: Mathematical, Physical and Engineering Sciences*, 358(1776):2873–2911, 2000.

[35] Yihua Cao, Zhenlong Wu, Yuan Su, and Zhongda Xu. Aircraft flight characteristics in icing conditions. *Progress in Aerospace Sciences*, 74:62–80, 2015.

[36] WS Pike. Extreme warm frontal icing on 25 February 1994 causes an aircraft accident near Uttoxeter. *Meteorological Applications*, 2(3):273–279, 1995.

[37] J Marwitz, M Politovich, B Bernstein, F Ralph, P Neiman, R Ashenden, and J Bresch. Meteorological conditions associated with the ATR72 aircraft accident near Roselawn, Indiana, on 31 October 1994. *Bulletin of the American Meteorological Society*, 78(1):41–52, 1997.

[38] Charles Ryerson, Thomas Gilligan, and George Koenig. Evaluation of three helicopter preflight deicing techniques. In *37th Aerospace Sciences Meeting and Exhibit*, page 499, 1999.

[39] Olivier Parent and Adrian Ilinca. Anti-icing and de-icing techniques for wind turbines: Critical review. *Cold regions science and technology*, 65(1):88–96, 2011.

[40] Charles C Ryerson. Ice protection of offshore platforms. *Cold Regions Science and Technology*, 65(1):97–110, 2011.

[41] Srinivas Bengaluru Subramanyam, Konrad Rykaczewski, and Kripa K Varanasi. Ice adhesion on lubricant-impregnated textured surfaces. *Langmuir*, 29(44):13414–13418, 2013.

[42] J Andrey and Richard Olley. The relationship between weather and road safety: past and future research directions. *Climatological Bulletin*, 24(3):123–127, 1990.

[43] Anna K Andersson and Lee Chapman. The impact of climate change on winter road maintenance and traffic accidents in West Midlands, UK. *Accident Analysis & Prevention*, 43(1):284–289, 2011.

[44] AF Emery and BL Siegel. Experimental measurements of the effects of frost formation on heat exchanger performance. In *Numerical Heat Transfer-Presented at AIAA/ASME Thermophysics and Heat Transfer Conference*. Publ by ASME, 1990.

[45] Lingyan Huang, Zhongliang Liu, Yaomin Liu, Yujun Gou, and Jieteng Wang. Experimental study on frost release on fin-and-tube heat exchangers by use of a novel anti-frosting paint. *Experimental Thermal and Fluid Science*, 33(7):1049–1054, 2009.

[46] Masoud Farzaneh. *Atmospheric icing of power networks*. Springer Science & Business Media, 2008.

[47] Kunpeng Ji, Xiaoming Rui, Lin Li, André Leblond, and Ghyslaine McClure. A novel ice-shedding model for overhead power line conductors with the consideration of adhesive/cohesive forces. *Computers & Structures*, 157:153–164, 2015.

[48] P. L. T. Brian, R. C. Reid, and Y. T. Shah. Frost deposition on cold surfaces. *Industrial & Engineering Chemistry Fundamentals*, 9(3):375–80, 1970.

[49] Kwan-Soo Lee, Woo-Seung Kim, and Tae-Hee Lee. A one-dimensional model for frost formation on a cold flat surface. *International Journal of Heat and Mass Transfer*, 40(18):4359–4365, November 1997.

[50] C. Oliet. *Numerical simulation and experimental validation of fin-and-tube heat exchangers*. PhD thesis, Universitat Politècnica de Catalunya, 2006.

2

A finite volume method to solve the frost growth using dynamic meshes

Abstract. The physical mechanisms of frost formation have been widely studied, yet much empirism is still needed in numerical approaches. Indeed, accurate simulations of frost growth can be reached by setting up a specific combination of the model empirical inputs while using a method to accurately track the frost-air interface.

This chapter presents a finite volume ALE method which captures the air-frost interface using dynamic meshes. It is divided into two main sections. First, the search of a valid set of empirical correlations to correctly emulate frost growth under certain experimental conditions. An assessment of seven reference cases is carried out by comparing solutions using different empirical correlations against experimental data. As a result, a discussion on the performance of such parameters is made, emphasizing the fact of using diffusion resistance factors above 1.0 in order to capture the frost growth. Second, a 2D numerical test consisting of a duct flow with a non-homogeneously cooled lower boundary is performed. Aspects related to the frost thickness and growth rate are analysed, proving the method to be a valid candidate to simulate frost growth.

2.1 Introduction

Whenever a surface is in contact with humid air below the dew and freezing points, water vapour will desublimate, transitioning to a solid state that will form a crystaline structure called frost. Frost formation is a common and usually undesired phenomenon that affects the aerospace, cryogenics and refrigeration industry, among others. Frost can form on aircraft wings either on-ground (typically through nocturnal frost), and in-flight (when crossing supersaturated icing clouds [1]), adding weight and reducing the aerodynamical performance. It also causes a great impact on wind turbines, heat exchangers, engine turbine blades, electrical lines, etc. These issues highlight the need of understanding and accurately predicting frost formation.

Hayashi *et al.* [2] divided the frost formation mechanism into three periods: the *crystal growth period*, the *frost layer growth period* and the *frost layer full growth period*. The first refers to an early growth period characterized by crystal growth. First, heterogeneous nucleation and further embryo growth covers the cold wall as a thin frost layer. In the second period, the frost layer behaves as a porous medium, where crystals continue growing while interacting with each other. In this period, the initial rough frost becomes a uniform layer. It is considered to end when the thickness of the frost stops growing. The third period continues with a densification and growth of the frost layer, bringing with it an increase of the thermal resistance [2]. During that stage, the thickness growth is minimal, and the frost surface temperature rises until the melting point. From that point onwards, new deposition sites at the frost surface will form in liquid phase, which will soak into the frost layer, freezing in the inside. This cycle process continues periodically until the heat transfer condition reaches the equilibrium.

The frost layer growth period is the most studied among the three. Brian *et al.* [3] proposed first analytical approximations to model frost growth. Later on, Tao *et al.* [4] and Le Gall *et al.* [5] used averaged finite volume approaches, which were also used by Na and Webb [6] with some simplifications. Na and Webb's formulation was subsequently used by Lenic *et al.* [7], and recently by Armengol *et al.* [8] to address the air-frost coupled problem. Other significant approaches involving the computation of the fluid and frost domains are the coupling of a one dimensional frost model with a comercial CFD code by Ellgas and Pfitzner [9], the one-domain approach by Kim *et al.* [10], in which the one dimensional frosting model [11] is implemented, and the recent frost formation resistance model put forward by Kim *et al.* [12].

Despite the efforts to simulate the frost-free air coupled problem, there is still a lack of consensus in which empirical correlations capture better the frost formation. Furthermore, solutions with CFD approaches use static grids [7, 8, 13–16], which lead to a non-accurate tracking of the interface.

In view of the reported results, a finite volume approach based on Tao's mathematical formulation, which models the frost layer growth period (until the melting point
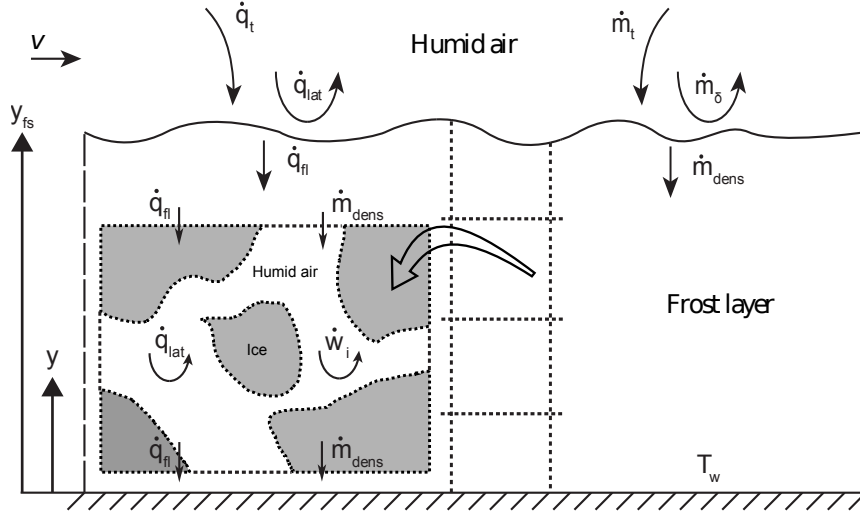
Figure 2.1: Sketch of the frost growth in a discretized domain. The detail of the elementary control volume shows the implemented averaged volume technique.

is reached) using a deformable mesh is here presented. This study aims to discuss the performance of the tested empirical correlations, and provide new insights throughout a critical analysis of seven reference cases, covering a wide range of experimental conditions. Finally, the stated methodology is used to numerically solve the frosting on a wind tunnel with a non-homogeneously cooled lower boundary, experimentally set up by Kwon *et al.* [17], in order to test the model capabilities.

2.2 Physical model and mathematical formulation

The mechanism of frost growth is shown in Fig. 2.1, in which a local averaged control volume analysis is depicted. The set out approach considers that a volume V is composed by the volumes occupied by the ice V_i, and the humid air V_{ha}. The ice volume fraction or ice porosity is then defined as $\varepsilon_i = V_i/V$. Similarly, the air porosity is expressed as $\varepsilon_{ha} = V_{ha}/V$. Moreover, the equalty $\varepsilon_{ha} + \varepsilon_i = 1$ must be preserved. In addition, note that the humid air porosity, the dry air porosity and the water vapour porosity stand for the same volume fraction, i.e., $\varepsilon_{ha} = \varepsilon_{da} = \varepsilon_v$. Such porosities will also be represented as ε_v for the sake of clarity.

The assumptions made in the present analysis are: (a) the total gas phase pressure p_{ha} is constant throughout the porous frost layer, and equal to the external atmospheric pressure p_∞; (b) water vapour, dry air and ice are in local thermal equilibrium,

i.e. $T_{ha} = T_v = T_{da} = T_i$; (c) water vapour inside the frost layer is saturated; (d) the heat and mass transfer analogy is applicable, with a constant Lewis number; (e) convection effects are negligible such that $\vec{v}_{ha} = 0$ within the frost layer [18], and (f) no movement of the ice crystals is allowed ($\vec{v}_i = 0$).

2.2.1 The transport diffusion equations

The vapour mass conservation equation reads as:

$$\frac{d}{dt} \int_{V_v} \rho_v dV_v + \int_{S_v} \rho_v (\vec{v}_v - \vec{v}_b) \cdot \vec{n} dS_v = \int_V \dot{\omega}_v dV \tag{2.1}$$

where the substantial derivative of the Eulerian density field including the volume swept by the mesh equals the generation or destruction of water vapour $\dot{\omega}_v$. Integrating over the volume V and rewriting the equation in terms of the water vapour diffusion mass flux $\vec{j}_v = \rho_v (\vec{v}_v - \vec{v}_{ha})$.

$$\frac{d}{dt} \int_V \rho_v \varepsilon_v dV + \int_S \rho_v \varepsilon_v (\vec{v}_{ha} - \vec{v}_b) \cdot \vec{n} dS + \int_S \varepsilon_v \vec{j}_v \vec{n} dS = \int_V \dot{\omega}_v dV \tag{2.2}$$

Applying that $\vec{v}_{ha} = 0$ and introducing Fick's law, i.e. $\vec{j}_v = -\rho_{ha} \tau D_v \nabla Y_v$:

$$\frac{d}{dt} \int_V \rho_v \varepsilon_v dV - \int_S \rho_v \varepsilon_v \vec{v}_b \cdot \vec{n} dS = \int_S \rho_{ha} \varepsilon_v \tau D_v \nabla Y_v \cdot \vec{n} dS + \int_V \dot{\omega}_v dV \tag{2.3}$$

where Y_v is the concentration of water vapour, and τ is the tortuosity. The effective diffusivity is defined as $D_{eff} \equiv \varepsilon_v \tau D_v$ or $D_{eff} \equiv \mu D_v$, where μ is called the diffusion resistance factor ($\mu \equiv \varepsilon_v \tau$). On the other hand, setting up the transport equation of the ice phase:

$$\frac{d}{dt} \int_V \rho_i \varepsilon_i dV + \int_S \rho_i \varepsilon_i (\vec{v}_i - \vec{v}_b) \cdot \vec{n} dS = \int_V \dot{\omega}_i dV \tag{2.4}$$

where ice generation equals water vapour destruction ($\dot{\omega}_i = -\dot{\omega}_v$). Applying the equality into Eq.2.4 and substituting into Eq. 2.3, while considering $\vec{v}_i = 0$, and rearranging the terms:

$$\begin{aligned} \frac{d}{dt} \int_V \varepsilon_v (\rho_v - \rho_i) \, dV - \int_S \varepsilon_v (\rho_v - \rho_i) \, \vec{v}_b \cdot \vec{n} dS = \int_S \rho_i \vec{v}_b \vec{n} dS \\ - \frac{d}{dt} \int_V \rho_i dV + \int_S \rho_{ha} D_{eff} \nabla Y_v \cdot \vec{n} dS \end{aligned} \tag{2.5}$$

2.2.2 The energy equation

The energy conservation equation is given by the following equation:

$$\frac{\mathrm{d}}{\mathrm{d}t} \sum_k \int_{V_k} \left(\rho_k h_k - p_k \right) \mathrm{d}V_k + \sum_k \int_{S_k} \rho_k h_k \left(\vec{v}_k - \vec{v}_b \right) \cdot \vec{n} \mathrm{d}S_k = - \sum_k \int_{S_k} \vec{\dot{q}}_k \cdot \vec{n} \mathrm{d}S_k \qquad (2.6)$$

where $k = \{i, v, \mathrm{da}\}$. Rewriting the former in terms of the diffusion mass flux $\vec{j}_r = \rho_r \left(\vec{v}_r - \vec{v}_{\mathrm{ha}} \right)$, where $r = \{v, \mathrm{da}\}$, and applying the condition $p_{\mathrm{ha}} \approx p_i \approx p_\infty$ as well as the assumed zero velocities of the ice and humid air within the frost layer:

$$\frac{\mathrm{d}}{\mathrm{d}t} \int_V \left(\varepsilon_i \rho_i h_i + \varepsilon_v \rho_{\mathrm{ha}} h_{\mathrm{ha}} \right) \mathrm{d}V - \int_S \left(\varepsilon_i \rho_i h_i + \varepsilon_v \rho_{\mathrm{ha}} h_{\mathrm{ha}} \right) \vec{v}_b \cdot \vec{n} \mathrm{d}S$$
$$+ \int_S \varepsilon_v h_v \vec{j}_v \cdot \vec{n} \mathrm{d}S + \int_S \varepsilon_v h_{\mathrm{da}} \vec{j}_{\mathrm{da}} \cdot \vec{n} \mathrm{d}S = - \int_S \left(\varepsilon_i \vec{\dot{q}}_i + \varepsilon_{\mathrm{ha}} \vec{\dot{q}}_{\mathrm{ha}} \right) \cdot \vec{n} \mathrm{d}S \qquad (2.7)$$

Now, developing the enthalpy cross-diffusion terms:

$$\frac{\mathrm{d}}{\mathrm{d}t} \int_V \left(\varepsilon_i \rho_i h_i + \varepsilon_v \rho_{\mathrm{ha}} h_{\mathrm{ha}} \right) \mathrm{d}V - \int_S \left(\varepsilon_i \rho_i h_i + \varepsilon_v \rho_{\mathrm{ha}} h_{\mathrm{ha}} \right) \vec{v}_b \cdot \vec{n} \mathrm{d}S$$
$$+ \int_S \varepsilon_v \left(h_v - h_{\mathrm{da}} \right) \vec{j}_v \cdot \vec{n} \mathrm{d}S = - \int_S \left(\varepsilon_i \vec{\dot{q}}_i + \varepsilon_{\mathrm{ha}} \vec{\dot{q}}_{\mathrm{ha}} \right) \cdot \vec{n} \mathrm{d}S \qquad (2.8)$$

where $\vec{j}_v = -\vec{j}_{\mathrm{da}}$. Furthermore, defining the frost layer (fl) conduction heat flux as $\vec{\dot{q}}_{\mathrm{fl}} \equiv \varepsilon_i \vec{\dot{q}}_i + \varepsilon_{\mathrm{ha}} \vec{\dot{q}}_{\mathrm{ha}}$ and applying Fick's law:

$$\frac{\mathrm{d}}{\mathrm{d}t} \int_V \left(\varepsilon_i \rho_i h_i + \varepsilon_v \rho_{\mathrm{ha}} h_{\mathrm{ha}} \right) \mathrm{d}V - \int_S \left(\varepsilon_i \rho_i h_i + \varepsilon_v \rho_{\mathrm{ha}} h_{\mathrm{ha}} \right) \vec{v}_b \cdot \vec{n} \mathrm{d}S =$$
$$\int_S \left(h_v - h_{\mathrm{da}} \right) \rho_{\mathrm{ha}} D_{eff} \nabla Y_v \cdot \vec{n} \mathrm{d}S - \int_S \vec{\dot{q}}_{\mathrm{fl}} \cdot \vec{n} \mathrm{d}S \qquad (2.9)$$

The enthalpy cross-diffusion term on the right-hand side of the equation is neglected as it is about five orders of magnitude smaller than the heat flux term (see Table 2.1). Note that this term is not usually mentioned in the literature.

Recalling that enthalpies are defined as:

$(h_v - h_{\mathrm{da}})\,\rho_{ha}D_{\mathrm{eff}}\nabla Y_v$				$\vec{q}_{\mathrm{fl}} = -\lambda_{\mathrm{fl}}\nabla T$
$(h_v - h_{\mathrm{da}})$	$\rho_{\mathrm{ha}}D_{\mathrm{eff}}$	∇Y_v	λ_{fl}	∇T
10^7	10^{-7}	10^{-1}	10^{-1}	10^3
10^{-1}			10^2	

Table 2.1: Orders of magnitude of the right-hand side of Eq. 2.9.

$$h_n = h_{f_n} + \int_{T_{\mathrm{ref}}}^{T} c_{p_n}\mathrm{d}T \approx h_{f_n} + \bar{c}_{p_n}\left(T - T_{\mathrm{ref}}\right) \tag{2.10}$$

$$\bar{c}_{p_n} = \frac{1}{T - T_{\mathrm{ref}}}\int_{T_{\mathrm{ref}}}^{T} c_{p_n}\mathrm{d}T \tag{2.11}$$

where $n = \{i, v, \mathrm{da}\}$ and h_f is the formation enthalpy. Rearranging the terms of Eq. 2.9 in terms of the temperature, the following expression is reached:

$$\frac{\mathrm{d}}{\mathrm{d}t}\int_V \left(\mathcal{C}_1 T + \mathcal{C}_2\varepsilon_v + \mathcal{C}_3\varepsilon_v T\right)\mathrm{d}V - \int_S \left(\mathcal{C}_1 T + \mathcal{C}_2\varepsilon_v + \mathcal{C}_3\varepsilon_v T\right)\vec{v}_b\cdot\vec{n}\mathrm{d}S =$$
$$\int_S \left(\mathcal{C}_4 + p_\infty\right)\vec{v}_b\cdot\vec{n}\mathrm{d}S + \int_S \lambda_{\mathrm{fl}}\nabla T\vec{n}\mathrm{d}S - \frac{\mathrm{d}}{\mathrm{d}t}\int_V \mathcal{C}_4\mathrm{d}V \tag{2.12}$$

where λ_{fl} is the frost layer conductivity, and the coefficients $\mathcal{C}_1, \mathcal{C}_2, \mathcal{C}_3, \mathcal{C}_4$ are given by:

$$\mathcal{C}_1 = \rho_i\bar{c}_{p_i}$$
$$\mathcal{C}_2 = \rho_i\left(\bar{c}_{p_i}T_{\mathrm{ref}_i} - h_{f_i}\right) + \rho_{\mathrm{ha}}\bar{c}_{p_{\mathrm{da}}}T_{\mathrm{ref}_{\mathrm{da}}}\left(Y_v - 1\right) + \rho_{\mathrm{ha}}Y_v\left(h_{f_v} - \bar{c}_{p_v}T_{\mathrm{ref}_v}\right)$$
$$\mathcal{C}_3 = \rho_{\mathrm{ha}}\bar{c}_{p_{\mathrm{da}}}\left(1 - Y_v\right) - \rho_i\bar{c}_{p_i} + \rho_{\mathrm{ha}}Y_v\bar{c}_{p_v}$$
$$\mathcal{C}_4 = \rho_i\left(h_{f_i} - \bar{c}_{p_i}T_{\mathrm{ref}_i}\right) - p_\infty$$

2.2.3 Boundary conditions

Air-frost interface:

An energy balance at the interface gives the temperature at the frost surface (fs):

$$\underbrace{\lambda_{\text{fl}} \frac{\partial T_{\text{fl}}}{\partial n}}_{\dot{q}_{\text{fl}}} = \underbrace{h_c \left(T_\infty - T_{\text{fs}}\right)}_{\dot{q}_t} + \underbrace{\rho_{\text{fl}} \Delta h_{\text{sv}} \frac{\mathrm{d}y_{\text{fs}}}{\mathrm{d}t}}_{\dot{q}_{\text{lat}}} \tag{2.13}$$

where the sensible heat flux $\dot{q}_{\text{fl}}$, which penetrates into the frost layer, is generated by the heat convection from the surrounding air $\dot{q}_t$ caused by the temperature gradient between the air bulk and the frost surface, and by the latent heat of sublimation $\dot{q}_{\text{lat}}$ given by the desublimation of water vapour at the frost surface.

The Nusselt number correlations used in the present study vary depending on the tested experiment. Further detail on such taken values will be adressed in Section 2.5.1 and Section 2.6.

On the other hand, a mass balance at the frost interface allows the evaluation of the frost surface displacement:

$$\underbrace{\rho_{\text{fl}} \frac{\mathrm{d}y_{\text{fs}}}{\mathrm{d}t}}_{\dot{m}_{\Delta y}} = \underbrace{h_m \left(\rho_{v_\infty} - \rho_{v_{\text{fs}}}\right)}_{\dot{m}_t} - \underbrace{\rho_{\text{ha}} D_{\text{eff}} \frac{\partial Y_{v,\text{fl}}}{\partial n}}_{\dot{m}_{\text{dens}}} \tag{2.14}$$

Notice that the total deposited mass $\dot{m}_t$ breaks into the part that contributes to the growth of the frost thickness $\dot{m}_{\Delta y}$, and the one that densifies the frost layer $\dot{m}_{\text{dens}}$. The mass transfer coefficient h_m is calculated by means of the heat and mass transfer analogy that assumes a Lewis number of 1.

$$h_m = h_c / \left(\rho_{\text{ha},\infty} c_{p,\text{ha},\infty} Le^{2/3}\right) \tag{2.15}$$

The terms of Eqs. 2.13 and 2.14 are graphically shown in Fig. 2.1.

A major concern is the calculation of the water vapour pressure at the frost surface. Although theoretical analyses state the water vapour must be supersaturated for the phase change to occur, no general method for the calculation of such pressure values has yet been reported. Authors prior to Na and Webb [19], such as [5, 11], used a saturation condition. Na and Web suggested an empirical expression to model the supersaturation degree (see Eq. 2.16) extracted from linearizing the laminar boundary layer equations.

$$SSD_{\text{fs}} = 0.808 \left(\frac{p_{v,\infty}}{p_{v,\text{sat},\infty}}\right) \left(\frac{p_{v,\text{sat},\text{fs}}}{p_{v,\text{sat},\infty}}\right)^{-0.657} - 1 \tag{2.16}$$

for $\quad T_{\text{fs}} + 14 < T_\infty < T_{\text{fs}} + 20 \quad$ and $\quad 243.15K < T_{\text{fs}} < 273.15K$

where SSD_{fs} is defined as follows:

$$SSD_{\text{fs}} = \frac{p_{v,\text{fs}} - p_{v,\text{sat},\text{fs}}}{p_{v,\text{sat},\text{fs}}} \tag{2.17}$$

Kandula [20] again used a saturation condition claiming that the supersaturation degree is strongly dependent on the surface coating governing the contact angle, and that there is no such information in the reported experimental data.

Another condition was recently used by El Cheikh and Jacobi [21], which uses the total air heat flux acquired at the frost surface. Unfortunately, this condition needs such value from the experiment. Hence, it was not considered, and saturated and supersaturated conditions were tested. Whenever using the supersaturated condition given in Eq.2.16 and out of range, the saturated condition is applied.

In regards to the frost density, the Neumann type condition used by Na and Webb [6] is applied. Such condition assumes that the gradient of the frost density at the frost surface is zero, i.e. $\partial \rho_{\mathrm{fl}} / \partial n|_{\mathrm{fs}} = 0$.

The cold wall:

The cases tested in this study consider a Dirichlet type boundary condition, either through an isothermal wall $T = T_w$ in the 1D tests shown in Section 2.5, or a varying temperature over the wall in the 2D case presented in Section 2.6. The wall is assumed totally impermeable, such that the water vapour concentration gradient is zero, hence, $\partial Y_v / \partial n|_{\mathrm{w}} = 0$. Moreover, there is no change in porosity, which leads to $\partial \varepsilon_v / \partial n|_{\mathrm{w}} = 0$.

Other boundaries:

Neumann type boundary conditions are chosen for the temperature, water vapour concentration and porosity.

2.3 Thermo-physical properties

This section is dedicated to the definition of the implemented thermo-physical properties of ice and the humid air mixture, as well as the averaged frost properties used within the porous medium.

2.3.1 Ice properties

According to Fukusako's thermophysical correlations of ice [22], in the range of -25°C to 0°C, density changes are about 0.3%, while variations in that range for the conductivity and the specific heat are about 12% and 8%, respectively. The correlations of ice thermal conductivity and heat capacity proposed in the aforementioned paper are:

$$\lambda_i = 1.16 \left(1.91 - 8.66 \cdot 10^{-3}\theta + 2.97 \cdot 10^{-5}\theta^2 \right) \qquad \text{for} \quad 100K \leq T \leq 273K \qquad (2.18)$$

$$c_{p,i} = 1000 \cdot \left(0.185 + 0.689 \cdot 10^{-2}T \right) \qquad\qquad \text{for} \quad 90K \leq T \leq 273K \qquad (2.19)$$

where θ is in $[°C]$, and T is in $[K]$.

Several tests were carried out by changing the density, conductivity and specific heat capacity from variable to fixed values. Results show negligible variations under density and heat capacity changes. Hence, mean ice density is considered to be $\bar{\rho}_i = 918.9 kg/m^3$. Nevertheless, changes of approximately 2% on the thermal conductivity lead to accumulated mean density errors of approximately 2-3% after 3 hours of simulation time, stressing out the importance of using a variable ice conductivity.

2.3.2 Humid air properties

Pressure and density:

Due to the lack of information of the water vapour pressure in the inside of the frost layer, many authors assume the saturation condition. El Cheikh and Jacobi [21] used another formulation in which a mass transfer conductance is considered, avoiding the use of the aforementioned condition. Saturated water vapour below the freezing point can be approximated by the correlation given in [23]. Thus, the dry air pressure can be obtained from $P_{da} = P_\infty - P_{v,\text{sat}}$.

The humid air density, which is the sum of water vapour and dry air densities, is then easily calculated by means of the perfect gas law applied to both substances.

Thermal conductivity:

The thermal conductivity of humid air is a mixture of the dry air and water vapour conductivities. It can be calculated by means of the Studnikov expression found in [24].

$$\lambda_{\text{ha}} = \left(x_{\text{da}}\lambda_{\text{da}} + x_v\lambda_v \right) \frac{1 + \left(x_v - x_v^2 \right)}{2.75} \qquad (2.20)$$

where x_{da} and x_v are the dry air and water vapour mole fractions.

Dry air and water vapour conductivites are calculated by means of the suggested correlations by [25].

Diffusivity:

The water vapour diffusivity is determined from [26].

$$D_v = 2.11 \cdot 10^{-5} \left(\frac{T}{T_0}\right)^{1.94} \left(\frac{p_0}{p}\right) \quad \text{for} \quad 233.15K \leq T \leq 313.15K \qquad (2.21)$$

where T_0 and p_0 are the reference temperature ($273.15K$) and the reference pressure ($101325Pa$), respectively.

Specific heat capacity:

The specific heat capacity of humid air can be approximated as the sum of the heat capacities of its elements alone:

$$c_{p,\text{ha}} = Y_{\text{da}}c_{p,\text{da}} + Y_v c_{p,v} \qquad (2.22)$$

The dry air and water vapour heat capacities are given by polinomial fits extracted from the experimental data supplied in [27, 28]:

$$c_{p,\text{da}} = a_0 + a_1 T + a_2 T^2 + a_3 T^3 + a_4 T^4 \qquad \text{for} \quad 200K \leq T \leq 400K$$

$$c_{p,v} = \frac{1000}{18.01528}\left(b_1 + b_2 T + b_3 T^2 + b_4 T^3\right) \qquad \text{for} \quad 200K \leq T \leq 800K$$

where coefficients are:

$$a_0 = +8.858044433595\text{E} + 02 \qquad b_1 = +33.8\text{E} + 00$$
$$a_1 = +1.837101847329\text{E} + 00 \qquad b_2 = -0.00795\text{E} + 00$$
$$a_2 = -1.011132405598\text{E} - 02 \qquad b_3 = +2.8228\text{E} - 05$$
$$a_3 = +2.353255208331\text{E} - 05 \qquad b_4 = -1.3115\text{E} - 08$$
$$a_4 = -1.933268229165\text{E} - 08$$

2.3.3   Frost properties

The frost domain is comprised of a porous ice crystaline structure that contains humid air. Depending on the environmental conditions, a large diversity of crystals can be formed. Temperature mainly determines whether snow crystals will grow into plates or columns, while higher supersaturations produce more complex structures (an extensive study can be found in Libbrecht's work [29]). This will affect the thermal

conductivity of the frost as well as the mass diffusivity of the water vapour throughout the porous structure. In the present averaged volume approach, the former will be treated as an effective conductivity and diffusivity.

Frost density:

The frost density is directly calculated with the local porosity, humid air and ice densities.

$$\rho_{fl} = \varepsilon_{ha}\rho_{ha} + (1 - \varepsilon_v)\,\rho_i \tag{2.23}$$

Frost effective conductivity:

Among the large amount of correlations suggested in the literature (a detailed list can be found in [30,31]), the three thermal conductivity correlations proposed by Lee *et al.* [32], Na and Webb [6] and Negrelli *et al.* [30] are hereby tested. These are chosen due to being both some of the most widely (see [31]), and also most recently used.

Lee *et al.* [32] gave the following correlation:

$$\lambda_{fl} = 0.133 + 3.13e^{-4}\rho_{fl} + 1.6e^{-7}\rho_{fl}^2 \quad \text{for} \quad \bar{\rho}_{fl} \leq 500 kg/m^3 \tag{2.24}$$

Later studies by Na and Webb [6] in the line of the series-parallel model put forward by Sanders [33] suggest that:

$$\lambda_{fl} = \xi\lambda_{par} + (1 - \xi)\,\lambda_{ser} \tag{2.25}$$

where:

$$\lambda_{par} = \left(1 - \frac{\rho_{fl}}{\rho_i}\right)\lambda_{ha} + \frac{\rho_{fl}}{\rho_i}\lambda_i$$

$$\lambda_{ser} = \left[\frac{\rho_{fl}}{\rho_i}\frac{1}{\lambda_i} + \left(1 - \frac{\rho_{fl}}{\rho_i}\right)\frac{1}{\lambda_{ha}}\right]^{-1}$$

And the modeled ξ parameter is given in Table 3.2.

Negrelli *et al.* [30] have recently introduced a new correlation which takes into account the morphology of the crystals by means of the temperature and the porosity of the frost.

$$\frac{\lambda_{fl}}{\lambda_i} = a\left(\frac{\lambda_{ha}}{\lambda_i}\right)^{b\varepsilon_v} \quad \text{for} \quad 0.5 \leq \varepsilon_v \leq 0.95 \tag{2.26}$$

Coefficients a and b are listed in Table 2.3. For convenience, the three presented correlations will be referred in this chapter as Lee, Na and Webb and Negrelli.

	Range	ζ
(i)	$-10 < T_w < -4$ °C	$0.283 + e^{-0.020\rho_{fl}}$
(ii)	$-21 < T_w < -10$ °C	$0.140 + 0.919e^{-0.0142\rho_{fl}}$
(iii)	$T_w < -21$ °C and $\rho_{fl} < 200$kg/m^3	$0.0107 + 0.419e^{-0.00424\rho_{fl}}$
(iv)	$T_w < -21$ °C and $\rho_{fl} > 200$kg/m^3	$0.005\rho_{fl}\left(0.0107 + 0.419e^{-0.00424\rho_{fl}}\right)$

Table 2.2: ζ parameter of Na and Webb's effective thermal conductivity correlation.

	Temperature range	Morphology	a	b
(i)	$-10 < T_w < -4$ °C	Needles and sheaths	1.576	0.797
(ii)	$-19 < T_w < -10$ °C	Plates and dentrites	1.594	0.761
(iii)	$-30 < T_w < -19$ °C	Sheaths	1.035	0.797

Table 2.3: Coefficients of Eq. 2.26.

A comparison of the three correlations is depicted in Fig. 2.2. Whenever Negrelli's correlation is used, and due to the fact that this correlation does not cover the 0 to 1 porosity range, constant thermal conductivity values are set below 0.5 and above 0.95 porosity values, with the values obtained at these two porosities. This treatment is also applied to Lee's correlation when having averaged densities above $500kg/m^3$.

Frost effective diffusivity:

As deduced in Section 2.2.1, the effective diffusivity is a function of the local porosity, water vapour diffusivity and the tortuosity factor, or just a function of the diffusion resistance factor and the water vapour diffusivity. The tortuosity factor and the diffusion resistance factor are measures of the added difficulty to the water vapour following diffusion paths through the snow crystals. Values above unity contradict reality, as it seems that the water vapour would be able to follow a path shorter than a straight line. However, in the past Tao *et al.* [4] and Le Gall *et al.* [5] used correlations with values higher than 1. Yosida [34] also suggested a hand-to-hand delivery of water vapour as an explanation of such diffusion enhancements.

In this thesis, the most widely used correlations for the diffusion resistance factor have been tested. All of them are listed in Table 3.1. Moreover, Fig. 3.1 shows the calculated values which range from below 1 to 2.2.

Note that the correlations given by Bruggeman, Prager and Zehnder were obtained by means of experimental data of packed beds, not frost. Auracher was the only one
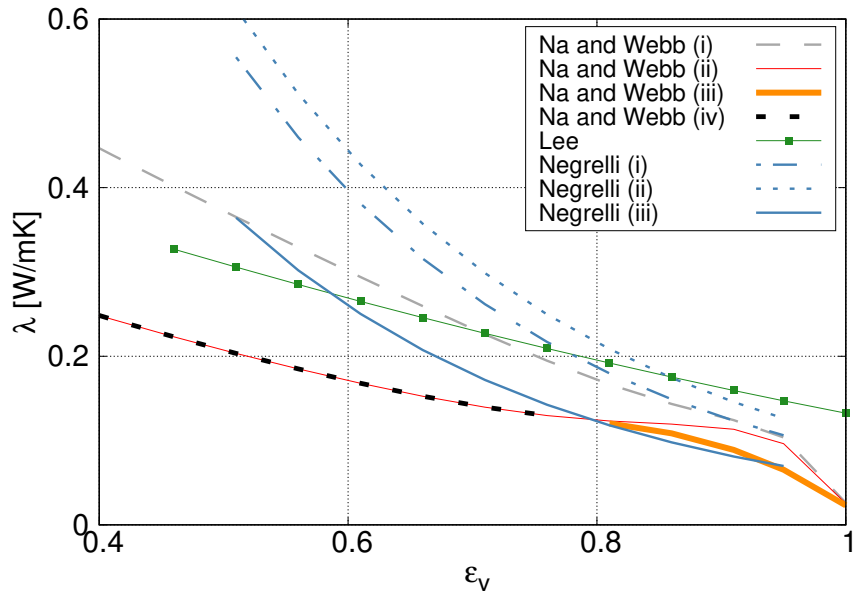
Figure 2.2: Comparison of frost conductivity correlations as a function of the porosity at $T = 240K$ (influence of temperature is minimal).

Author	Diffusion resistance factor
Bruggeman *et al.* [35]	$\mu = \varepsilon_v^{2/3}$
Prager *et al.* [35]	$\mu = 0.5\varepsilon_v\left(1+\varepsilon_v\right)$
Zehnder *et al.* [33]	$\mu = \left(1-\sqrt{1-\varepsilon_v}\right)$
Auracher *et al.* [36]	$\mu = \varepsilon_v/\left(1-0.58\left(1-\varepsilon_v\right)\right)$
Le Gall *et al.* [5]	$\mu = \varepsilon_v/\left(1-0.58\left(1-\varepsilon_v\right)\right) + F10\left(1-\varepsilon_v\right)\varepsilon_v^{10}$

Table 2.4: Correlations of the diffusion resistance factor.
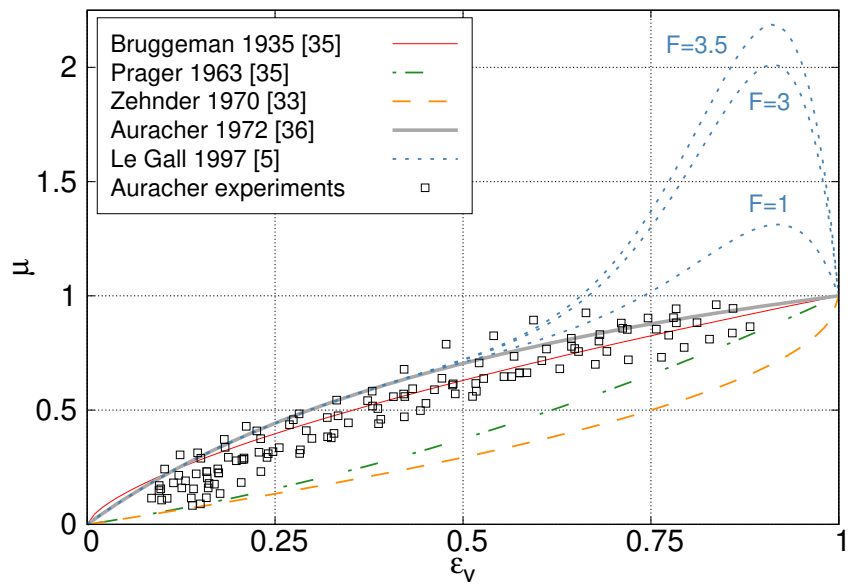
Figure 2.3: Correlations by various authors of the diffusion resistance factor as function of the porosity. Experimental data from Auracher [36].

to provide a correlation by means of experimental data of frost. However, notice that Auracher did not provide experimental values above $\varepsilon = 0.89$. Either Tao *et al.* [4] and Le Gall *et al.* [5] used modifications of Auracher's correlation to correctly capture the evolution of the frost layer under high porosity values. Further discussion is given in Section 2.5.2.

2.4 Numerical implementation

The presented formulation has been implemented into the in-house C++ computer code called *TermoFluids*. *TermoFluids* is an unstructured finite volume flow solver, designed for direct and large-eddy numerical simulation of turbulent flows along with multiphysics problems. The reader is referred to [37] for details on the *TermoFluids* framework that are beyond the scope of this thesis.

2.4.1 Discretization

The pair $\{T, \varepsilon_v\}$ is solved using the finite volume method. Time derivatives are discretized with a first order implicit Euler scheme. Discretization of face values at previous time instant t^n is performed with Central Difference Schemes (CDS), whereas face values at current time t^{n+1} are dealt with diffusive schemes i.e. first order Upwind Differential Schemes (UDS) due to instabilities that may arise near the wall. In addition, the grid velocity is evaluated at the faces of the swept volume:

$$\vec{v}_b = \frac{{}^{\ell}\vec{r}_{f,\text{centroid}}^{\,n+1} - \vec{r}_{f,\text{centroid}}^{\,n}}{\Delta t} \tag{2.27}$$

where the face centroid positions $\vec{r}_{f,\text{centroid}}$ are evaluated at the iteration itself and at the former time step, respectively.

2.4.2 Methodology

The algorithm, which follows a fully implicit time resolution, is presented in Alg. 1, where ℓ refers to the current outer iteration, and m refers to the inner iteration. The calculation of the temperature and porosity distributions follows a Gauss-Seidel method. α_r refers to the underrelaxation factors, implemented as dynamic relaxation factors using the Aitken's Δ^2 method (see Section 2.4.3).

The dynamic movement of the mesh comprehends steps 4, 11 and 12 of the algorithm. The example shown in Fig. 2.4 shows the moving mesh pattern followed within a time step. Notice that in this particular case, the algorithm goes through step 4 of the algorithm twice before the $\Delta y_{\text{fs}}^{n+1}$ convergence is reached in mesh_{it2}.

Algorithm 1 Frost growth - moving mesh method

1:     Initial conditions ($t = 0$): $\{\bar{T}_{\text{fl}} = T_w \, ; y_{\text{fs}}^0 \, ; \bar{\rho}_{\text{fl}}^0 \text{ (see Table 2.5)}\}$
2:     New time step Δt (evaluation of instant t^{n+1})
3:     Extrapolate $^l\Delta y_{\text{fs}}^{n+1} = 2.5\Delta y_{\text{fs}}^n - 2\Delta y_{\text{fs}}^{n-1} + 0.5\Delta y_{\text{fs}}^{n-2}$
4:     Move mesh
5:         Calculate T from Eq. 3.25
6:         Update physical properties ($Y_v, \rho_{\text{ha}}, \rho_v, \rho_{\text{da}}, c_{p,i}, \rho_{\text{fl}}, D_{\text{eff}}, \lambda_i, \lambda_{\text{fl}}, C_{1,2,3,4}$)
7:         Calculate ε_v from Eq. 2.5
8:         **if** $\frac{\|^mT^{n+1} - {}^{m-1}T^{n+1}\|}{\|^{m-1}T^{n+1}\|} > \delta_2$ **and** $\frac{\|^m\varepsilon^{n+1} - {}^{m-1}\varepsilon^{n+1}\|}{\|^{m-1}\varepsilon^{n+1}\|} < \delta_2$ **then**

$$^mT^{n+1,\text{NEW}} = f\left(^{m-1}T^{n+1}, {}^m T^{n+1}, \alpha_r\right),$$
$$^m\varepsilon^{n+1,\text{NEW}} = f\left(^{m-1}\varepsilon^{n+1}, {}^m \varepsilon^{n+1}, \alpha_r\right),$$
          Go to step 5 **endif**

9:         $^mT^{n+1,\text{NEW}} = {}^m T^{n+1}$ and $^m\varepsilon^{n+1,\text{NEW}} = {}^m \varepsilon^{n+1}$
10:        Update physical properties ($Y_v, \rho_{\text{ha}}, \rho_v, \rho_{\text{da}}, c_{p,i}, \rho_{\text{fl}}, D_{\text{eff}}, \lambda_i, \lambda_{\text{fl}}, C_{1,2,3,4}$)
11:    Calculate $\Delta y_{\text{fs}}^{n+1}$ from Eq. 2.14

12:    **if** $\frac{\|^\ell\Delta y_{\text{fs}}^{n+1} - {}^{\ell-1}\Delta y_{\text{fs}}^{n+1}\|}{\|^\ell\Delta y_{\text{fs}}^{n+1}\|} > \delta_1$ **then** Go to step 4 **endif**

13:    **if** $t_{\text{sim}} < t_{\text{end}}$ **then** Go to step 2

       else End of Simulation **endif**

0

7

7

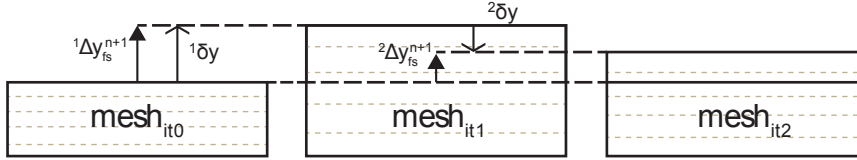
Figure 2.4: Schematized pattern of a 2-outer-iteration mesh movement.

Equation 2.28 displays the amount δy that the mesh has to move at a specific outer iteration. While Δy has a physical meaning (recall its definition given in Section 2.2.3), δy is purely geometrical.

$$^{\ell}\delta y = {}^{\ell}\Delta y_{fs}^{n+1} - {}^{\ell-1}\Delta y_{fs}^{n+1} \tag{2.28}$$

Notice that despite the fact that Δy is positive-definite, δy can take either positive or negative values. No adaptive mesh refinement is used. Thus, the number of control volumes along the simulation remain constant. These are resized after each outer iteration by means of a technique based on a classical elasticity-based mesh update model introduced by Smith and Wright [38] further explained in Appendix.

The $\delta's$ that appear in steps 8 and 12 of the algorithm previously introduced refer to the convergence criteria. The latter are studied along with the time step and the mesh size in order to secure grid independence. The adequate values found are a time step of $10^{-2}s$, and the pair $\{\delta_1 = 10^{-5}, \delta_2 = 10^{-5}\}$ under a single column 30-cell structured mesh.

Different close-to-zero frost layer initial thicknesses are tested. No significant differences are encountered between $y_{fs}^0 = 2 \cdot 10^{-5}m$ and $y_{fs}^0 = 10^{-5}m$, values also tested by Jones and Parker [39], and later used in [7,8,19]. Hence, the present study uses an initial thickness of $10^{-5}m$.

2.4.3 Relaxation factors

An optimized performance of the model is of key importance as applications with complex geometries and vast domains require large amounts of computational time. This Section tackles the aforementioned by testing two types of relaxation factors for the Gauss-Seidel solver: fixed relaxation factor and Aitken's dynamic relaxation method. Note that these are applied in step 8 of the algorithm previously presented.

Variables are updated at each iteration q as follows:

$$^{q}\mathbf{x} = {}^{q-1}\mathbf{x} + {}^{q-1}\alpha_r \, {}^{q}\mathbf{r} \tag{2.29}$$

where α_r is the relaxation factor and $\mathbf{r}$ the residual, defined as:

$$^{q}\mathbf{r} = {}^{q}\tilde{\mathbf{x}} - {}^{q-1}\mathbf{x} \tag{2.30}$$

while x̃ is the unrelaxed calculated variable.

In fixed relaxation factors, a small enough fixed value is assigned for all iterations to keep a stable solution. On the other hand, dynamic relaxation factors follow Aitken's Δ^2 method as stated in Eq. 2.31.

$$^{q-1}\alpha_r = -^{q-2}\alpha_r \frac{^{q-1}\mathbf{r}^T \left(^{q}\mathbf{r} - ^{q-1}\mathbf{r}\right)}{\left|^{q}\mathbf{r} - ^{q-1}\mathbf{r}\right|^2} \tag{2.31}$$

Both fixed and dynamic relaxation factors show a favourable performance and stability. Nevertheless, Aitken's dynamic relaxation method has proved the most efficient based on computational time, taking 50% of the averaged CPU time required by the most adequate fixed relaxation factor.

2.5   Assessment of the model empirical inputs

The empirical inputs needed by the model, i.e. the diffusion resistance factor, the frost layer conductivity, the initial frost mean density and the pressure condition at the air-frost interface are listed in Table 2.5. Several empirical correlations and values have been suggested in literature. However, numerical solutions varying the empirical input parameters show significant differences. Such differences urge to conduct parametric studies in order to determine combinations which give best fits against tested experimental data.

The reference experimental cases studied in this study were chosen with the aim of covering a major region of Hayashi's diagram [2], i.e. covering different types of frost morphologies (see Fig. 2.5). Taking into account the preference of selecting cases with thickness and average density data over time, the full set of experiments tested by Lee *et al.* [11] were chosen. Moreover, in order to give the study greater generality, the test cases by Sahin [40] were also included. A summary of the experimental conditions is given in Table 2.6.

Each of these cases is then simulated, by means of 1D numerical tests, with each of the resulting input combinations obtained from Table 2.5. As an example, an input combination would be Le Gall *et al.* [5] diffusion resistance factor with $F = 2.5$, Na and Webb's [6] frost layer conductivity, an initial frost thickness of $30 kg/m^3$ and a supersaturated condition at the frost-air interface. Note that the heat and mass transfer coefficients are selected based on each specific experiment conditions (see Section 2.5.1). The total amount of input combinations per case is of 414 runs, giving an overall of 2898 runs for the seven cases.

Due to the large number of results, an statistical post-process is made after every simulation in order to find out the best fit of each case. It consists of calculating a modified R-squared value of each output with available experimental data: thickness,

Parameter	Value-Correlation
μ	{ Auracher [36], Prager [35], Zehnder [33], Bruggeman [35], Le Gall *et al.* [5] with $F = \{1 - 10\}$ with intervals of 0.5}
λ_{fl}	{ Na and Webb [6], Lee *et al.* [32], Negrelli *et al.* [30] }
$\bar{\rho}_{\text{fl}}^{0}$	$\{25, 30, 35\}$ kg/m^3
p_{fs}	{Saturated, Supersaturated (when applicable)}

Table 2.5: List of parameters tested in each case.

Case	W $[kg_v/kg_{\text{da}}]$	T_w [°C]	T_∞ [°C]	v $[m/s]$	Data
Lee1 [11]	0.00531	-20	10	1.75	$\{y_{\text{fs}}; \bar{\rho}_{\text{fl}}; T_{\text{fs}}\}$
Lee2 [11]	0.00637	-15	15	2.5	$\{y_{\text{fs}}; \bar{\rho}_{\text{fl}}; T_{\text{fs}}\}$
Lee3 [11]	0.00323	-15	5	1	$\{y_{\text{fs}}; \bar{\rho}_{\text{fl}}; T_{\text{fs}}\}$
Sah1 [40]	0.0069	-9.15	12.85	2.11	$\{y_{\text{fs}}\}$
Sah2 [40]	0.0069	-15.15	12.85	2.11	$\{y_{\text{fs}}\}$
Sah3 [40]	0.007	-25.15	19.85	2.20	$\{y_{\text{fs}}\}$
Sah4 [40]	0.0039	-25.15	12.85	2.10	$\{y_{\text{fs}}\}$

Table 2.6: Chosen experimental conditions and measured data based on Lee *et al.* [11] and Sahin [40] experiments.
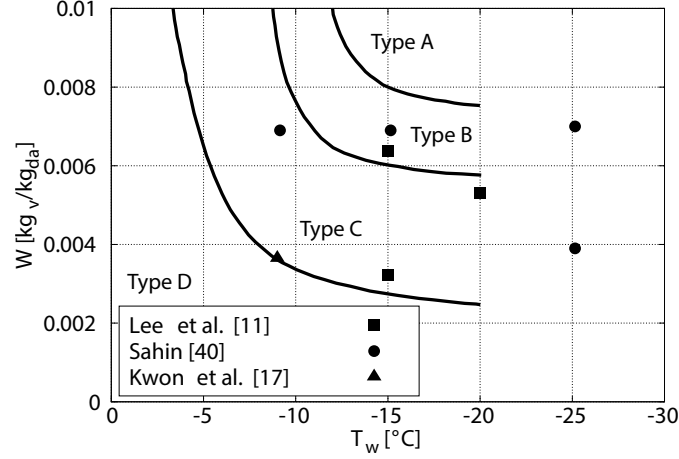
Figure 2.5: Initial state experimental conditions under Hayashi's $\Delta C - T_w$ diagram [2]. Conditions are given in Tables 2.6 and 3.3.

mean density and surface temperature over time. The chosen modified R-squared value is given by:

$$R^2_{\text{mod}} \equiv 1 - \frac{\sum_i \left(\text{num}_i - \text{exp}_i\right)^2}{\sum_i \left(\text{exp}_i - \bar{\text{exp}}\right)^2} \tag{2.32}$$

where $R^2_{\text{mod}} \in (-\infty, 1]$. Recall that a value of 1 correponds to a perfect fit, whereas lowering the R^2_{mod} increases the discrepancies among experimental and numerical data, worsening the output fit. Equation 2.32 differs from the standard definition in its denominator: instead of dividing by the residuals of the numerical solution, residuals of the experimental data are used in order to share a unique normalization for all the runs tested of a certain case.

Due to the large discrepancies encountered when matching the surface temperature (when available), the criterion followed to find the best fit consists of choosing the combination which maximizes the average of $R_{\text{mod},y_{\text{fs}}}$ and $R_{\text{mod},\bar{\rho}_{\text{fl}}}$. In the cases where no mean density data were reported, the best fit will be given by the combination that maximizes the $R_{\text{mod},y_{\text{fs}}}$.

2.5.1 Heat and mass transfer coefficients

Lee *et al.* [11] experimental apparatus (cases `Lee1-Lee3`) consisted of a closed wind tunnel, with a test section of 300 mm long, 150 mm wide and 150 mm high. The thickness was measured by a digital micrometer, and the surface temperature with an infrared thermometer. The mean frost density was obtained by weighing the frost mass. The overall uncertainties were of 5.57% in thickness, 6.94% in frost density, and 4.36% in frost surface temperature.

Instead of using an empirical correlation to calculate the Nusselt number, and eventually the heat transfer coefficient, a mass transfer coefficient was first computed from the available experimental data. The latter was extrapolated from every set of thickness, frost mean density and surface temperature given at a certain time. In particular, a mass transfer coefficient can be obtained by means of a mass balance at the interface:

$$\frac{\mathrm{d}\left(y_{\mathrm{fs}}\rho_{\mathrm{fl}}\right)}{\mathrm{d}t}\bigg|_{t=i} = \left[h_m\left(\rho_{v_\infty} - \rho_{v_{\mathrm{fs}}}\right)\right]\bigg|_{t=i} \tag{2.33}$$

where i refers to the instant where the set of data is evaluated, and where $\rho_{v_{\mathrm{fs}}}$ is obtained at the given surface temperature. The heat transfer coefficient is then computed by means of the previously introduced heat and mass transfer analogy (see Eq. 2.15). The final value is then given by the average of all computed $h_c\,|_{t=i}$.

On the other hand, Sahin [40] experimental set up (cases `Sah1-Sah4`) consisted of an open wind tunnel, with a long entrance rectangular section of 1000 mm long, 254 mm wide and 12.7mm high, followed by a test section of 506 mm long with same aspect ratio. The thickness was measured using two different techniques: using a depth micrometer and the use of a cathetometer. The first being more accurate with an overall uncertainty of ± 0.2 mm.

The averaged Nusselt correlation put forward by Shah (found in [41]) for a thermally developing and hydrodynamically developed flow is hereby used.

$$\mathrm{Nu_{av}} = \begin{cases} 1.849(L^*)^{-1/3} & \text{for} \quad L^* \leq 0.0005 \\ 1.849(L^*)^{-1/3} + 0.6 & \text{for} \quad 0.0005 < L^* \leq 0.0005 \\ 7.541 + \frac{0.0235}{L^*} & \text{for} \quad L^* > 0.006 \end{cases} \tag{2.34}$$

where L^* is the dimensionless distance in the flow direction for the thermal entrance region expressed as:

$$L^* = \frac{L}{D_h \mathrm{RePr}} \tag{2.35}$$

where L is the test section length and D_h the hydraulic diameter.
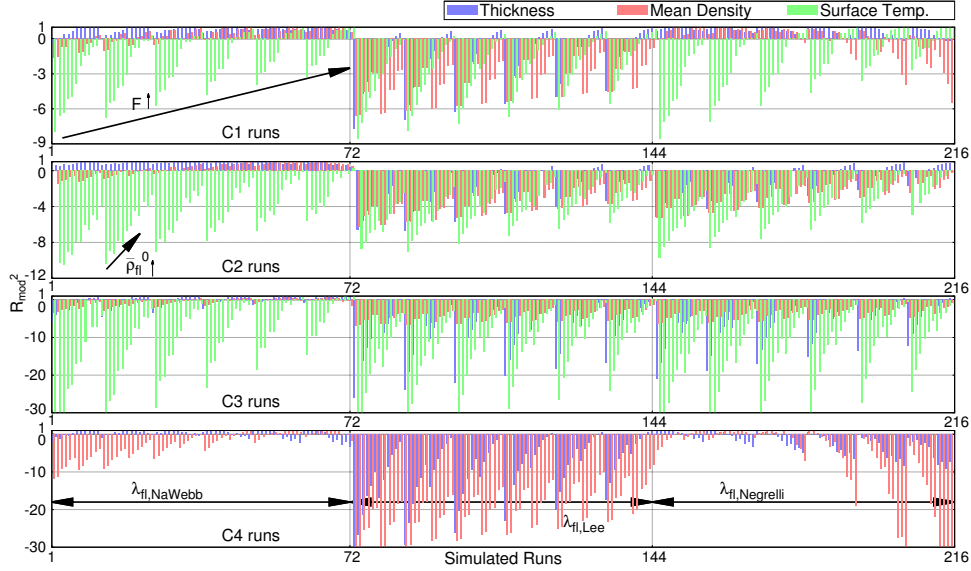
Figure 2.6: R-squared values of the four cases tested in [42] using $\mu > 1$ diffusion resistance factors, i.e., Le Gall's [5] correlation. Each set of two or three columns correspond to the R-squared values of aChanges of λ_{fl}, $\bar{\rho}_{\mathrm{fl}}^0$, F factor, Le and p_{fs} condition are given every 72, 2, 12, 1 and 6 runs, respectively. Periodicities of $\bar{\rho}_{\mathrm{fl}}^0$, F factor and p_{fs} are given every 6, 72 and 12 runs, respectively.

2.5.2   Assessment results

The assessment carried out shows that frost layer thickness results can fit properly through numerous combinations. However, fewer combinations capture the rest of the properties with acceptable accuracy. See Figs. **??** and **??** as examples of the tendecies followed by the cases, different from the present study, analysed in [42]. Note that the solutions give better fits when increasing the factor F or the initial value of the average frost density, and when Na and Webb's frost layer conductivity correlation. Thus, testing a model uniquely against frost thickness measurements does not ensure a proper capture of the physical phenomenon. Furthermore, both thickness and frost mean density represent global values of the problem, which are linked together. This is, whenever using parameters that give an increase to the mean frost density, the thickness decreases and viceversa.

The best combination of empirical inputs found for each case, presented in Table 2.6, is given in Table 2.7. In addition, a comparison of the numerical solutions and the experimental data is shown in Figs. 2.8 and 2.9.
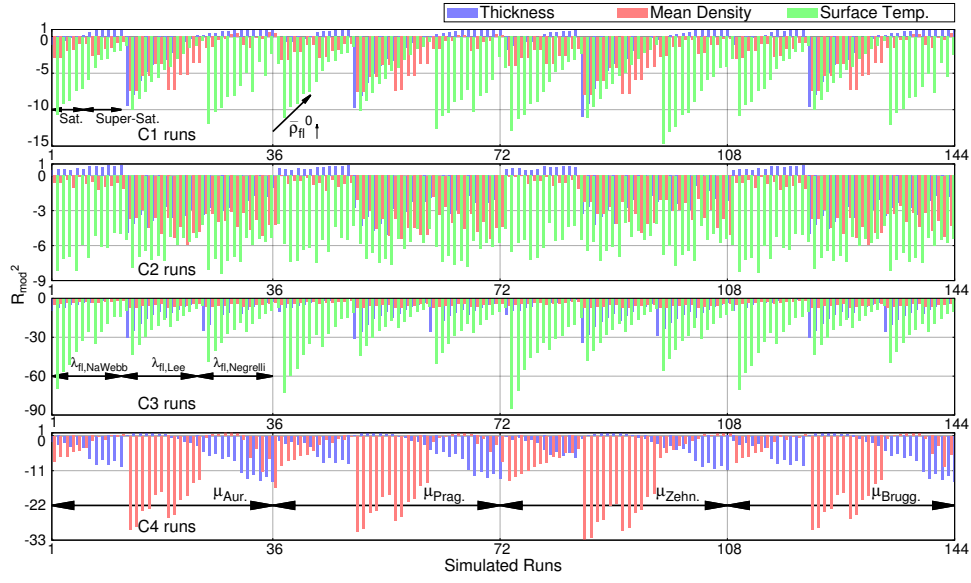
Figure 2.7: R-squared values of the four cases tested in [42], using $\mu < 1$ diffusion resistance factors. Changes of μ, λ_{fl}, $\bar{\rho}_{\text{fl}}^0$, Le and P_{fs} condition are given every 36, 12, 2, 1 and 6 runs, respectively. Periodicities of λ_{fl}, $\bar{\rho}_{\text{fl}}^0$ and p_{fs} are given every 36, 6 and 12 runs, respectively.

Case	μ	λ_{fl}	$\bar{\rho}_{\text{fl}}^0$	P_{fs}	$R^2_{\text{mod},y_{\text{fs}}}$	$R^2_{\text{mod},\bar{\rho}_{\text{fl}}}$
Lee1	Le Gall $F=2$	Negrelli	35	Sat.	0.972	0.960
Lee2	Le Gall $F=3.5$	Na and Webb	35	Sat.	0.951	0.932
Lee3	Le Gall $F=5$	Na and Webb	25	Sat.	0.888	0.701
Sah1	Le Gall $F=6.5$	Na and Webb	35	Sat.	0.962	-
Sah2	Le Gall $F=7$	Na and Webb	35	Sat.	0.995	-
Sah3	Le Gall $F=6.5$	Na and Webb	35	Sat.	0.975	-
Sah4	Le Gall $F=9$	Na and Webb	30	Sat.	0.997	-

Table 2.7: Best fit cases. Units of $\bar{\rho}_{\text{fl}}^0$ are kg/m^3.
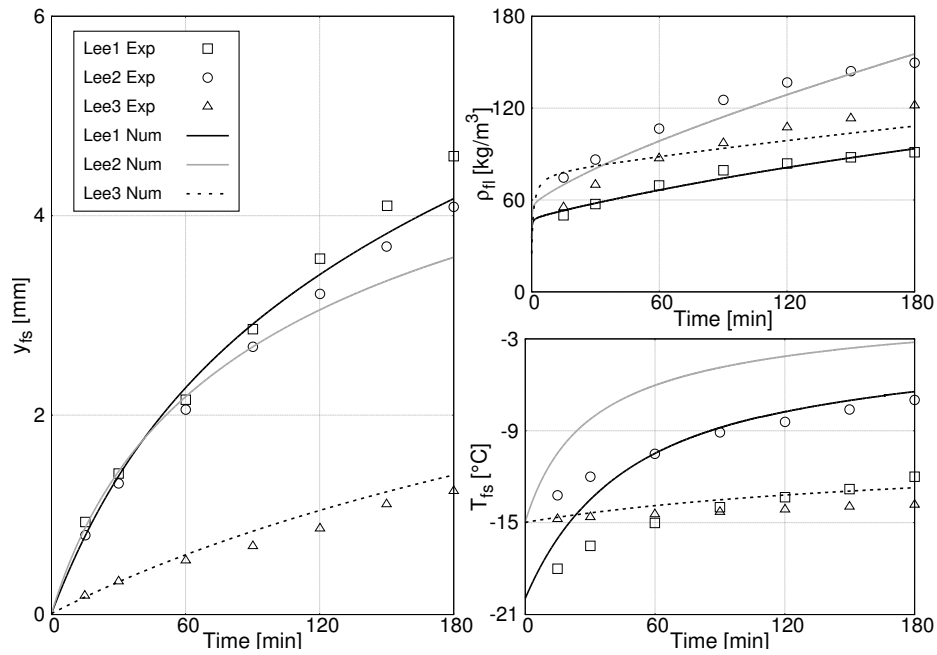
Figure 2.8: Evolution of the thickness, frost mean density and frost surface temperature of Lee's *et al.* cases.
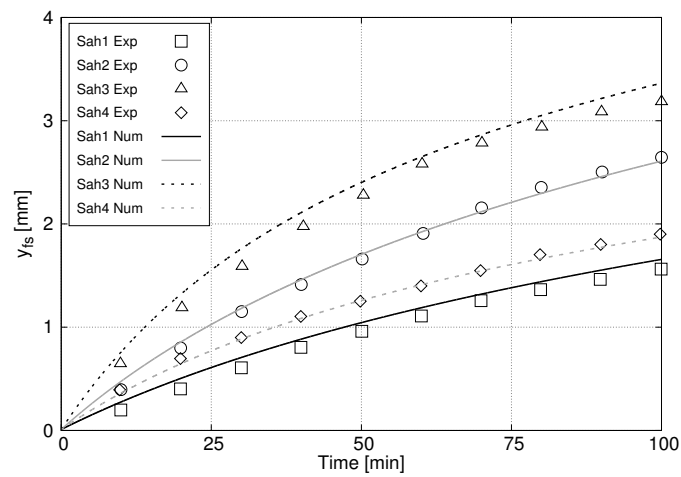
Figure 2.9: Evolution of the thickness of Sahin's cases.

Results ensure that best fits are achieved whenever using diffusion resistance factors above 1. On the other hand, Auracher, Prager, Zehnder and Bruggeman effective diffusivities ($\mu < 1$) show poorer results than Le Gall's correlation, as these tend to underestimate the total deposited mass. Nevertheless, better agreements are reached when increasing the initial mean frost density, using a supersaturated condition at the air-frost interface (whenever applicable), and also when using Na and Webb's or Negrelli's frost layer conductivity correlations rather than Lee's. This is due to the lower ratio observed between the calculated deposited mass and the experiment deposited mass compared to the one resulting from a $\mu > 1$ effective diffusivity, which is enhanced when imposing the supersaturated condition. This results in the fact that some of the solutions provide good agreement of the frost growth, however lacking a proper capture of the other two variables, which usually follow the tendency line although shifted. Indeed, it is difficult not to underestimate the mean frost density when having a good fit of the frost thickness and viceversa.

2.5.3 Physical aspects of the diffusion resistance factor

The former numerical assessment shows not only that the chosen effective diffusivity correlation has a great impact in the numerical solution, but also that diffusion resistance factors with values greater than 1.0 are needed to match experimental data. It is found that whenever using correlations which remain within the range $0 \leq \mu \leq 1$, the observed lower ratio between the calculated and the experimental deposited mass unables an accurate capture of the frost growth evolution.

Na and Webb [19] argued the fact that Le Gall and Tao had used values greater than 1.0, stating that such values could not be physically possible. Indeed, no molecule of water vapour can run through a solid wall. Nevertheless, the fact that frost behaves as a packed bed could be a hasty verdict. In his experiments, Yosida [34] found values much greater than 1.0 in snow (which is very similar to frost). He suggested a hand-to-hand delivery of water vapour from side to side of ice crystals. Later on, Tao and Le Gall also found the need of using higher values of the diffusion resistance factors in order to numerically match their own experiments. The latter gave two other physical explanations. First, the displacement of ice crystals towards the cold wall due to the extreme fragility of frost caused by either thermophoresis acting on small ice nuclei, dissociation of dendritic crystals or a modification of the shear stress caused by the air flow along the frost layer. And second, the rate of densification along the frost layer could act as a pumping force, promoting the mass transfer mechanism. Moreover, notice that Le Gall's correlation shown in Fig. 3.1 follows the trendline of Auracher's at low porosity values, and separates when getting to high porosities. Furthermore, note that the experimental data gathered by Auracher [36] was aquired up to values of $\varepsilon = 0.89$, as shown in Section 2.3.3. No experimental data has yet been provided in the range of $0.89 < \varepsilon \leq 1$.
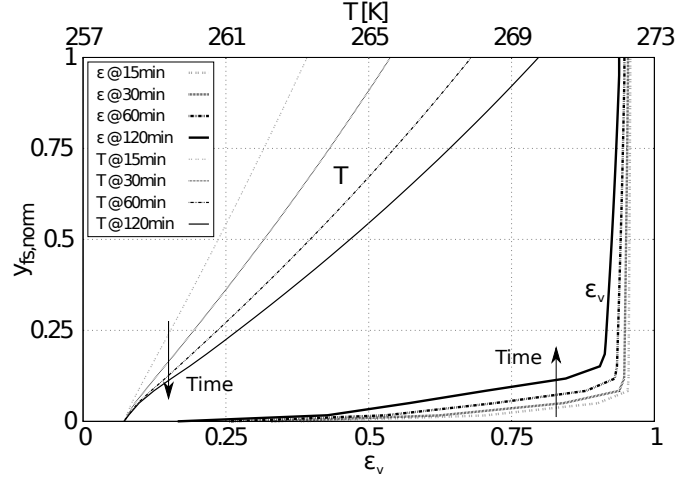
Figure 2.10: Porosity and temperature distributions in the frost layer over time.

Fig. 2.10 shows the distributions of porosity and temperature at different times of a representative example as a function of a normalized frost thickness. It shows that about 80% of the frost layer has porosity values greater than 0.9, a fact also observed in the frost density distributions computed by Na and Webb presented in [6]. Indeed, this characteristic has been found in all the tested numerical experiments. This is remarkable, as the rate of densification is being held mainly close to the cold wall. It is a fact that not only corroborates the possible mechanisms suggested by Le Gall but also, and most outstanding, the fact that convective effects within the frost layer should be taken into account. In the case convective effects were implemented, a reduction of the maximum values of μ would be expected, as water vapour would penetrate easier into the frost layer. Chapter 3 is focused, among other things, on investigating the validity of such an idea. Furthermore, the lack of experimental data within the frost layer highlights, despite its great difficulties, the actual need to perform experiments aiming to study the internal processes within it.

2.6 2D numerical test

The described model, set up through an Arbitrary Lagrangian-Eulerian (ALE) formulation and implemented by means of a finite volume approach, is tested against the experimental case carried out by Kwon *et al.* [17], aiming to complete and verify the conclusions extracted from the previous 1D-studies. The experiment consists of a duct flow with a rectangular cross section of 4mm x 100mm, and a total length of 110
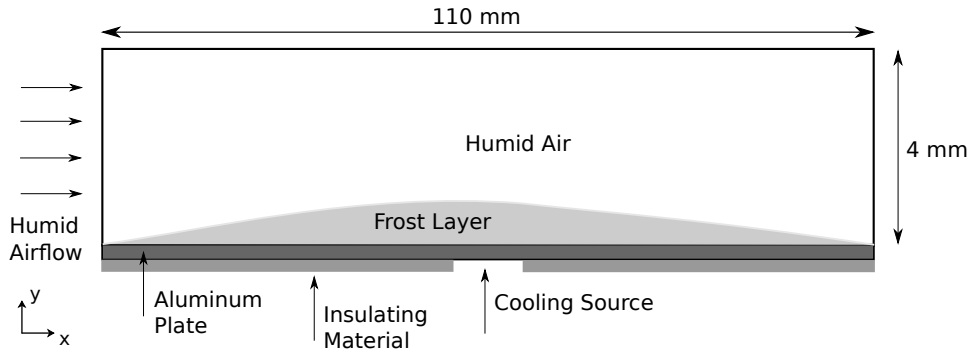
Figure 2.11: Detail of the test section used by Kwon *et al.* [17].

$T_{\text{ha,in}}$ [K]	$v_{\text{ha,in}}$ [m/s]	W_{in} [kg_v/kg_{da}]	$T_{w,\text{center}}$ [K]
275.15	1.5	0.00365	264.15

Table 2.8: Experimental test conditions

mm. A cooling source is placed at the middle-length cross section of the test chamber, below the aluminum plate that constitutes its bottom side. Fig. 3.7 shows a detail of the test section. The tested experimental conditions are given in Table 3.3.

The total mass of frost was measured every 30 min, until 120 min. Frost thickness was also measured at 7 different locations along the test section. Mea- sures were taken every 30 min, till the end of the experimental test (180 min). The wall temperature, shown in Fig. 3.8, was also monitored at 17 different positions at 5, 10, 15, 30, 60, 90, 120, 150 and 180 minutes. In order to take into account the temperature variations at the wall boundary, a stepwise Dirichlet type boundary condition consisting of linear interpolations in both streamwise direction and time is implemented.

Following the conclusions extracted from the grid independence study carried out in Section 2.4.2, the present 2D-study shows the results acquired with a structured mesh of size of 440 x 30 cells, with $\Delta x^0 = 0.25$mm and $\Delta y^0 = 0.33 \cdot 10^{-3}$mm. Note that the growth happens mainly perpendicular to the cold wall. Thus, a small-enough Δx value was chosen such that it would ensure a smooth streamwise transition at the air-frost interface. The model empirical inputs used correspond to Lee3 case (see Table 2.7). This combination is chosen due to the fact that among the set of cases studied in Section 2.5, Lee3 experimental conditions are the closest to the present study in terms of crystal morphology (see Fig. 2.5).

On the other hand, as the goal of the present study is not solving the fluid domain
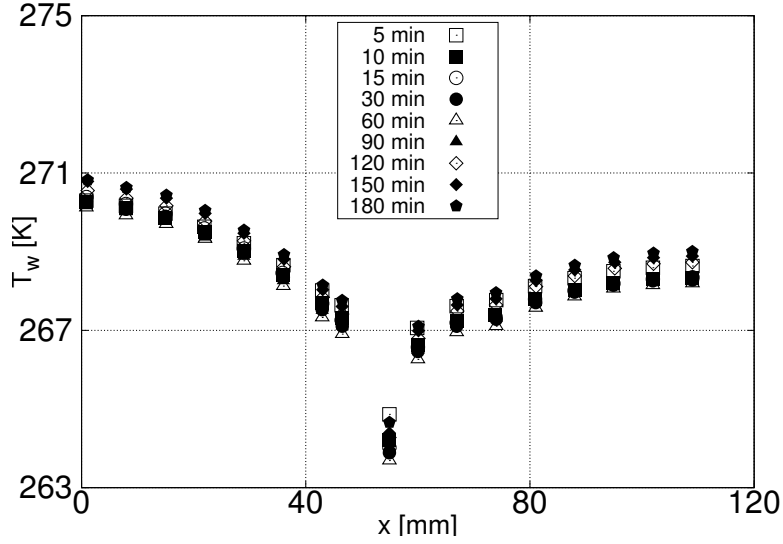
Figure 2.12: Experimental data aquired by Kwon *et al.* [17], and hereby used as a boundary condition for the cold plate.

accurately, but to stress out the methodology used to track the interface using a dynamic mesh, a simplified treatment of the flow is applied. Linear functions for the temperature and the water vapour concentration are used along the streamwise direction. The approximate outlet values, $T_{out} = 274.15K$ and $W_{out} = 0.00336$, have been taken from a previous numerical test using constant values, and have been qualitatively verified against the available Kwon experimental data.

In addition, local heat and mass transfer coefficents are applied. These are found by means of the local Sherwood number correlation put forward by Lombardi and Sparrow [43], which accounts for the combined entry length problem for parallel plates under a thermally and hydrodynamically developing flow with a wall at a uniform temperature and the other insulated.

$$\mathrm{Sh}_x = 0.332 \mathrm{Pr}^{1/3} \left(\frac{\mathrm{Re}}{x/D_h} \right)^{1/2} \left[1 + 7.3 \left(\frac{x/D_h}{\mathrm{Re}} \right)^{1/2} \right]^{1/2}$$
$$\cdot \left[1 + \frac{3.65 \left(\frac{x/D_h}{\mathrm{Re}} \right)^{1/2}}{1 + 7.3 \left(\frac{x/D_h}{\mathrm{Re}} \right)^{1/2}} \right] \quad (2.36)$$

Recall that the Sherwood number is defined as $\mathrm{Sh} = D_h h_m / D_v$.

The steep gradients of the transfer coefficients close to the inlet causes a significant increase of the computational costs. Because of this, a $\mathrm{Sh}_x|_{5\mathrm{mm}}$ is applied when $x \leq 5$ mm.

2.6.1 Test results

The growth of the frost layer is shown in Fig. 3.10 through several thickness profiles at different times. The experimental data gathered by Kwon *et al.* [17], and the numerical solutions given by Wu *et al.* [14] using a static grid under a CFD approach, are also depicted.

Results agree well with the experimental data. However, some differences can be observed: an underpredicted growth found in the upstream region, followed by an initial underprediction of the frost growth in the central region. A behaviour also seen close to the outlet.

In the reported experimental facility, the flow is subjected to a sudden stretchment at the inflow of the duct, shown in Fig. 3.7. The design is such that higher velocities are found close to the inflow, where a thermal boundary layer is being formed. Thus, increasing the heat and mass transfer coefficients as accounted by Eq. 2.36. Wu *et al.*'s model does not capture the increase of growth close to the inlet, presumably due to the fact that the simulation domain was extended 5 additional millimeters and, as a consequence, not considering the enhanced gradients of the temperature and the water vapour close to the inlet. On the contrary, despite the fact that the present model indicates a gradual increase of the frost thickness close to the inlet, the underprediction is due to the fact of using constant heat and mass transfer coefficients for the first 5 mm of the duct, previously explained.

Moreover, because the model uses heat and mass transfer coefficients which take into account the hydraulic diameter of the clean duct, the increase of the flow velocity due to the narrowing of the duct caused by the frost growth is not taken into account. Indeed, in the central region, where the velocity is maximized, a larger heat and mass transfer should be expected. Larger heat and mass transfer coefficients would enhance the initial rate of deposition, as seen in the distributions approximately up to 90 min which lay below the experimental values.

Furthermore, the slight overprediction in the downstream region seen in the profiles beginning at 90 min is atributed to the fact of not accounting for a detailed resolution of the water vapour concentration decay along the duct. Recall that the linear profile used would decrease its slope with time, due to the fact of having a reduced deposition of water vapour given by an increase of the surface temperature.

The evolution of the frost weight over time is shown in Fig. 2.14. Good agreement is found between numerical results and experimental data. Nevertheless, the numerical results show that the deposition tends to slightly decrease with time. This is due
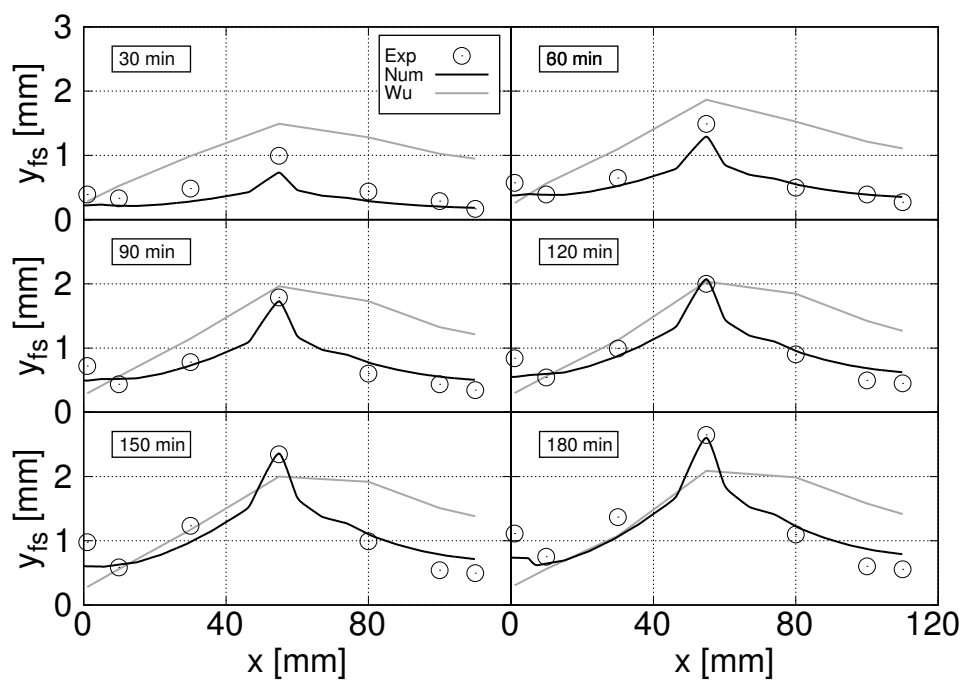
Figure 2.13: Frost thickness distributions. Comparison of the experimental data acquired by Kwon *et al.* [17] with the present model and Wu's *et al.* [14] model.
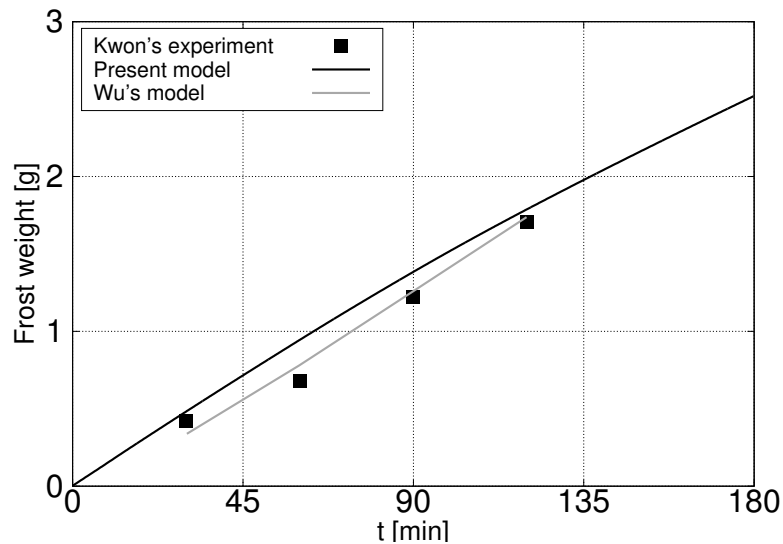
Figure 2.14: Predicted and measured frost weight.

to the reduction of the vapour deposition caused by a continuous diminution of the difference between the frost surface and the external flow temperatures, and also between water vapour densities. The aforementioned reducing effect should balance the increase of deposition due to the continuous strangulation of the channel, as the more the frost layer grows, the larger should the heat and mass transfer coefficients be, enhancing the deposition of the water vapour. On the other hand, the high linearity of the numerical solution given by Wu *et al.*'s model implies that the initial rate of deposition of water vapor suffers an increase during the first 30 min of simulation. This is due to the fact that the number of frost cells in contact with humid air along the duct increases gradually, beginning at the central region where the cooling source is located.

In addition, a set of countour plots ranging from 30 to 180 min is shown in Fig. 3.15. The distributions of the temperature and the porosity show that the regions where the wall temperature is smaller (e.g. the central region), larger growth is reached, and viceversa. However, note that the porosity close to the wall is greater in the central region than in the upstream and downstream areas. This is due to the fact that the rate of phase change in the central region is not sufficient to overcome the increment of the volume due to the frost growth.

Despite the fact that the model is not accounting for a detailed analysis of the external humid air flow, but thanks to the interface tracking method implemented

(a) ε_v@30 min, x :1:100, y :1:1

(b) T@30 min, x :1:100, y :1:1

(c) ε_v@60 min, x :1:100, y :1:2

(d) T@60 min, x :1:100, y :1:2

(e) ε_v@120 min, x :1:100, y :1:3.3

(f) T@120 min, x :1:100, y :1:3.3

(g) ε_v@180 min, x :1:100, y :1:4

(h) T@180 min, x :1:100, y :1:4
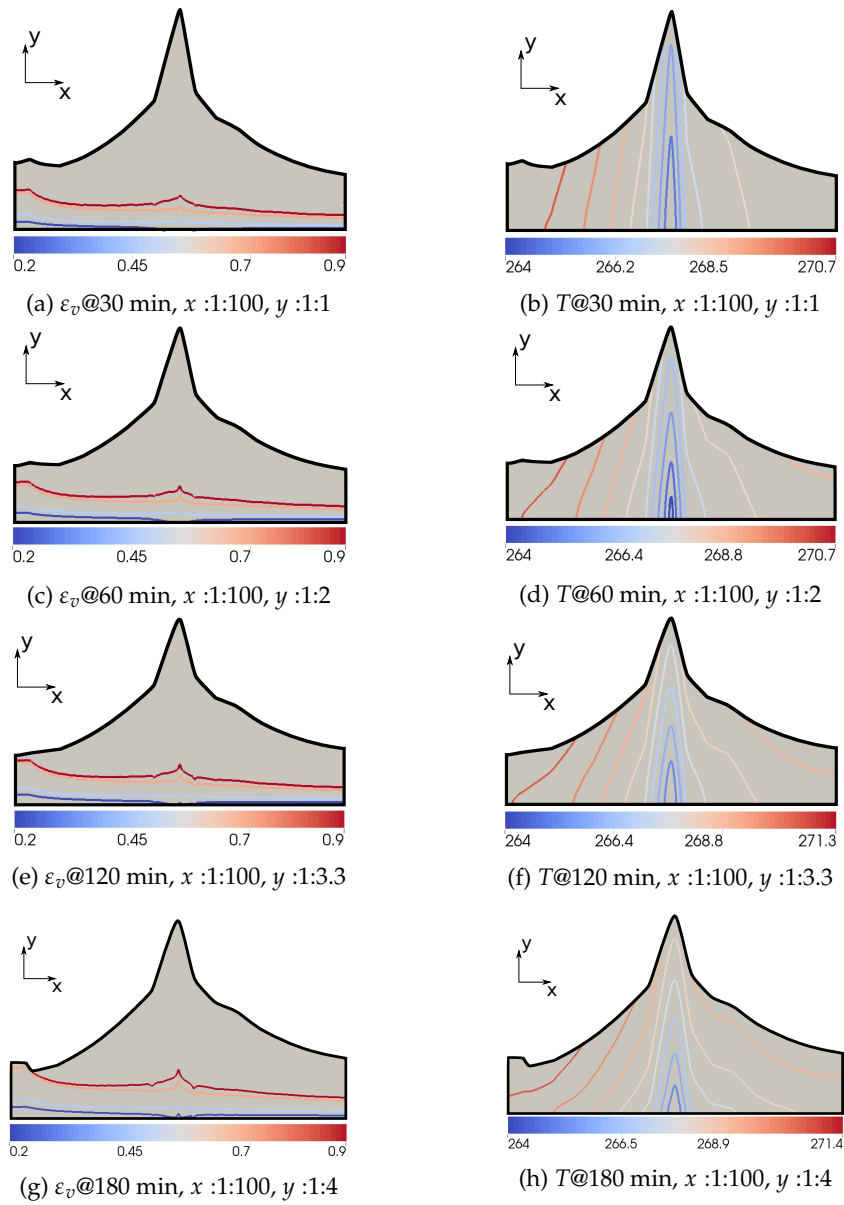
Figure 2.15: Porosity and temperature contour plots over time. x : and y : refer to the applied image scaling.

by means of a dynamic mesh, the solutions reached show that the presented model is able to produce competitive results, which are in reasonable agreement with the experimental data.

2.7   Conclusions

A finite volume method capable to solve the frost growth using dynamic meshes has been presented. The model, based on Tao's formulation, takes into account a growing frost domain. The deformation of the mesh is accomplished by means of a moving mesh method that enables the vertices of the mesh to readapt to given imposed displacements at the interface boundary.

Tackling the problem of frost formation is still a challenge. Despite the many empirical correlations proposed in literature, there is still no agreement on which combinations of parameters better capture the formation pattern. A comprehensive numerical assessment of the empirical inputs of the model with seven reference cases has been carried out by means of more than 2800 numerical tests, resulting on combinations which ensure best fits under the considered experimental conditions. Special attention has been given to the arguments upholding the usage of diffusion resistance factors larger than 1.0 when having high porosity values, $\varepsilon_v \geq 0.9$, as they are needed to capute the frost formation. Due to the fact that a significant part of the frost layer has such values, a new insight has been put forward in regards of attributing the water vapour transport inside the frost layer not only to Fickian diffusion, but also to the convective effects involved in it.

Finally, the model has been tested on a bidimensional case with a non-homogeneous temperature at the wall. Notwithstanding the fact that the external flow is not being solved in detail, solutions show reasonable agreement with experimental data, proving the method to be a valid candidate to simulate frost growth.

References

[1] Kripa K Varanasi, Tao Deng, J David Smith, Ming Hsu, and Nitin Bhate. Frost formation and ice adhesion on superhydrophobic surfaces. *Applied Physics Letters*, 97(23):234102, 2010.

[2] Y. Hayashi, A Aoki, S Adaohi, and K Hori. Study of frost properties correlating with frost formation types. *Journal of Heat Transfer*, 99(May 1977):239–45, 1977.

[3] P. L. T. Brian, R. C. Reid, and Y. T. Shah. Frost deposition on cold surfaces. *Industrial & Engineering Chemistry Fundamentals*, 9(3):375–80, 1970.

[4] Y.-X. Tao, R.W. Besant, and K.S. Rezkallah. A mathematical model for predicting the densification and growth of frost on a flat plate. *International Journal of Heat and Mass Transfer*, 36(2):353–63, 1993.

[5] R. Le Gall, J.M. Grillot, and C. Jallut. Modelling of frost growth and densification. *International Journal of Heat and Mass Transfer*, 40(13):3177–87, 1997.

[6] Byeongchul Na and Ralph L. Webb. New model for frost growth rate. *International Journal of Heat and Mass Transfer*, 47:925–36, 2004.

[7] Bernard Frankovic Kristian Lenic, Anica Trp. Transient two-dimensional model of frost formation on a fin-and-tube heat exchanger. *International Journal of Heat and Mass Transfer*, 52:22–32, 2009.

[8] JM Armengol, CT Salinas, J Xaman, and KAR Ismail. Modeling of frost formation over parallel cold plates considering a two-dimensional growth rate. *International Journal of Thermal Sciences*, 104:245–256, 2016.

[9] Simon Ellgas and Michael Pfitzner. Modeling frost formation within a commercial 3-d cfd code. *Numerical Heat Transfer, Part A: Applications*, 53(5):485–506, 2007.

[10] Donghee Kim, Chiwon Kim, and Kwan-Soo Lee. Frosting model for predicting macroscopic and local frost behaviors on a cold plate. *International Journal of Heat and Mass Transfer*, 82:135–142, 2015.

[11] Kwan-Soo Lee, Sung Jhee, and Dong-Keun Yang. Prediction of the frost formation on a cold flat surface. *International Journal of Heat and Mass Transfer*, 46(20):3789–96, September 2003.

[12] Chiwon Kim, Jaehwan Lee, and Kwan-Soo Lee. Numerical modeling of frost growth and densification on a cold plate using frost formation resistance. *International Journal of Heat and Mass Transfer*, 115:1055–1063, 2017.

[13] J Cui, WZ Li, Y Liu, and ZY Jiang. A new time- and space-dependent model for predicting frost formation. *Applied Thermal Engineering*, 31:447–457, 2011.

[14] Xiaomin Wu, Qiang Ma, Fuqiang Chu, and Shan Hu. Phase change mass transfer model for frost growth and densification. *International Journal of Heat and Mass Transfer*, 96:11–19, 2016.

[15] Eduard Bartrons, PA Galione, Giorgos Papakokkinos, and Carles D Pérez-Segarra. Fixed-grid numerical modeling of frost formation. In *23rd AIAA Computational Fluid Dynamics Conference*, page 4505, 2017.

[16] Xiaomin Wu, Fuqiang Chu, and Qiang Ma. Frosting model based on phase change driving force. *International Journal of Heat and Mass Transfer*, 110:760–767, 2017.

[17] Jeong-Tae Kwon, Hyo Jae Lim, Young-Chul Kwon, Shigeru Koyama, Dong-Hwi Kim, and Chieko Kondou. An experimental study on frosting of laminar air flow on a cold surface with local cooling. *International Journal of Refrigeration*, 29(5):754–760, 2006.

[18] William Woodside. Calculation of the thermal conductivity of porous media. *Canadian Journal of Physics*, 36(7):815–23, 1958.

[19] Byeongchul Na and Ralph L. Webb. Mass transfer on and within a frost layer. *International Journal of Heat and Mass Transfer*, 47(5):899–911, 2004.

[20] Max Kandula. Frost growth and densification in laminar flow over flat surfaces. *International Journal of Heat and Mass Transfer*, 54:3719–31, 2011.

[21] Amne El Cheikh and Anthony Jacobi. A mathematical model for frost growth and densification on flat surfaces. *International Journal of Heat and Mass Transfer*, 77:604–11, 2014.

[22] S Fukusako. Thermophysical properties of ice, snow, and sea ice. *International Journal of Thermophysics*, 11(2):353–372, 1990.

[23] *ASHRAE Handbook Fundamentals*. American Society of Heating, Refrigerating and Air-conditioning Engineers, Inc., si edition edition, 2009.

[24] T. E. Fessler. *WETAIR - a computer code for calculating thermodynamic and transport properties of air-water mixtures*, volume Tech. Report 1466. NASA, 1979.

[25] Joseph Hilsenrath. *Tables of thermodynamic and transport properties of air, argon, carbon dioxide, carbon monoxide, hydrogen, nitrogen, oxygen and steam*. Pergamon Press, 1960.

[26] Hans R Pruppacher, James D Klett, and Pao K Wang. *Microphysics of clouds and precipitation*. Taylor & Francis, 1998.

[27] Ernst Rudolf Georg Eckert and Robert M Drake Jr. *Analysis of heat and mass transfer*. McGraw-Hill, 1972.

[28] D. R. Lide and H. V. Kehiaian. *CRC Handbook of Thermophysical and Thermochemical Data*. CRC Press, 1994.

[29] Kenneth G Libbrecht. The physics of snow crystals. *Reports on progress in physics*, 68(4):855, 2005.

[30] Silvia Negrelli and Christian JL Hermes. A semi-empirical correlation for the thermal conductivity of frost. *International Journal of Refrigeration*, 58:243–52, 2015.

[31] Florent Breque and Maroun Nemer. Frosting modeling on a cold flat plate: Comparison of the different assumptions and impacts on frost growth predictions. *International Journal of Refrigeration*, 69:340–360, 2016.

[32] K S Lee, T H Lee, and W S Kim. Heat and mass transfer of parallel plate heat exchanger under frosting condition. *Korean Journal of Air-Conditioning and Refrigeration Engineering*, 6(2):155–65, 1994.

[33] C T Sanders. *Frost formation. The influence of frost formation and defrosting on the performance of air coolers.* PhD thesis, Technische Hogeschool, Delft (Netherlands), 1974.

[34] Z. Yosida. Physical studies on deposited snow. i: Thermal properties. *Contributions from the Institute of Low Temperature Science*, 7(7):19–74, 1955.

[35] R.E. Cunningham and R.J.J. Williams. *Diffusion in Gases and Porous Media*. New York: Plenum Press, 1980.

[36] H Auracher. Water vapour diffusion and frost formation in capillaries. In *Bulletin of the International Institute of Refrigeration*, pages 477–88, 1972.

[37] Termo fluids s.l., webpage: www.termofluids.com.

[38] Richard W Smith and Jeffrey A Wright. A classical elasticity-based mesh update method for moving and deforming meshes. In *48th AIAA Aerospace Sciences Meeting Including the New Horizons Forum and Aerospace Exposition, Orlando, Florida, Jan. 4-7*, pages 2010–164, 2010.

[39] B.W. Jones and J.D. Parker. Frost formation with varying environmental parameters. *Journal of Heat Transfer*, 97(2):255–259, 1975.

[40] Ahmet Z Şahin. An experimental study on the initiation and growth of frost formation on a horizontal plate. *EXPERIMENTAL HEAT TRANSFER An International Journal*, 7(2):101–119, 1994.

[41] RK Shah and AL London. *Laminar flow forced convection in ducts: a sourcebook for compact heat transfer exchange analytical data*. Academic Press, 1978.

[42] E Bartrons, CD Perez-Segarra, and C Oliet. Frost formation: Optimizing solutions under a finite volume approach. In *Journal of Physics: Conference Series*, volume 745, page 032062. IOP Publishing, 2016.

[43] G Lombardi and EM Sparrow. Measurements of local transfer coefficients for developing laminar flow in flat rectangular ducts. *International Journal of Heat and Mass Transfer*, 17(10):1135–1140, 1974.

Fixed grid numerical modelling of frost growth and densification

Main contents of this chapter have been published in:

E. Bartrons, P. Galione and C-D. Pérez-Segarra, Fixed grid numerical modelling of frost growth and densification, *International Journal of Heat and Mass Transfer*, (under review).

E. Bartrons, P. Galione, G. Papakokkinos and C. D. Pérez-Segarra, Fixed-grid numerical modeling of frost formation, *23rd AIAA Computational Fluid Dynamics Conference*, 4505, 2017.

Abstract. A fixed-grid-porous-media method capable of simulating the growth and densification of frost sheets is here presented. A velocity field is calculated across all the domain, in which a porous media treatment is given to the ice-containing cells. The transported temperature and vapor density are used to define the thermophysical state of each cell, which might enable phase change. As an improvement to Bartrons *et al.*, 2017, the method hereby presented accounts for solidification and sublimation phase transitions. The explicit time step has also been increased by using a semi-implicit treatment of the energy equation. Furthermore, a special boundary condition for cold surfaces has been developed in order to overcome the averaging effect that prevents ice formation in the cells adjacent to the wall. The method is then tested with a study case of a duct flow with a non-homogeneously cooled lower boundary. Several numerical tests are carried out in order to understand the capabilities of the model. The influence of accounting for the convection, as well as the enhanced diffusion resistance factors within the frost layer, is studied by means of the calculated porosity and velocity fields throughout the domain.

3.1   Introduction

The formation of frost is a common phenomenon in nature that involves growth of ice crystals on cold surfaces. The build-up of such porous structures causes malfunctioning in a wide variety of industrial applications, like power transmission line systems, refrigerators and heat exchangers among others. In wind turbines, frost adhesion may be strong under low speed winds [1]. Deicing liquids are often used to remove the nocturnal frost generated on aircraft wings, which adds weight and reduces the aerodynamical performance. Recent studies suggest that frost can also form on aircraft wings during in-flight when crossing supersaturated icing clouds [2]. Hence, providing robust numerical methods to predict the appearance and growth of frost is of key importance to counteract such undesired effects and, as a consequence, improving designs that enhance safety, increase the efficiency and avoid mechanical damage.

The incipient stages of frost formation, triggered by either desublimation or condensation frosting [3], range from an initial heterogeneous nucleation at a surface, until a network of inter-connected frozen droplets is formed. This provides the foundation upon which out-of-plane frost growth can happen. A comprehensive number of studies have modelled the latter from a macroscopical point of view. Based on how equations are set, frost growth models coupled with a free air flow region, using a finite volume approach, can be divided into two main blocks: the two-domain approach and the single-domain approach.

The two-domain approach consists in solving separately the frost and the free air regions. If the implemented frost growth model is 1D (see [4–9] among others), a mesh accounting for the frost domain is not specifically needed [10]. Moreover, it allows implementing a frost growth model with a zero frost thickness initial condition [9]. On the other hand, 2D and 3D frost growth models need a mesh to account for the frost domain, where distributions of the porosity, or the frost density, and the temperature are calculated. These models do need an initial frost thickness [11–13], as the mesh occupies a certain amount of volume. Despite that the results for frost growth remain unaffected when using close to zero initial thicknesses [14], the region where frost will grow must be known in advance. Regardless of the implemented frosting model, either static or dynamic meshes can be used. The first is more common among the literature despite its inherent lack of accuracy when tracking the frost-air interface [10–12]. When dynamic meshes are used, an ALE formulation is set to correct the mass and energy fluxes due to the imposed grid deformations derived from the frost growth [15–18]. The two domains are then coupled by means of a mass and energy balance at the frost-air interface along with a water vapour pressure condition.

There are just a few studies using single-domain approaches (see [19–21]). These do not need an initial frost thickness, fact that not only allows solving the appearance

of frost, but also having several unconnected frost regions growing simultaneously. Similarly to the two-domain approach with a static mesh, the usage of fixed grids compared to deformable grids could dramatically reduce the simulation computational costs and resources, as the mesh does not need to readapt at each iteration. Furthermore, no extra communication between the two domains is required.

The present study sets a single-domain approach method, as an improvement to [22]. The new model, which consists of a single set of equations, accounts for the formation and sublimation of frost by means of a momentum equation for flow through the frost layer (based on the previous works of Galione *et al.* [23, 24], in the line of the works of Hsu and Cheng [25] and Voller and Prakash [26]), as well as a water vapour transport and energy equations that determine the state of a cell, and thus, the phase change. An effort has been put towards maximizing the explicit time step, by evaluating the diffusive term of the energy equation implicitly. Moreover, in order to ensure ice generation close to cold surfaces, a special treatment to such boundaries is here presented.

The proposed model is then used for simulating the case of a duct flow with a non-homogeneously cooled lower surface carried out by Kwon *et al.* [27]. Several numerical tests are conducted with the aim of understanding the capabilities of the model. In particular, the impact to the frost growth when using different porous media treatment, as well as the usage of diffusion resistance factors above 1 is here analysed. Furthermore, a qualitative study of the convective effects within the frost sheet is also discussed.

3.2 Mathematical model

The present analysis assumes that: (a) water vapour, dry air and ice inside the frost layer are in local thermal equilibrium, i.e., $T_{\text{ha}} = T_v = T_{\text{da}} = T_i$; (b) water vapour inside the frost layer is saturated, (c) no movement of the ice crystals is allowed ($\vec{u}_i = 0$), and (d) temporal variation of the mixture density is neglected when calculating the velocity field.

The local volume averaging technique is used, where ε_v represents the volumetric vapour or humid air fraction, which can take values between 0 (ice) and 1 (humid air). The equalty $\varepsilon_v + \varepsilon_i = 1$ must be preserved.

Based on the above-mentioned hypotheses, the resulting volume-averaged governing equations for incompressible flow (global mass, momentum, water vapour transport and energy) are:

$$\frac{\partial \rho_m}{\partial t}^{\;0} + \nabla \cdot (\rho_{\text{ha}} \vec{u}) = 0 \tag{3.1}$$

$$\frac{\partial}{\partial t}(\rho_{ha}\vec{u}) + \nabla \cdot \left(\rho_{ha}\frac{\vec{u}\otimes\vec{u}}{\Xi}\right) = -\nabla p + \nabla \cdot [\mu_{ha}\left(\nabla\vec{u} + (\nabla\vec{u})^T\right)]$$
$$-\frac{2}{3}\nabla\mu\left(\nabla \cdot \vec{u}\right) + \rho_{ha}\varepsilon_v\vec{g} - S\vec{u} \tag{3.2}$$

$$\frac{\partial}{\partial t}(\varepsilon_v\rho_v) + \nabla \cdot (\rho_v\vec{u}) = \nabla \cdot (\rho_{ha}\mu D_v\nabla Y_v) + \dot{\omega}_v \tag{3.3}$$

$$\frac{\partial}{\partial t}(\rho_m h_m) + \nabla \cdot (\rho_{ha}h_{ha}\vec{u}) = \nabla \cdot (\lambda_m\nabla T) + \nabla \cdot [(h_v - h_{da})\rho_{ha}\mu D_v\nabla Y_v] \tag{3.4}$$

where:

$$\rho_m = \varepsilon_v\rho_{ha} + (1 - \varepsilon_v)\rho_i \tag{3.5}$$

$$\rho_m h_m = \varepsilon_v\rho_{ha}h_{ha} + (1 - \varepsilon_v)\rho_i h_i \tag{3.6}$$

$$\rho_{ha} = \rho_v + \rho_{da} \tag{3.7}$$

The presented mass and momentum equations are very similar to the well-known volume-averaged Navier-Stokes (VANS) equations put forward by Whitaker [28] (note that the pressure term of Eq. 3.2 does not contain a volume fraction). The VANS equations have later been extensively used (see for instance [29–31]).

Equation 3.2 corresponds to the momentum equation for flow through a porous medium, where only the Darcian source term, $S\vec{u}$, has been preserved, accounting for the drag force produced by the solid to the fluid flow.

The present study analyzes two forms of the momentum equation:

a) The simplified model for mushy regions put forward by Voller and Prakash [26], where $\Xi = 1$ and $S = S_{VP}$.

b) The porous media model put forward by Hsu and Cheng [25], where $\Xi = \varepsilon_v$ and $S = S_{HC}$.

The selected correlations for the coefficient S are treated in detail in Section 3.3.1.

The water vapour transport and energy equations deduced in [18, 32] are here extended to account for the advective terms. Observe that these terms, which appear in Eqs. 3.1-3.4, contain uniquely the transport of the humid air properties, as the ice phase is assumed to be motionless [23].

The source term $\dot{\omega}_v$ that appears in Eq. 3.3 represents the generation or destruction of water vapour. This value is equally opposite to the generation or destruction of the ice phase, $\dot{\omega}_i$. Hence,

$$\dot{\omega}_v = -\dot{\omega}_i = -\frac{\partial(\varepsilon_i\rho_i)}{\partial t} \tag{3.8}$$

The diffusion resistance factor μ (not to be confused with the dynamic viscosity μ_{ha} in the momentum equation), commonly defined in non-reactive porous media

Author	Diffusion resistance factor
Prager *et al.* [34]	$\mu = 0.5\varepsilon_v \left(1 + \varepsilon_v\right)$
Le Gall *et al.* [16]	$\mu = \varepsilon_v / \left(1 - 0.58 \left(1 - \varepsilon_v\right)\right) + F10 \left(1 - \varepsilon_v\right) \varepsilon_v^{10}$

Table 3.1: Implemented correlations of the diffusion resistance factor.

	Range	ξ
(i)	$-10 < T_w < -4$ °C	$0.283 + e^{-0.020\rho_{\text{fl}}}$
(ii)	$-21 < T_w < -10$ °C	$0.140 + 0.919e^{-0.0142\rho_{\text{fl}}}$
(iii)	$T_w < -21$ °C and $\rho_{\text{fl}} < 200\text{kg/m}^3$	$0.0107 + 0.419e^{-0.00424\rho_{\text{fl}}}$
(iv)	$T_w < -21$ °C and $\rho_{\text{fl}} > 200\text{kg/m}^3$	$0.005\rho_{\text{fl}} \left(0.0107 + 0.419e^{-0.00424\rho_{\text{fl}}}\right)$

Table 3.2: ξ parameter of Na and Webb's effective thermal conductivity correlation.

as $\mu \equiv \varepsilon_v \tau$, is a measure of the added difficulty of the water vapour to flow through the ice crystal pores. However, the former definition does not entirely apply for frost, since an effective mass diffusion is allowed between ice shelves due to temperature gradients ($\mu \neq 0$ in a humid air-ice series arrangement, see Auracher [33]). The correlations used in this study, shown in Table 3.1 and in Fig. 3.1 for different values of ε_v, are the ones proposed by Prager *et al.* [34] and Le Gall *et al.* [16].

On the other hand, the thermal conductivity of the mixture, λ_m, is defined either by means of the Studnikov expression [35] in the humid air region, or by the empirical correlation proposed by Na and Webb [6] within the frost layer. The latter reads as:

$$\lambda_{\text{fl}} = \xi \lambda_{\text{par}} + (1 - \xi) \lambda_{\text{ser}} \tag{3.9}$$

where:

$$\lambda_{\text{par}} = \left(1 - \frac{\rho_{\text{fl}}}{\rho_i}\right) \lambda_{\text{ha}} + \frac{\rho_{\text{fl}}}{\rho_i} \lambda_i$$

$$\lambda_{\text{ser}} = \left[\frac{\rho_{\text{fl}}}{\rho_i} \frac{1}{\lambda_i} + \left(1 - \frac{\rho_{\text{fl}}}{\rho_i}\right) \frac{1}{\lambda_{\text{ha}}}\right]^{-1}$$

And the modeled ξ parameter is given in Table 3.2.

The reader is referred to [18] for a further description of the regarding the implemented correlations of the thermo-physical properties of the model. Furthermore, a detailed comparison of the presented mathematical formulation against the most
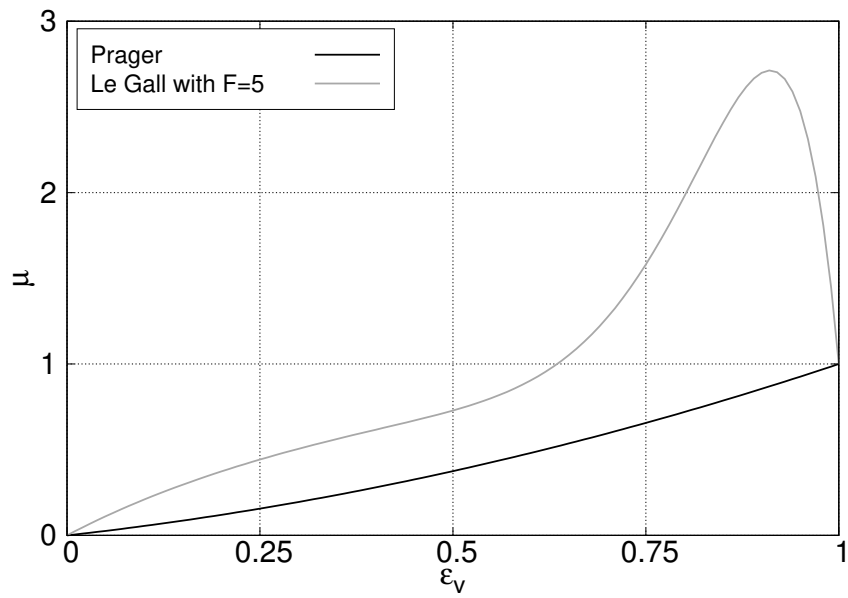
Figure 3.1: Tested diffusion resistance factor correlations. Le Gall *et al.* [16] with and F factor of 5, and the widely used correlation from Prager *et al.* [34].

commonly used in the literature, namely the ones first put forward by Tao *et al.* [15] and Le Gall *et al.* [16], and Na and Webb [6], is developed in Appendix.

3.3 Numerical implementation

The mathematical model is implemented into an in-house C++ computer code called *TermoFluids*. The reader is referred to [36] for details on the *TermoFluids* framework that are beyond the scope of this work. A finite volume approach and a collocated discretization is used along with explicit time integration schemes. In particular, the time integration scheme corresponds to the 2nd order explicit Linear Multi-step method (*k*2LM), in which the time step is dynamically adapted by estimating the upper bounds of the eigenvalues of the convective and the diffusive operators [37].

3.3.1 Mass and momentum

The velocities induced as a result of the density changes (mainly given by phase changes) can be neglected when comparing them to the resulting velocity field of forced convection driven flows. As a consequence, the transient term of the continuity equation (Eq. 3.1) is neglected, as formerly stated by assumption (d). Moreover, due to the fact that the gravitational effects of the problem of study are negligible, the buoyancy term of Eq. 3.2 is also neglected. The resulting time-discretization of the Eqs.3.1 and 3.2 is:

$$\nabla \cdot (\rho_{\mathrm{ha}} \vec{u})^{n+1} = 0 \tag{3.10}$$

$$\frac{(\rho_{\mathrm{ha}} \vec{u})^{n+1} - (\rho_{\mathrm{ha}} \vec{u})^{n}}{\Delta t} = R^{n+\alpha}(\vec{u}) - \nabla p^{n+1} - S\vec{u}^{n+1} \tag{3.11}$$

where $R^{n+\alpha}$ represents the sum of the convective and diffusive terms integrated between time steps n and $n+1$ using some integration scheme (in this case, the above mentioned *k*2LM). The momentum source term is treated implicitly due to stability reasons [23].

Decoupling of $\vec{u}^{n+1}$ and p^{n+1} is carried out applying divergence, imposing mass conservation (Eq. 3.10) and rearranging terms:

$$\Delta t \nabla \cdot \left(\frac{\nabla p^{n+1}}{1 + \Delta t S / \rho_{\mathrm{ha}}} \right) = \nabla \cdot \left(\frac{\rho_{\mathrm{ha}} u^{p}}{1 + \Delta t S / \rho_{\mathrm{ha}}} \right) \tag{3.12}$$

where

$$\rho_{\mathrm{ha}} \vec{u}^{p} = \rho_{\mathrm{ha}} \vec{u}^{n} + \Delta t R^{n+\alpha} \tag{3.13}$$

is a pseudo-predictor velocity. And thus:

$$(\rho_{ha}\vec{u})^{n+1} = \left(\frac{\rho_{ha}\vec{u}^p + \Delta t \nabla p^{n+1}}{1 + \Delta t S / \rho_{ha}} \right) \tag{3.14}$$

from where the new velocity field ($\vec{u}^{n+1}$) is calculated, and where $1/\left(1 + \Delta t S / \rho_{ha}\right)$ acts as a damping factor of the velocity. The desity ρ_{ha} is evaluated at time n because the momentum equation is not iterated with the energy and vapor transport equations. A detailed explanation of the procedure is given in [23,24].

Darcian source term coefficient (S)

The coefficient S can take various forms. In particular, the present study uses two of them. Whenever using the model put forward by Voller and Prakash [26], the following expression is used:

$$S_{VP} = C_{VP} \frac{(1 - \varepsilon_v)^2}{\varepsilon_v^3 + q} \tag{3.15}$$

where C_{VP} is an arbitrary constant and q is a very small value included to avoid division by zero (when $\varepsilon_v \to 0$, S_{VP} increases and consequently convection is strongly reduced).

When the momentum equation corresponds to the one proposed by Hsu and Cheng [25], the preferred expression, deduced from Kozeny-Carman equation, reads as:

$$S_{HC} = \frac{150}{(\psi d_p)^2} \frac{\mu_{ha}(1 - \varepsilon_v)^2}{\varepsilon_v^2} \tag{3.16}$$

Where ψ is the sphericity of the packed bed particles, and d_p the particle diameter. These two values will evidently not be constant throughout the frost layer. Therefore, an expression for d_p, probably depending on ε_v, should be determined in order to accurately simulate the phase change within the frost layer. Due to the fact that such correlation is not available, some arbitrary values are hereby tested using the constant C_{HC}, defined as:

$$C_{HC} \equiv \frac{150}{(\psi d_p)^2} \tag{3.17}$$

The two values used for C_{HC} are set so the resulting damping curves are the most similar to the ones using the tested values of C_{VP}.

As previously stated in Eq. 3.11, the Darcian source term is treated implicitly, from which the coefficient S contributes on the dampening of the velocity through the previously named damping factor. Fig. 3.2 shows the damping produced for different values of C. The results obtained using these values are compared and discussed in Sec. 3.5.
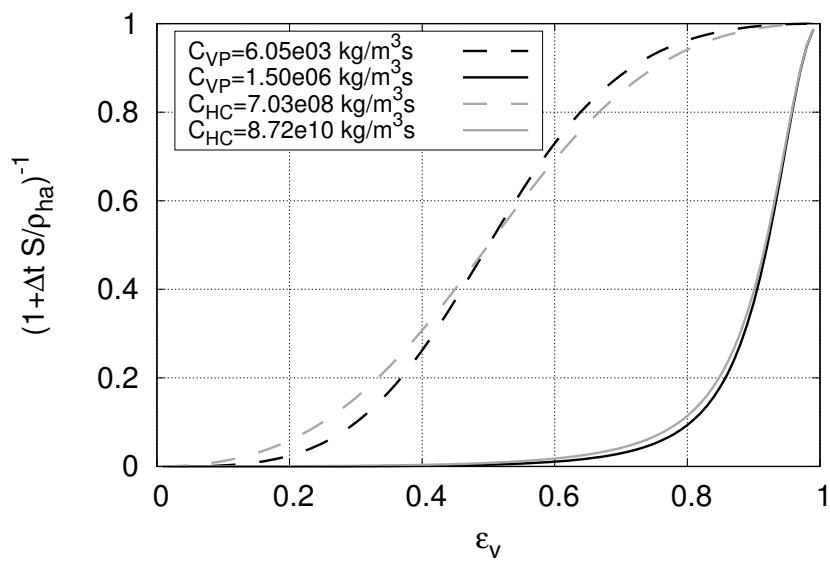
Figure 3.2: Damping factor vs. ε_v for various values of C. Values of $C_{VP} = 6.05e03$ kg/m^{3}s and $C_{HC} = 7.03e08$ kg/m^{3}s have been taken such that the damping factor is 0.5 when $\varepsilon_v = 0.5$.

3.3.2   Water vapour transport

Expressing Eq. 3.3 in a non-conservative form for ρ_v:

$$\varepsilon_v \frac{\partial \rho_v}{\partial t} + \nabla \cdot (\rho_v \vec{u}) = \nabla \cdot (\rho_{\mathrm{ha}} \mu D_v \nabla Y_v) + (\rho_i - \rho_v) \frac{\partial \varepsilon_v}{\partial t} \tag{3.18}$$

It can be seen that the transient source term containing the derivative of the porosity could give stability problems due to the fact that the error in the solution of ρ_v caused by assuming the vapour fraction derivative would grow significantly. Indeed,

$$\frac{\Delta \rho_v}{\rho_v} \propto \left(\frac{\rho_i}{\rho_v} - 1 \right) \frac{\Delta \varepsilon_v}{\varepsilon_v} \tag{3.19}$$

from which the factor $(\rho_i/\rho_v - 1)$ is of the order of 10^5. Hence, a small as 0.1 relative error in ε_v will induce an error in ρ_v of 10^4.

In order to overcome this numerical issue, Eq. 3.3 is separated into two equations: one for ρ_v, which corresponds to Eq. 3.18 and the other for ε_v defined hereafter.

$$(\rho_v - \rho_i) \frac{\partial \varepsilon_v}{\partial t} + \nabla \cdot (\rho_v \vec{u}) = \nabla \cdot (\rho_{\mathrm{ha}} \mu D_v \nabla Y_v) - \varepsilon_v \frac{\partial \rho_v}{\partial t} \tag{3.20}$$

Cells containing ice phase will compute ε_v from Eq. 3.20. Recall that the water vapour in cells with $\varepsilon_v \neq 1$ is under saturated contitions, from which ρ_v is directly calculated by means of the cell temperature. On the contrary, cells containing only humid air will compute ρ_v from Eq. 3.18.

Discretizing Eqs. 3.18 and 3.20 in time:

$$\rho_v^{n+1} = \rho_v^n + \frac{\Delta t}{\varepsilon_v^n} \left[\underbrace{\nabla \cdot (\mu D_v \nabla \rho_v)}_{\mathcal{D}} - \underbrace{\nabla \cdot (\rho_v \vec{u})}_{\mathcal{C}} \right]^{n+\alpha} - \underbrace{(\rho_v^n - \rho_i^n) \frac{\varepsilon_v^{n+1} - \varepsilon_v^n}{\Delta t}}_{\mathcal{S}} \tag{3.21}$$

$$\varepsilon_v^{n+1} = \varepsilon_v^n + \frac{\Delta t}{(\rho_v^n - \rho_i^n)} \left[\underbrace{\nabla \cdot (\mu D_v \nabla \rho_v)}_{\mathcal{D}} - \underbrace{\nabla \cdot (\rho_v \vec{u})}_{\mathcal{C}} \right]^{n+\alpha} - \underbrace{\varepsilon_v^n \frac{\rho_v^{n+1} - \rho_v^n}{\Delta t}}_{\mathcal{S}} \tag{3.22}$$

where $n + \alpha$ refers to the *k*2LM time integration scheme.

A split method is implemented to solve the former. The method consists in solving the convective ($\mathcal{C}$) and diffusive ($\mathcal{D}$) terms explicitly and once per time step, as shown in a simplified form in Eq.3.23.

$$\frac{\phi^* - \phi^n}{\Delta t} = -\mathcal{C}^n + \mathcal{D}^n \tag{3.23}$$
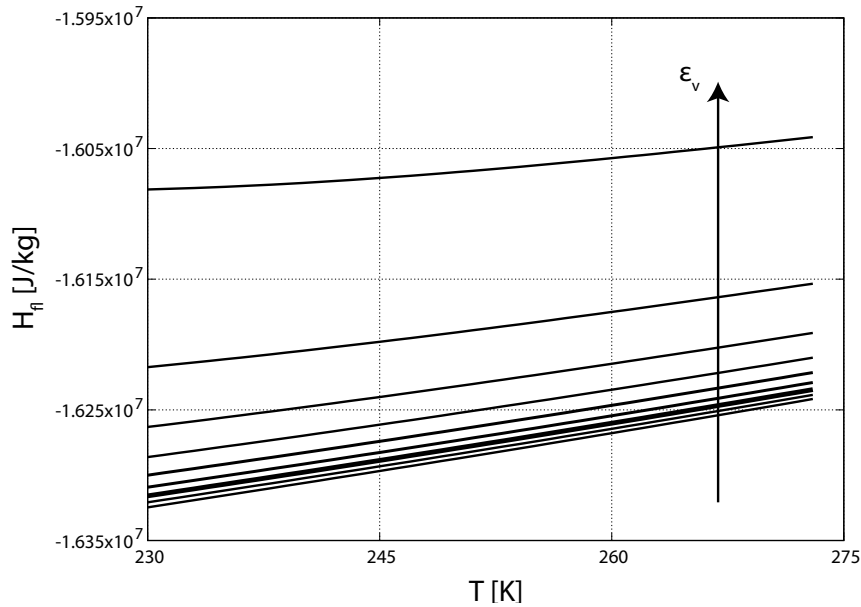
Figure 3.3: H-T dependance. Each curve is given at a fixed ε_v, from values of 0.1 to 0.9 with increments of 0.1.

where ϕ stands for either ρ_v or ε_v. The source term ($\mathcal{S}$), on the contrary, is evaluated between time $n+1$ and n, and reconstructed at each iteration (see step 4 in Alg. 1, Sec. 3.3.4), as shown in Eq.3.24, to obtain ϕ^{n+1}.

$$\frac{\phi^{n+1} - \phi^*}{\Delta t} = -\mathcal{S}^{n+1} \tag{3.24}$$

3.3.3 Energy

The enthalpy-based energy equation given by Eq. 3.4 is rewritten in a non-conservative form in terms of the temperature. This change of the solving variable is preferred because of two main reasons: (a) isolating a temperature from Eq. 3.6 is not an easy task, and most important, (b) a small absolute error in the solution of the enthalpy translates into a big error in the temperature (see Fig. 3.3). The resulting energy equation is:

$$\rho_{\mathrm{fl}}c_{p,\mathrm{fl}}\frac{\partial T}{\partial t} + \nabla \cdot (\rho_{ha}h_{ha}\vec{u}) = \nabla \cdot (\lambda_m \nabla T) + \nabla \cdot [(h_v - h_{da})\,\rho_{\mathrm{ha}}\mu D_v \nabla Y_v]$$
$$-\varepsilon_v h_{\mathrm{ha}}\cancelto{0}{\frac{\partial \rho_{\mathrm{ha}}}{\partial t}} - \rho_{\mathrm{ha}}\varepsilon_v(h_v - h_{\mathrm{da}})\frac{\partial Y_v}{\partial t} - (\rho_{\mathrm{ha}}h_{\mathrm{ha}} - \rho_i h_i)\frac{\partial \varepsilon_v}{\partial t} \tag{3.25}$$

where the source term containing the humid air density derivative over time is neglected due to its very slow changes over time. The frost layer heat capacity, $c_{p,\mathrm{fl}}$, is defined as follows:

$$c_{p,\mathrm{fl}} = \frac{1}{\rho_{\mathrm{fl}}}\left[(1 - \varepsilon_v)\rho_i\bar{c}_{p,i} + \varepsilon_v\rho_{\mathrm{ha}}\bar{c}_{p,\mathrm{ha}}\right] \tag{3.26}$$

where $\bar{c}_{p,i}$ and $\bar{c}_{p,\mathrm{ha}}$ correspond to the averaged values of the specific heat capacity of ice and humid air, respectively.

The convective term is treated explicitly using the k2LM integration scheme. Moreover, due to the fact that the largest eigenvalue among the convective and diffusive terms of the full set of equations (Eqs. 3.2 - 3.4) corresponds to the diffusive term of the energy equation, it is hereby treated implicitly, resulting in an increase of the time step, and a reduction of the computational costs, compared to the one reached in [22]. As a consequence, the limitation of the explicit time step is then given by the eigenvalue of the convective term of the momentum equation.

Because the problem of study imposes a temperature difference (not a water vapor concentration difference), and also the fact that it has been verified that the variations in time of the source term containing the concentration derivative ($\mathcal{S}_{12}$) are generally small, it is evaluated between time n and $n - 1$. On the other hand, the source term containing the time derivative of the porosity is evaluated between time $n + 1$ and n.

The discretized form of Eq. 3.25 is then:

$$T^{n+1} = T^n + \frac{\Delta t}{\left(\rho_{\mathrm{fl}}c_{p,\mathrm{fl}}\right)^n}\left[-\underbrace{\nabla \cdot (\rho_{ha}h_{ha}\vec{u})^{n+\alpha}}_{\mathcal{C}} + \underbrace{\nabla \cdot (\lambda_m \nabla T_m)^{n+1}}_{\mathcal{D}} \right.$$
$$+ \underbrace{\nabla \cdot [(h_v - h_{da})\,\rho_{\mathrm{ha}}\mu D_v \nabla Y_v]^n}_{\mathcal{S}_{11}} - \underbrace{[\rho_{\mathrm{ha}}\varepsilon_v (h_v - h_{\mathrm{da}})]^n \frac{Y_v^n - Y_v^{n-1}}{\Delta t}}_{\mathcal{S}_{12}} \tag{3.27}$$
$$\left. - \underbrace{(\rho_{\mathrm{ha}}h_{\mathrm{ha}} - \rho_i h_i)^n \frac{\varepsilon_v^{n+1} - \varepsilon_v^n}{\Delta t}}_{\mathcal{S}_2} \right]$$

The steps of the implemented split method are detailed in Eqs. 3.28 and 3.29, in which the source term containing the derivative of the porosity, $\mathcal{S}_2$, is rebuilt at each

iteration.

$$\frac{\phi^* - \phi^n}{\Delta t} = -\mathcal{C}^n + \mathcal{S}_{11}^n - \mathcal{S}_{12}^n \tag{3.28}$$

$$\frac{\phi^{n+1} - \phi^*}{\Delta t} = \mathcal{D}^{n+1} - \mathcal{S}_2^{n+1} \tag{3.29}$$

3.3.4 Methodology

The steps of the methodology are herewith summarized in Alg. 1. Due to the fact that most of the industrial applications that include frost growth involve forced convection driven flows, momentum is solved first (step 3) using the well known fractional step method [38]. Next, the transport of vapour (step 5) and the energy equations (step 6) are solved semi-implicitly throughout an iterative process in which the transient source terms are implicitly coupled and updated after each iteration (steps 4, 7 and 8). When the equations converge to a certain tolerance for variables ρ_v, ε_v and T, the calculation of the new time step is began.

The changes in the thermophysical state of a cell are regulated by the control variable `thStateChange`. This variable is set at each control volume, and it can take three values: 0 when there is no change of state (either if the cell remains as a frost cell or a humid air cell), 1 when the cell changes from a fully air containing cell to an ice containing cell, and 2 when the cell changes from a frost cell to a fully air containing cell.

Note that all cells begin with a `thStateChange` = 0. Some of them eventually meet the requirements to form ice, i.e. when the temperature of the cell is below the freezing point and the vapour density is larger than the saturation vapour density at the last calculated temperature. In this case, `thStateChange` is set to 1, fact that will let ε_v be calculated in the following iteration. Note that once an ε_v is calculated for a certain cell, its vapour density will be considered at saturation and thus calculated by means of the new temperature. Moreover, the `thStateChange` will be reset to 0, and will remain 0 as long as that cell contains ice.

In the event that the new calculated temperature of an ice containing cell is higher than the freezing point, `thStateChange` is set to 2. The ice contained in it will sublimate, calculating ρ_v instead of ε_v in the next iteration.

As it has been described, the method takes into account the solidification and the sublimation in the cells, but not the condensation nor the evaporation. Hence, the numerical experiments tested using this methodology should not meet those conditions that would trigger such phase transitions in the actual experiment. A graphical explanation of the limitations of the presented methodology is given in Fig. 3.4.

Algorithm 1 Fixed grid - frost growth method

1: Initial conditions: `thStateChange` = 0
2: New time step Δt
3: Momentum equation
   - Pseudo-predictor velocities u_{ha}^p using previous velocity fields (Eq. 3.13)
   - Pressure eq.: calculation of coefs. and resolution using a linear solver to get p^{n+1} (Eq. 3.12)
   - New velocity field u_{ha}^{n+1} using u_{ha}^p and p^{n+1} (Eq. 3.14)
4: New guessed values Φ^{n+1*}, where $\Phi = \{\rho_v, \varepsilon_v\}$ taken from last iteration
   - Build transient source terms of Eqs. 3.21 , 3.22 and 3.27
5: Water vapour transport equations
   if $\left[\left(\varepsilon_v^{n+1*} == 1\right) \textbf{ and } \left(\rho_v^{n+1} < \rho_{v,\text{ref,sat}}\right) \textbf{ and } (\texttt{thStateChange} == 0)\right] \textbf{ or}$
   $\left(\texttt{thStateChange} == 2\right)$ **then**
       - Solve Eq. 3.21. Variable is vapour density: ρ_v^{n+1}
       - `thStateChange` = 0
   else *that is:* $\left(\varepsilon_v^{n+1*} \neq 1\right)$ *or* $\left(\rho_v^{n+1} \geq \rho_{v,\text{ref,sat}}\right)$ *or*
   $\left(\texttt{thStateChange} == 1\right)$
       - Vapour is saturated. ρ_v will be calculated after calulating T^{n+1}
       - Solve Eq. 3.22. Variable is vapour fraction: ε_v^{n+1}
       if $\left(\varepsilon_v^{n+1} < 1.0\right)$ **then** `thStateChange` = 0
       else $\qquad\qquad\quad \varepsilon_v^{n+1} = 1.0$, `thStateChange` = 2
       end if
   end if
6: Energy equation. Solve Eq. 3.27. Variable is temperature: T^{n+1}
   - Calculate $\rho_{v,\text{sat}}(T^{n+1})$ from tables [39]
   if $(T < 273.15K)$ **then** $\rho_{v,\text{ref,sat}} = \rho_{v,\text{sat}}$
   else $\rho_{v,\text{ref,sat}} = r$, where r is a very big number to avoid passing a phase change condition when being at temperatures above freezing
   end if
   if $\left(\varepsilon_v^{n+1*} == 1\right)$ **and** $\left(\rho_v^{n+1} \geq \rho_{v,\text{ref}}\right)$ **and** $(\texttt{thStateChange} \neq 2)$ **then**
       - `thStateChange` = 1
       - $\rho_v = \rho_{v,\text{sat}}$
   else if $\left(\varepsilon_v^{n+1*} < 1\right)$ **and** $(T < 273.15)$ **then**
       - $\rho_v = \rho_{v,\text{sat}}$
   else if $\left(\varepsilon_v^{n+1*} < 1\right)$ **and** $(T > 273.15)$ **then**
       - `thStateChange` = 2
       - $\varepsilon_v = 1$
   end if
7: Update ρ_{ha} (in order to update such value, Y_v must also be updated)
8: **if** $|\varepsilon_v^{n+1} - \varepsilon_v^{n+1*}| > \delta$ **or** $|T^{n+1} - T^{n+1*}| > \delta$ **or** $|\rho_v^{n+1} - \rho_v^{n+1*}| > \delta$ **then**
       - $\Phi^{n+1*} = \Phi^{n+1}$
       - Go to 5
   else
       - Update (by order): ρ_{fl}, Y_v, thermophysical properties and h_{ha}
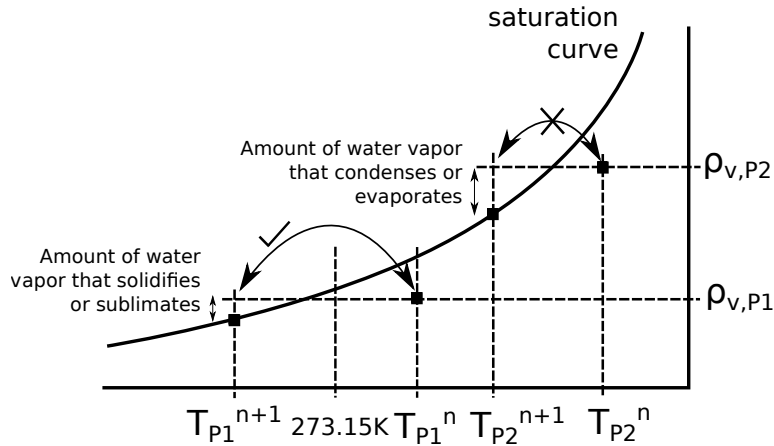   - Go to 2
   end if

Figure 3.4: Capabilities and restrictions of the model. Possible phase change cases of a cell P1 solidifying or sublimating and a cell P2 condensing or evaporating are here depicted.

3.3.5 Special wall boundary condition

As previously discussed, the change of state of a cell occurs when the combination of the average temperature and vapour density values surpass the saturation curve (given that the temperature is below the freezing point). It is obvious that the amount of time needed by a fully humid-air-containing cell, neighbouring and ice-containing cell, to change its phase, will be directly related to the size of that cell. The smaller the cell is, the closer its temperature will be to that of its saturated neighbour, allowing an earlier generation of ice in it. Note that the cell size dependency to the phase change will only affect the accuracy at which the frost-air interface is being tracked, but not necessarily the average growth velocity of the frost, which depends on the accuracy in the spatial representation of the relevant fields (T, ρ_v, ε_v). Certainly, a larger size of a humid air cell will require its ice neighbouring cell to densify more before meeting the requirements to change its phase. However, once it becomes a frost cell, the space gained by the frost front will also be larger.

The former explanation is only valid if the domain already contains frost cells, as the latter densify and eventually let the neighbouring humid air cells change of phase. This section tackles the problem when still not having frost cells: depite that the conditions at the cold surface ensure the formation of ice at the wall, the humid air cells in which the cold surface is contained are big enough so their average temperature never reduces till a point where phase change can happen. This lack of ice being formed in cells attached to the wall and that would actually meet the conditions for frosting (only because of the wall temperature, not because of the

average cell temperature), is the one atributed to the size of the mesh.

A solution to this instrinsic problem of finite volume approaches, while maintaining coarse-enough meshes, is addressed here by means of a boundary contition that allows the accumulation of water vapour at the wall in the form of ice. This ice is artificially accumulated at the wall until the summation of the density of water vapour at the cell node and the one equivalent to the accumulated ice is larger than the saturated vapour density at the wall temperature, thus activating a phase change.

The algorithm associated to this boundary condition is presented in Alg. 2. In particular, when the temperature at the wall is below the dew and freezing points (see condition given in step 2 and shown in Fig. 3.5), ice should deposit on its surface. At this point, the vapor density zero derivative used as the default boundary condition is stopped being applied.

The total deposited ice over a period of time reads as:

$$m_{i,\text{added}} = \int_0^t \dot{m}_v'' S dt \tag{3.30}$$

Where $\dot{m}_v''$ is the water vapor mass flux at the wall:

$$\dot{m}_v'' = D_v \nabla \rho_v\big|_W \hat{n}_W \tag{3.31}$$

The added mass of ice at the wall is stored as an equivalent water vapor volume fraction of the belonging cell:

$$\varepsilon_{v,W}' = \varepsilon_{v,W}' - V_{i,\text{added}}/V_{\text{cell}} \tag{3.32}$$

Where $V_{i,\text{added}} = m_{i,\text{added}}/\rho_i$. This volume fraction is then translated into an equivalent water vapour density, in step 4, as follows:

$$\rho_{v,\text{equiv}} = \rho_{v,P} + \rho_i \left(1 - \varepsilon_{v,W}'\right) \tag{3.33}$$

Where P stands for the cell central node. The cumulative value $\rho_{v,\text{equiv}}$ might eventually surpass the one from the saturation state at the averaged cell temperature (calculated in step 6 of Alg. 1). If the condition is satisfied, the cell state must change to frost. The variable `thStateChange` is then set to 1 in order to calculate ε_v in next iteration.

The implementation of this boundary condition is placed after step 6 of Alg. 1. The artificial variable ε_v' (not to be confused with ε_v) is only used for the purpose of this boundary condition. Moreover, once a cell starts being treated as a frost cell, this boundary condition is disapplied.

Algorithm 2 Boundary condition: vapour accumulation at the wall

---

1:     Initial conditions: $\varepsilon'_v = 1$ (set along with `thStateChange` in step
     1 of Alg. 1)
     - Following steps placed after step 6 of Alg. 1

2:     **if** $(T_W < T_{\text{dew},P})$ **and** $(T_W \leq 273.15K)$ **then** $\rho_{v,W} = \rho_{v,\text{sat}}\big|_{T_W}$ (see Fig.3.5)
     else $\rho_{v,W} = \rho_{v,P}$ (see Fig.3.6)
     end if

3:     **if** $\left(\rho_{v,P} \neq \rho'_{v,W}\right)$ **then**
        - $\dot{m}''_{i,\text{added}} = D_v \nabla \rho_v\big|_W \hat{n}_W$, where $\nabla \rho_v\big|_W \approx (\rho_{v,P} - \rho_{v,W}) / (\vec{d}_{PW} \cdot \hat{n}_W)$
        - $V_{i,\text{added}} = \left(\dot{m}''_{i,\text{added}} S_W \Delta t\right) / \rho_i$
        - $\varepsilon'_{v,W} = \varepsilon'_{v,W} - V_{i,\text{added}} / V_{\text{cell}}$
     else $\varepsilon'_{v,W} = \varepsilon_{v,P}$
     end if

4:     **if** $\left(\varepsilon'_{v,W} \neq 1\right)$ **and** $(\varepsilon_{v,P} == 1)$ **then**
        - $\rho_{v,\text{equiv}} = \rho_{v,P} + \rho_i \left(1 - \varepsilon'_{v,W}\right)$
       if $\left(\rho_{v,\text{equiv}} > \rho_{v,sat}\big|_{T_P}\right)$ **then**
           - `thStateChange = 1`
           - $\rho_v^n = \rho_{v,\text{equiv}}$ and $\rho_v^{n+1*} = \rho_{v,\text{ref},P}$ when building the
             transient source terms in step 4 of Alg. 1
           - $\varepsilon'_v = 1$
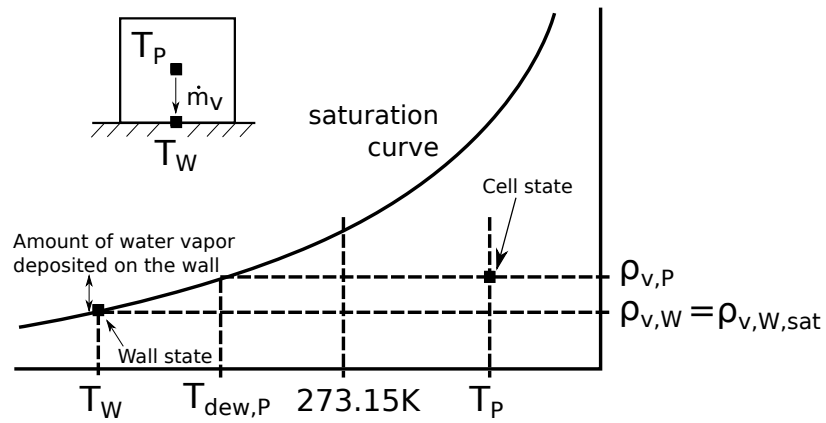   **end if**
     end if

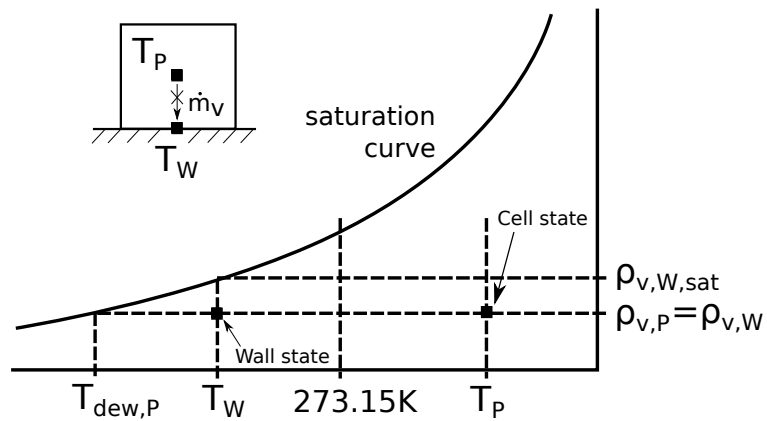Figure 3.5: Conditions enabling phase change at the wall.
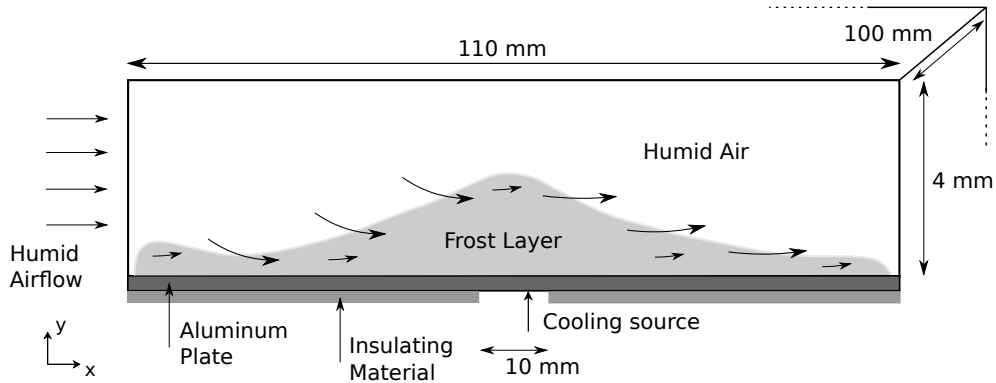

Figure 3.6: No phase change occuring at the wall.

Figure 3.7: Detail of the test section used by Kwon *et al.* [27].

$T_{ha,in}$ [K]	$v_{ha,in}$ $[m/s]$	W_{in} $[kg_v/kg_{da}]$	$T_W(x,t)$ [K]
275.15	1.5	0.00365	see Fig.3.8

Table 3.3: Experimental test conditions

3.4   Numerical experiment

The experimental case, carried out by Kwon *et al.* [27], consists of a duct flow with a rectangular cross section of 4 mm x 100 mm, and a total length of 110 mm. A cooling source of 10 mm wide is placed at the middle-length cross section of the test chamber, below the aluminum plate that constitutes the bottom side of the channel. Fig. 3.7 shows a detail of the test section. The tested experimental conditions are given in Table 3.3.

The total mass of frost was measured every 30 min, until 120 min. Frost thickness was also measured at 7 different locations along the test section. Measures were taken every 30 min, till the end of the experimental test (180 min).

The wall temperature, shown in Fig. 3.8, was monitored at 17 different positions at 5, 10, 15, 30, 60, 90, 120, 150 and 180 minutes. In order to take into account the temperature variations at the wall boundary, a stepwise Dirichlet type boundary condition consisting of bilinear interpolations in both streamwise direction and time is implemented.

Furthermore, a uniform inlet velocity boundary condition is used. This boundary condition is preferred over the parabolic profile formerly used in [22], as the increased experimental thickness values close to the inlet suggest the existence of enhanced
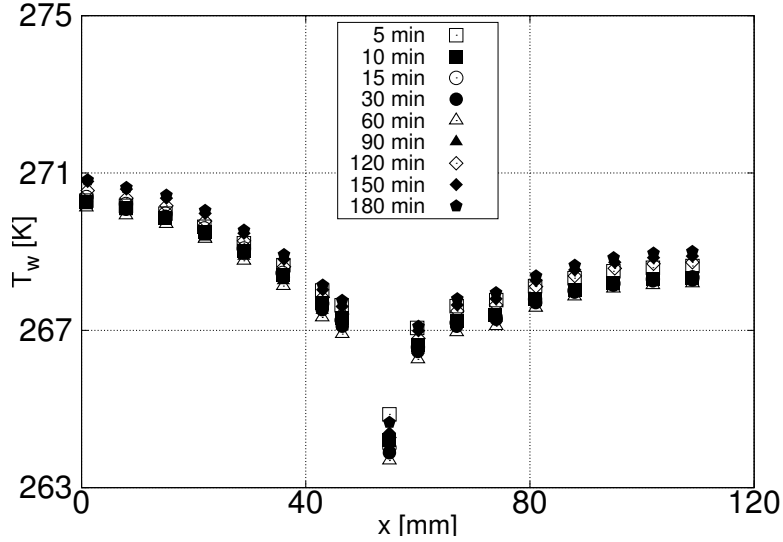
Figure 3.8: Experimental data aquired by Kwon *et al.* [27], and hereby used as a wall temperature boundary condition for the bottom wall.

gradients in that region.

A summary of the specified boundary conditions is given in Table 3.4.

As previously explained, the *TermoFluids* code uses explicit time integration schemes for the momentum equation. Due to the fact that frost growth experiments usually range between 1 to 3 hours, the size of the mesh cells needs to be as large as possible while preserving the grid independence in order not to reach too small time steps. Figure 3.9 shows a grid independence study with three different meshes with $\{\Delta x, \Delta y\}$-pairs of $\{0.25, 0.2\}$mm, $\{0.5, 0.4\}$mm and $\{0.7, 0.6\}$mm. The study shows good agreement of the accumulated frost among the three meshes. Furthermore, the mesh comparison carried out in [22] also showed that the rate of ice deposition is almost unchanged when changing from meshes with cell sizes of $\{1, 1\}$mm to $\{0.1, 0.1\}$mm. As a consequence, and recalling that the main purpose of the present study is to introduce and emphasize a new methodology capable to simulate the frost growth, the present 2D-study shows the results acquired with a uniform structured mesh of 220 x 10 cells, with $\Delta x = 0.5$mm and $\Delta y = 0.4$mm. The mesh size and the given numerical integration schemes (see Sec. 3.3) lead to time steps of the order of 10^{-4} to $10^{-5}s$. Ongoing work is focused on the implementation of fully implicit integration schemes, so computationally less consuming simulations are performed.

Furthermore, despite the fact that in [22], an extra 5 mm domain had been added to the inlet and outlet boundaries to avoid possible numerical instabilities as previously

77

Table 3.4: Boundary conditions

Side	v	p	ρ_v	ε_v	T
Bottom wall*	0	$\partial p/\partial n = 0$	$\partial \rho_v/\partial n = 0$	$\partial \varepsilon_v/\partial n = 0$	$T_W(x,t)^\dagger$
Upper wall	0	$\partial p/\partial n = 0$	$\partial \rho_v/\partial n = 0$	$\partial \varepsilon_v/\partial n = 0$	$\partial T/\partial n = 0$
Inlet	$v_{\text{ha,in}}$	$\partial p/\partial n = 0$	$\rho_{v,\text{in}}$	$\partial \varepsilon_v/\partial n = 0$	$T_{\text{ha,in}}$
Outlet	$\partial v/\partial n = 0$	0	$\partial \rho_v/\partial n = 0$	$\partial \varepsilon_v/\partial n = 0$	$\partial T/\partial n = 0$

* Contains the special treatment explained in Sec.3.3.5.
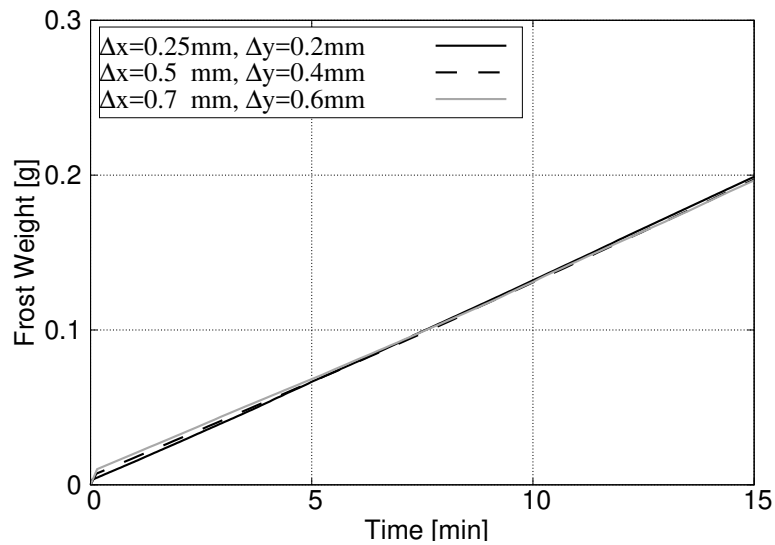† Bilinear interpolation of the experimental data, shown in Fig. 3.8.

Figure 3.9: Grid independence study. The model parameters correspond to case `VP_high_Prag` defined in Table 3.5.

suggested by Wu *et al.* [20], the methodology hereby presented gives a stable solution close to the inflow and to the outflow, regardless of how close is the boundary to the growing frost sheet. Hence, the computed domain consists of 110 mm in the streamwise direction. Moreover, not accounting for the added domain close to the inlet as well as imposing uniform inflow boundary conditions, allows solving the enhanced gradients generated in that region, which produce larger frost growths (notice the experimental points measured at $x = 1$mm in Fig. 3.15).

3.5   Numerical tests

The dynamic mesh method presented in [18], which neglected the convection within the frost sheet, reported porosity values above 0.9 in approximately 80% of the frost layer thickness. In this method, an artificially enhanced diffusion resistance factor ($\mu > 1$) was needed in order to match the experiments, namely, Le Gall's correlation [16] with a factor F=5. Accurate results were found for the thickness profiles and the deposited mass. However, despite the aforementioned porosity distributions agreed with the numerical results obtained by Na and Webb [6], the resulting morphology of the frost layer remained unknown, as no such data is yet to be reported experimentally. Hence, the implementation of the fixed grid method was a motivation to give more clarity into two main aspects. First, whether the porosity distributions within the frost layer are similar to the ones obtained using the dynamic mesh method. And second, whether an enhanced diffusion resistance factor is still needed (as in the dynamic mesh method) if the convection within the frost layer is being accounted.

The numerical tests carried out in this study were designed both aiming to give answers to the former, which will be later discussed in Sec.3.5.2, as well as to study the behaviour of the presented model. A summary of the selected tests is shown in Table 3.5. In particular, the goal is to study:

- The differences between the two types of porous media treatment presented in Sec. 3.2, $\Xi = [1, \varepsilon_v]$, while maintaining the Darcian source terms as similar as possible, i.e., a C_{VP} and C_{HC} such that $S_{\text{VP}} \approx S_{\text{HC}}$.

- The impact of the velocity damping factor, directly related to the constant $C_{\text{VP,HC}}$ of the Darcian source term.

- The effect of using artificially increased diffusion resistance factors.

Case	Momentum model	Ξ	$C_{VP,HC}$	μ
VP_high_Prag	Voller and Prakash [26]	1	1.50e06	Prager *et al.* [34]
VP_low_Prag	Voller and Prakash [26]	1	6.05e03	Prager *et al.* [34]
HC_high_Prag	Hsu and Cheng [25]	ε_v	8.72e10	Prager *et al.* [34]
HC_low_Prag	Hsu and Cheng [25]	ε_v	7.03e08	Prager *et al.* [34]
VP_low_Gall	Voller and Prakash [26]	1	6.05e03	Le Gall *et al.* [16], F=5

Table 3.5: Tested numerical models.

3.5.1 Results

The thickness distributions of the frost layer at different instants is shown in Fig. 3.10. Each distribution corresponds to each of the cases listed in Table 3.5. Due to the fact that using a static mesh does not allow a fully accurate tracking of the air-frost interface (the air-frost interface is located within the limits of the ice containing cells that have fully air containing cells neighbours), the thickness distributions shown in Fig. 3.10 correspond to contour plots at $\varepsilon_v = 0.99$. Note that using an $\varepsilon_v = 1$ contour condition would imply defining the frost-air interface at the very edges between ice containing cells and fully air containing cells, regardless the amount of deposited ice in the latter. In addition, the evolution of the accumulated frost weight at the lower boundary of the duct is shown in Fig.3.11. The experimental data gathered by Kwon *et al.* [27] is also depicted in both figures. The numerical tests are solved up to 90 min, as the authors find it a more than adequate elapsed time to represent the behaviour of each case's set up. Results up to 180 min are also shown for case VP_high_Prag.

A comparison of the solutions of the porosity and temperature distributions, as well as the velocity field, of cases VP_high_Prag, VP_low_Prag and VP_low_Gall at 60 min is also provided in Figs.3.12, 3.13 and 3.14. Furthermore, the porosity distributions up to 180 min of case VP_high_Prag are depicted in Fig.3.15.

Solutions show almost no differences between the two types of porous media treatment given to the convective term of the momentum equation with large C-values (see that cases VP_high_Prag and HC_high_Prag appear overlaped in Figs. 3.10 and 3.11). Only very slight variations arise when using lower values of C (see cases VP_low_Prag and HC_low_Prag in Figs. 3.10 and 3.11), due to the fact that the expressions given in Eqs.3.15 and 3.16 move further apart as ε_v takes lower values (see Fig. 3.2). Therefore, the simplification of the porous media treatment put forward by Voller and Prakash [26] for mushy regions ($\Xi = 1$), in comparison with the one of Hsu and Cheng [25] ($\Xi = \varepsilon_v$), seems to give good enough approximations when solving the frost growth under the tested C-values.
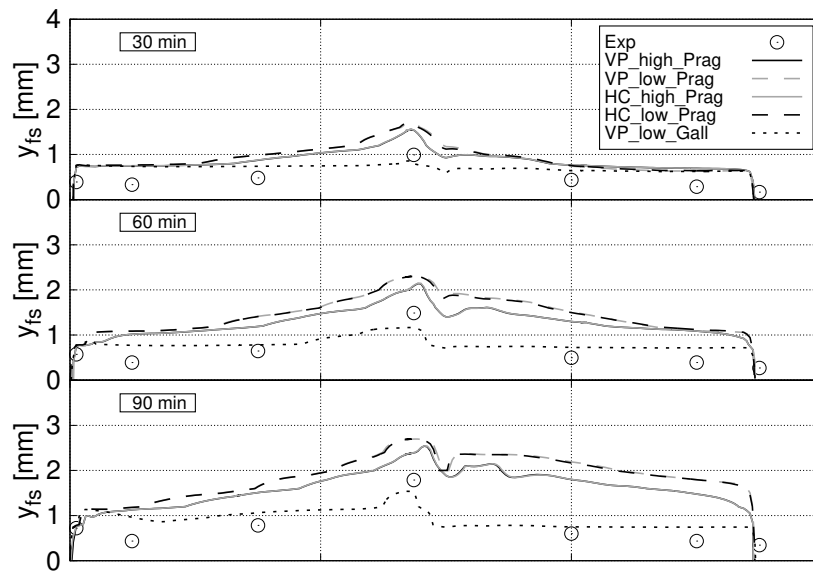
Figure 3.10: Frost thickness distributions given at $\varepsilon_v = 0.99$. Comparison with the experimental data acquired by Kwon *et al.* [27].
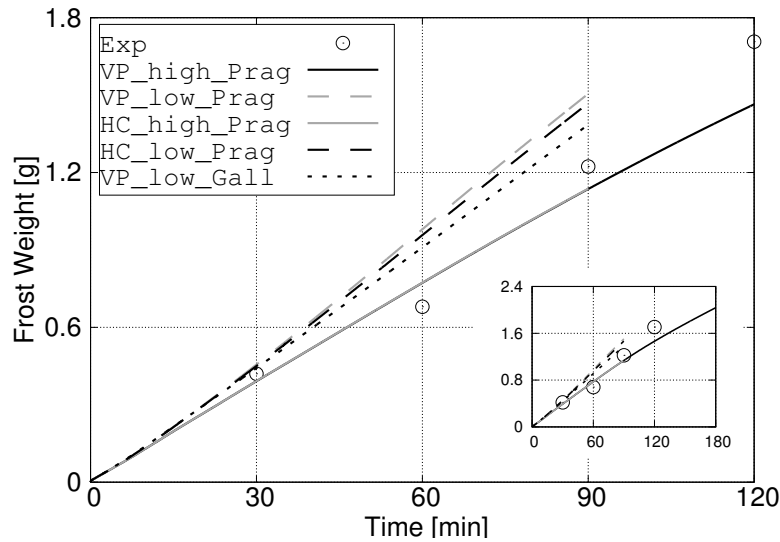
Figure 3.11: Frost weight evolution with time.

Differences arise when using different values of the Darcian source term constant C. Lower C-values mean less resistance exerted by the frost layer on the air flow, which allows more water vapour to soak into it. As a consequence, larger deposition rates are found (e.g., note the slope differences between cases VP_high_Prag and VP_low_Prag, or cases HC_high_Prag and HC_low_Prag, shown in Fig. 3.11). Moreover, note that the corresponding thickness profiles given in Fig. 3.10 bring out that lower values of C not only let larger water vapour deposition, but also the fact that the densification along the duct is distributed differently (see Figs. 3.12a and 3.12b). Higher deposition rates are found in the upstream region ($x < 50$ mm) due to the fact that more vapour is penetrating the frost layer. Thus enlarging the drop of the bulk moisture in the first 60 mm in the streamwise direction, which at the same time leads to a lower deposition in the downstream region ($x > 60$ mm) because of the reduced amount of the transported water vapour.

On the other hand, larger differences are found among the thickness distributions whenever using enhanced diffusion resistance factors (see cases VP_low_Prag and VP_low_Gall depicted in Figs. 3.10, 3.12b and 3.12c). The enhanced water vapor diffusivity lets a larger part of the vapour impinging the frost surface to diffuse into the frost sheet, which otherwise would remain in the cells close to the frost surface.

The porosity distributions shown in Figs.3.12 and 3.15 show that the densification occurs mainly close to the inlet, where higher gradients are located because of the

(a) VP_high_Prag

(b) VP_low_Prag

(c) VP_low_Gall
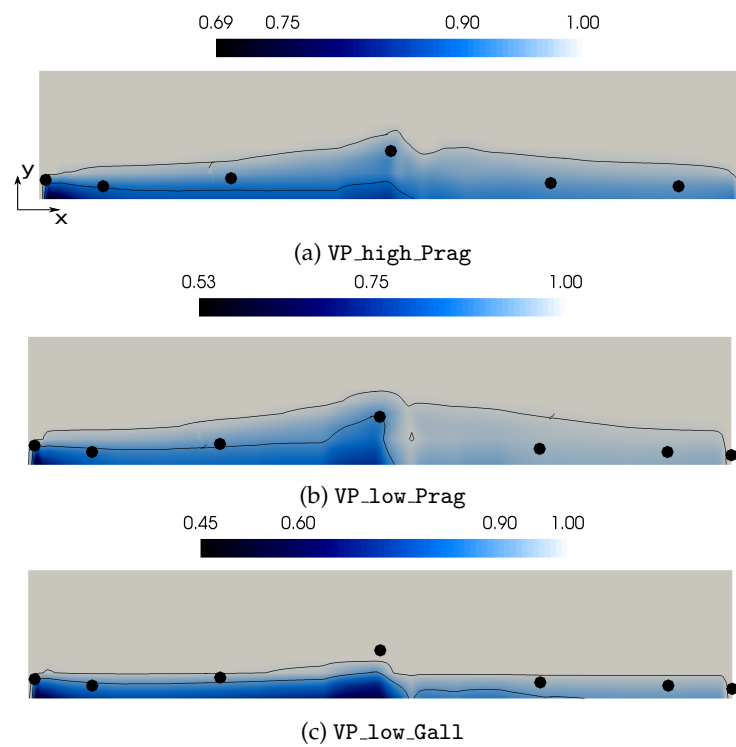
Figure 3.12: Porosity distributions, and contours of ε_v at 0.9 and 0.99 at 60 min. Circles correspond to the experimental frost thickness values [27]. The image scaling is x :1:5, y :1:1.

(a) VP_high_Prag

(b) VP_low_Prag

(c) VP_low_Gall
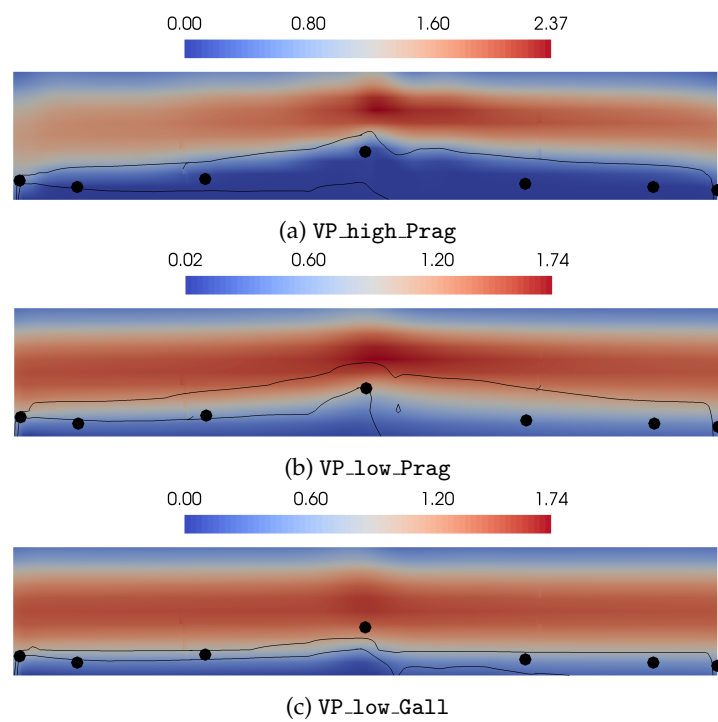
Figure 3.13: Velocity fields in m/s, and contours of ε_v at 0.9 and 0.99 at 60 min. Circles correspond to the experimental frost thickness values [27]. The image scaling is x :1:5, y :1:1.

(a) VP_high_Prag

(b) VP_low_Prag

(c) VP_low_Gall

Figure 3.14: Temperature distributions in K, and contours of ε_v at 0.9 and 0.99 at 60 min. Circles correspond to the experimental frost thickness values [27]. The image scaling is x :1:5, y :1:1.

(a) 30 min

(b) 60 min

(c) 90 min

(d) 120 min

(e) 150 min

(f) 180 min

Figure 3.15: Porosity ditributions of `VP_high_Prag`. Contours of ε_v at 0.9 and 0.99. Circles correspond to the experimental frost thickness values [27]. The image scaling is x :1:5, y :1:1.
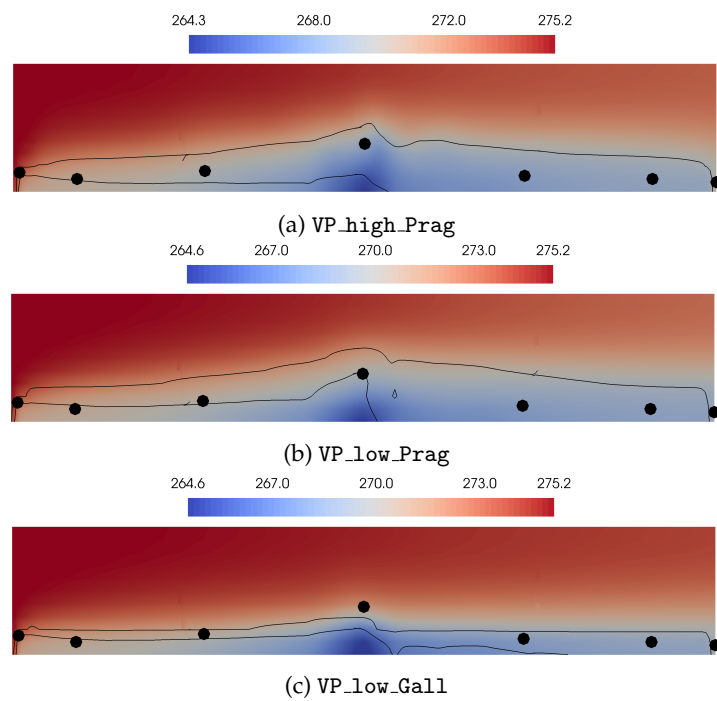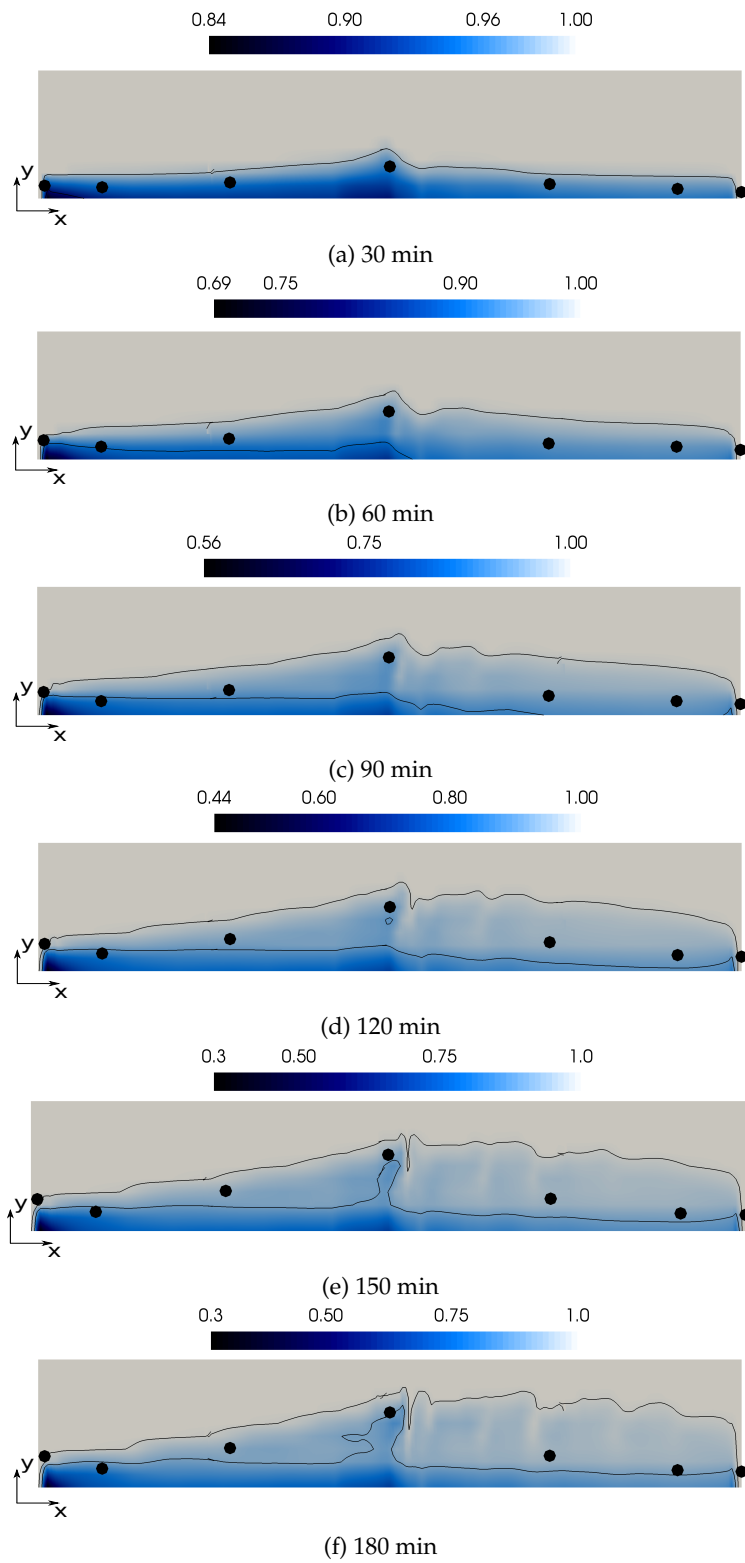
uniform inflow boundary condition, as well as the central region, where lower wall temperatures are set. It has also been noted an increase of the porosity at certain locations in the downstream region (beginning at $x \approx 60$ mm) observed only in advanced states of case `VP_high_Prag`, starting from 120 min onwards, in Fig.3.15. The origin of such effect, which might be numerical, is unclear. Further simulations using denser meshes might give an explanation to it.

In addition, notice how the bulk temperature shown in Fig.3.14 decreases because of the contact with the lower boundary, as well as how the increased thermal conductivity within the frost sheet allows the cold temperatures to propagate throughout the layer.

The velocity fields shown in Fig.3.13 indicate that convection within the range $\varepsilon_v \in [0.9 - 0.99]$ becomes less important when increasing the value of the constant C, as seen by the close to zero velocity values observed in that region. Indeed, the larger the C-value is, the bigger is the region with high porosity values, fact that agrees qualitatively to the solutions without convection obtained in [18].

3.5.2 Discussion

Despite the fact that using non-artificially increased diffusion resistance factors, i.e. Prager's correlation, lead to overall overpredicted growths (see Fig.3.10), it has been verified that the value of the constant C regulates the local densification. It is observed that the low C-values tested induce larger densifications in the upstream region ($x < 50$ mm), allowing a lower amount of water vapour to deposit on the downstream region ($x > 60$ mm). On the contrary, the large C-values tested allow a more homogeneous deposition of water vapor. Thus, keeping a larger amount in the dowstream region, which translates into higher growths. Regardless of the shifted solution of the air-frost interface when using Prager's diffusivity, the thickness distributions obtained when using the low C-values agree better to the experimental data. Recall that despite we are using a constant value for C, it likely has a dependance on the particle diameter, as for example, $\sim 1/d_p^2$ as given in Eq. 3.16. In more porous regions (that is, close to the frost-air surface), one should expect lower values of d_p. The lack of such data within the frost layer highlights the actual need to perform experiments aiming to study the internal morphology.

On the other hand, it has been observed that the usage of artificially increased diffusion resistance factors (Le Gall *et al.* [16] with an F factor of 5) promote the densification of the frost layer in exchange of its growth. The solution of case `VP_low_Gall` underpredicts the growth. Hence, given the tested mesh, one should expect better agreements when using lower values of F.

As a conclusion, the source term of the momentum equation regulates, in a way, where the densification will be held, as well as the shape of the air-frost interface. Whereas enhancing the diffusion resistance factor regulates the rate of growth. It

seems that enhanced diffusion resistance factors are needed to match the experimental data, although with smaller enhancements than the ones used in [18], which would prove that the convective effects play a role within the frost layer. However, despite convection should be included in the model, the need of using a $\mu > 1$ means that the latter is not accounting for other physical effects that are being taken place within the frost layer (see [16, 18, 40]).

3.6   Conclusions

The presented model accounts for the appearance, growth and densification of frost. The model is based on a finite volume approach which uses a fixed grid. A single set of equations is set both for the free air and the frost layer, where the thermophysical properties are dynamically adapted for each region and where phase changes are triggered by the thermophysical state of the cells. To the best of the author's knowledge, this is the first attempt to model frosting by means of the VANS equations.

The capabilities of the numerical model have been tested in a channel flow with a non-homogeneously cooled lower boundary, previously studied experimentally by Kwon *et al.* [27]. In particular, the studied parameters include the porosity model used to calculate the convection outside and within the frost layer, the magnitude of the Darcian coefficient that causes the damping of the velocity field within the porous medium, and the enhancement of the diffusion resistance factors.

Results show that using Darcian coefficient values such that convection is allowed at the high porosity regions ($\varepsilon_v > 0.9$), imply a more accurate capture of the local densification of the frost sheet. Moreover, it has been verified that whenever allowing convection within the frost layer, the artificial enhancement of the diffusion resistance factor needs to be reduced compared to a case where no convection is allowed [18], fact that confirms the idea that convective effects play a significant role in high porosity regions. Further simulations using denser meshes should be carried out to find the best combination of the input parameters of the model, such as the frost layer conductivity, the diffusion resistance factor, and the momentum source term coefficient, in order to provide more accurate predictions of the phenomenon.

Notwithstanding the fact that one could set up a numerical model able to reproduce the growth of the frost layer by optimizing the empirical and numerical inputs, it is essential to further encourage experimental research to tackle the internal processes of frost sheets. Specifically, from a macroscopical point of view, the ones related to the effective diffusivity and the particle diameter dependency of the Darcian coefficient.

References

[1] Olivier Parent and Adrian Ilinca. Anti-icing and de-icing techniques for wind turbines: Critical review. *Cold regions science and technology*, 65(1):88–96, 2011.

[2] Kripa K Varanasi, Tao Deng, J David Smith, Ming Hsu, and Nitin Bhate. Frost formation and ice adhesion on superhydrophobic surfaces. *Applied Physics Letters*, 97(23):234102, 2010.

[3] Saurabh Nath, S Farzad Ahmadi, and Jonathan B Boreyko. A review of condensation frosting. *Nanoscale and Microscale Thermophysical Engineering*, 21(2):81–101, 2017.

[4] Kwan-Soo Lee, Sung Jhee, and Dong-Keun Yang. Prediction of the frost formation on a cold flat surface. *International Journal of Heat and Mass Transfer*, 46(20):3789–96, September 2003.

[5] Y.B. Lee and S.T. Ro. Analysis of the frost growth on a flat plate by simple models of saturation and supersaturation. *Experimental Thermal and Fluid Science*, 29(6):685–96, July 2005.

[6] Byeongchul Na and Ralph L. Webb. New model for frost growth rate. *International Journal of Heat and Mass Transfer*, 47:925–36, 2004.

[7] Christian JL Hermes, Robson O Piucco, Jader R Barbosa, and Cláudio Melo. A study of frost growth and densification on flat surfaces. *Experimental Thermal and Fluid Science*, 33(2):371–379, 2009.

[8] Amne El Cheikh and Anthony Jacobi. A mathematical model for frost growth and densification on flat surfaces. *International Journal of Heat and Mass Transfer*, 77:604–11, 2014.

[9] Max Kandula. Frost growth and densification in laminar flow over flat surfaces. *International Journal of Heat and Mass Transfer*, 54:3719–31, 2011.

[10] Donghee Kim, Chiwon Kim, and Kwan-Soo Lee. Frosting model for predicting macroscopic and local frost behaviors on a cold plate. *International Journal of Heat and Mass Transfer*, 82:135–142, 2015.

[11] Bernard Frankovic Kristian Lenic, Anica Trp. Transient two-dimensional model of frost formation on a fin-and-tube heat exchanger. *International Journal of Heat and Mass Transfer*, 52:22–32, 2009.

[12] JM Armengol, CT Salinas, J Xaman, and KAR Ismail. Modeling of frost formation over parallel cold plates considering a two-dimensional growth rate. *International Journal of Thermal Sciences*, 104:245–256, 2016.

[13] Chiwon Kim, Jaehwan Lee, and Kwan-Soo Lee. Numerical modeling of frost growth and densification on a cold plate using frost formation resistance. *International Journal of Heat and Mass Transfer*, 115:1055–1063, 2017.

[14] B.W. Jones and J.D. Parker. Frost formation with varying environmental parameters. *Journal of Heat Transfer*, 97(2):255–259, 1975.

[15] Y.-X. Tao, R.W. Besant, and K.S. Rezkallah. A mathematical model for predicting the densification and growth of frost on a flat plate. *International Journal of Heat and Mass Transfer*, 36(2):353–63, 1993.

[16] R. Le Gall, J.M. Grillot, and C. Jallut. Modelling of frost growth and densification. *International Journal of Heat and Mass Transfer*, 40(13):3177–87, 1997.

[17] Simon Ellgas and Michael Pfitzner. Modeling frost formation within a commercial 3-d cfd code. *Numerical Heat Transfer, Part A: Applications*, 53(5):485–506, 2007.

[18] Eduard Bartrons, Carles Oliet, Enrique Gutiérrez, Alireza Naseri, and Carlos David Pérez-Segarra. A finite volume method to solve the frost growth using dynamic meshes. *International Journal of Heat and Mass Transfer*, 124:615–628, 2018.

[19] J Cui, WZ Li, Y Liu, and ZY Jiang. A new time- and space-dependent model for predicting frost formation. *Applied Thermal Engineering*, 31:447–457, 2011.

[20] Xiaomin Wu, Qiang Ma, Fuqiang Chu, and Shan Hu. Phase change mass transfer model for frost growth and densification. *International Journal of Heat and Mass Transfer*, 96:11–19, 2016.

[21] Xiaomin Wu, Fuqiang Chu, and Qiang Ma. Frosting model based on phase change driving force. *International Journal of Heat and Mass Transfer*, 110:760–767, 2017.

[22] Eduard Bartrons, PA Galione, Giorgos Papakokkinos, and Carles D Pérez-Segarra. Fixed-grid numerical modeling of frost formation. In *23rd AIAA Computational Fluid Dynamics Conference*, page 4505, 2017.

[23] PA Galione, O Lehmkuhl, J Rigola, and A Oliva. Fixed-grid modeling of solid-liquid phase change in unstructured meshes using explicit time schemes. *Numerical Heat Transfer, Part B: Fundamentals*, 65(1):27–52, 2014.

[24] PA Galione, O Lehmkuhl, J Rigola, and A Oliva. Fixed-grid numerical mod-
     eling of melting and solidification using variable thermo-physical properties–
     application to the melting of n-octadecane inside a spherical capsule. *International
     Journal of Heat and Mass Transfer*, 86:721–743, 2015.

[25] CT Hsu and P Cheng. Thermal dispersion in a porous medium. *International
     Journal of Heat and Mass Transfer*, 33(8):1587–1597, 1990.

[26] Vaughan R Voller and C Prakash. A fixed grid numerical modelling methodology
     for convection-diffusion mushy region phase-change problems. *International
     Journal of Heat and Mass Transfer*, 30(8):1709–1719, 1987.

[27] Jeong-Tae Kwon, Hyo Jae Lim, Young-Chul Kwon, Shigeru Koyama, Dong-Hwi
     Kim, and Chieko Kondou. An experimental study on frosting of laminar air
     flow on a cold surface with local cooling. *International Journal of Refrigeration*,
     29(5):754–760, 2006.

[28] Stephen Whitaker. The forchheimer equation: a theoretical development. *Trans-
     port in Porous media*, 25(1):27–61, 1996.

[29] WP Breugem and DAS Rees. A derivation of the volume-averaged boussinesq
     equations for flow in porous media with viscous dissipation. *Transport in porous
     media*, 63(1):1–12, 2006.

[30] Arghya Samanta, Ricardo Vinuesa, Iman Lashgari, Philipp Schlatter, and Luca
     Brandt. Enhanced secondary motion of the turbulent flow through a porous
     square duct. *Journal of Fluid Mechanics*, 784:681–693, 2015.

[31] Marco E Rosti, Luca Cortelezzi, and Maurizio Quadrio. Direct numerical simu-
     lation of turbulent channel flow over porous walls. *Journal of Fluid Mechanics*,
     784:396–442, 2015.

[32] E Bartrons, CD Perez-Segarra, and C Oliet. Frost formation: Optimizing solutions
     under a finite volume approach. In *Journal of Physics: Conference Series*, volume
     745, page 032062. IOP Publishing, 2016.

[33] H Auracher. Water vapour diffusion and frost formation in capillaries. In *Bulletin
     of the International Institute of Refrigeration*, pages 477–88, 1972.

[34] R.E. Cunningham and R.J.J. Williams. *Diffusion in Gases and Porous Media*. New
     York: Plenum Press, 1980.

[35] T. E. Fessler. *WETAIR - a computer code for calculating thermodynamic and transport
     properties of air-water mixtures*, volume Tech. Report 1466. NASA, 1979.

[36] Termo fluids s.l., webpage: www.termofluids.com.

[37] J. Muela. *Modelling and numerical simulation of combustion and multi-phase flows using finite volume methods on unstructured meshes*. PhD thesis, Universitat Politècnica de Catalunya, 2018.

[38] Jean-Luc Guermond, Peter Minev, and Jie Shen. An overview of projection methods for incompressible flows. *Computer methods in applied mechanics and engineering*, 195(44):6011–6045, 2006.

[39] *ASHRAE Handbook Fundamentals*. American Society of Heating, Refrigerating and Air-conditioning Engineers, Inc., si edition edition, 2009.

[40] Z. Yosida. Physical studies on deposited snow. i: Thermal properties. *Contributions from the Institute of Low Temperature Science*, 7(7):19–74, 1955.

4

Concluding remarks

The main objective of the thesis is to model the frost growth and densification of macroscopic frost sheets. Two finite volume models have been developed.

The first one, introduced in Chapter 2, uses a deformable mesh that emulates the growing frost layer. Implicit schemes are used for the energy and water vapour transport, and the heat and mass transfer coefficients are evaluated by means of empirical correlations.

Due to the large number of available frost layer conductivity and frost effective diffusivity correlations, parametric studies are carried out aiming to find optimum combinations that ensure best captures of the phenomena. It is observed that the combinations of the model empirical inputs which ensure best fits are dependent on the environmental conditions. Indeed, temperature and pressure are two key parameters that define the type of crystal which will be formed. Hence, the morphology of the frost sheet.

Results show that artificially enhanced diffusion resistance factors (larger than 1.0) need to be used at the high porosity regions, where $\varepsilon_v \geq 0.9$, in order to capture the frost growth and densification patterns. Due to the fact that a significant part of the frost layer has such values, a new insight is put forward in regards of attributing the water vapour transport inside the frost layer not only to Fickian diffusion, but also to the convective effects involved in it.

Finally, the model is tested on a bidimensional case with a non-homogeneous temperature at the wall. Notwithstanding the fact that the external flow is not being solved in detail, solutions show reasonable agreement with experimental data, proving the dynamic mesh method to be a valid candidate to simulate frost growth.

The need to understand possible reasons behind using enhanced diffusion resistance factors lead to the fixed grid model introduced in Chapter 3, in which the velocity field within the frost layer is calculated. The presented model accounts for the appearance, growth and densification of frost. A single set of equations is set both for the free air and the frost layer, where the thermophysical properties are dynamically adapted for each region, and where phase changes are triggered by the

thermophysical state of the cells.

The capabilities of the numerical model are tested in a duct flow with a non-homogeneously cooled lower boundary. A comparison of the velocity field solution within the frost sheet is carried out by means of two porous media models. Moreover, the damping of the velocity field inside the porous medium is studied by means of the magnitude of the Darcian coefficient. Furthermore, tests involving enhancement of the diffusion resistance factors are also performed.

Results show that using Darcian coefficient values such that convection is allowed at the high porosity regions ($\varepsilon_v > 0.9$), imply a more accurate capture of the local densification of the frost sheet. Moreover, it has been verified that whenever allowing convection within the frost layer, the artificial enhancement of the diffusion resistance factor needs to be reduced compared to a case where no convection is allowed [?], fact that confirms the idea that convective effects play a significant role in high porosity regions.

Despite all the efforts to develop models that are able to reproduce the growth and densification of the frost layer, the diverse nature of the crystal shapes and sizes pose a complexity that is yet to be accounted by the frost layer empirical correlations. From a macroscopical point of view, specially the ones related to the effective diffusivity and the particle diameter dependency of the Darcian coefficient.

5
_____

Future actions

The work carried out during the past four years constitutes a robust foundation which allows with some contributions to bring the Group to the vanguard of the simulations of macroscopic frost sheets for industrial applications. In this section, the short-term contributions, as well as some major improvements which can be dealt with in the long run, are explained in detail.

5.1   Short-term actions

This work has provided two numerical models capable to solve complex geometries. Each of them can be improved to tackle complex industrial applications.

The empirical inputs needed to solve the frost growth, i.e. the frost layer conductivity and the effective diffusivity, have been optimized for a litmited number of experimental conditions (see Sec. 2.5) by means of parametric studies which minimize the discrepancy between the numerical solution and the experimental data. In order to find an even more accurate set of empirical inputs for a given numerical experiment, such as the genetic algorithms library developed by Imanol [1], should be implemented.

In regards of the moving mesh method, the frost domain can be coupled with another mesh accounting for the fluid. The coupling between the two meshes would be located at the air-frost interface. Thanks to the fact that the fluid will be solved accurately, the empirical correlations accounting for the heat and mass transfer coefficients will no longer be needed. Special attention will be put on maximizing the implicit time step of both fluid and frost which, because of the multi-scale nature of the problem, might differ. Hence, a certain amount of subtime steps might be needed before communicating data (i.e. frost growth displacements, temperature and water vapour density gradients) among them.

On the other hand, the fixed grid method can be modified by changing the present explicit, or semi-implicit schemes, towards fully-implicit schemes. As a consequence,

larger time steps would be reached, which would allow solving a problem with much finer meshes.

Finally, the mesh where the frost growth is being simulated can be coupled with a solid domain. Heat conduction can be calculated inside the solid domain, thus accounting for the heat transfer conjugate problem (e.g. fin and tube heat exchangers, cold soaked fuel frost on aircrafts) [2,3]. In addition, the group's radiation solver [4], implemented and validated in *TermoFluids*, should be added in order to account for the nocturnal frost due to radiative cooling, i.e. the ice formed on aircraft wings or wind turbines during cloudless nights.

5.2   Mid- to long-term actions

On the one hand, the velocity field within the frost layer should be computed in order to have an improved solution of the frost growth using the moving mesh method. A boundary condition at the air-frost interface should be developed in order to transfer the velocities calculated at the fluid side of the frost-air interface to the frost domain. Given the velocities at the boundaries of the frost, a porous media treatment should be implemented in order to compute the fluid motion within the frost layer.

On the other hand, a long-term action regarding the fixed grid method consists in accounting for condensation and melting phenomena. Indeed, we are far from accurately solving such phase changes, due to the fact that liquid water cannot be considered still (as it is done with ice, whose velocity is considered zero). The water phase would be accounted by a volume fraction. A single-fluid approach using the Level-set method [5–7] with added source terms accounting for the appearance or destruction of the liquid water phase, would allow tracking the motion of the unconnected portions of liquid water being formed. Furthermore, adding a contact angle treatment [8] to the air-water-ice interfaces would give even more accurate solutions. Nevertheless, because the Level-set methods are time explicit, physical problems of the order of hours would not yet be possible to simulate.

Accounting for the condensation would not only allow simulating the environmental conditions that trigger the formation of water droplets at the cold surface during the initial stages of frosting, but also, and most important, the fact of accounting for the melting of the frost surface once it reaches the melting point. Hence, the cycle process of the penetration of that liquid water into the frost layer, with a later solidification.

References

[1] I. Aizpurua-Udabe. *Parallel optimization algorithms for high performance computing. Application to thermal systems*. PhD thesis, Universitat Politècnica de Catalunya, 2017.

[2] Joan Lopez. *Parallel object-oriented algorithms for simulation of multiphysics : application to thermal systems*. PhD thesis, Universitat Politècnica de Catalunya, 2016.

[3] Giorgos Papakokkinos, Eduard Bartrons, Joan Farnós, Jesús Castro, and Assensi Oliva. A computational model based on parallelizable unstructured meshes for the simulation of the conjugate phenomena in the adsorption reactor. In *International Sorption Heat Pump Conference*, Tokyo, Japan, 7-10 August 2017.

[4] G. Colomer. *Numerical methods for radiative heat transfer*. PhD thesis, Universitat Politècnica de Catalunya, 2006.

[5] Néstor Balcázar, Lluís Jofre, Oriol Lehmkuhl, Jesús Castro, and Joaquim Rigola. A finite-volume/level-set method for simulating two-phase flows on unstructured grids. *International journal of multiphase flow*, 64:55–72, 2014.

[6] Néstor Balcázar, Joaquim Rigola, Jesús Castro, and Assensi Oliva. A level-set model for thermocapillary motion of deformable fluid particles. *International Journal of Heat and Fluid Flow*, 62:324–343, 2016.

[7] E Gutiérrez, N Balcazar, E Bartrons, and J Rigola. Numerical study of taylor bubbles rising in a stagnant liquid using a level-set/moving-mesh method. *Chemical Engineering Science*, 164:158–177, 2017.

[8] Mark Sussman. An adaptive mesh algorithm for free surface flows in general geometries. *Adaptive method of lines*, pages 207–231, 2001.

Moving the mesh

The implemented moving mesh method that allows deformations of the frost domain is here explained.

The mesh is assumed to be elastic. The linear momentum conservation equation computed at each time step reads as:

$$\frac{\mathrm{D}}{\mathrm{D}t}\int_V \rho v dV \nearrow^0 = \oint_S \vec{n} \cdot \boldsymbol{\sigma} dS + \int_V \rho \boldsymbol{f}_b dV \nearrow^0$$

where inertial and body forces are neglected.

A.1 Constitutive law

The constitutive equations of a linear, elastic and homogeneous continuum are the Lamé-Hooke equations. In the particular case of small deformations, the stress tensor can be written as follows:

$$\boldsymbol{\sigma} = 2\mu\epsilon + \lambda \mathrm{tr}\left(\epsilon\right)\mathbb{I}$$

where μ and λ are the Lamé coefficients, which can be expressed as a function of Young's modulus and Poisson's ratio. In addition, the infinitessimal strain tensor ϵ reads as:

$$\epsilon = \frac{1}{2}\left(\nabla\vec{u} + (\nabla\vec{u})^T\right)$$

where $\vec{u}$ represents the displacements.

A.2 Boundary Conditions

Two main boundary conditions are implemented: Dirichlet (fixed displacement $\vec{u}_B$) and Neumann ($\vec{n} \cdot (\nabla\vec{u}) = 0$) type boundary conditions.

The present study uses Dirichlet type boundary conditions at the wall (with $\vec{u}_B = 0$) and at the frost surface. The side walls use a $\vec{u}_B = 0$ condition in the streamwise direction, and Neumann boundary condition in the other two directions. Periodic walls use a $\vec{u}_B = 0$ in the spanwise direction, and Neumann boundary condition in the other two directions.

A.3   Discretization

The momentum equation previously introduced can be written in terms of the displacements using the constitutive law.

$$\oint_S (2\mu + \lambda)\, \vec{n} \cdot \nabla \vec{u}\, dS = \oint_S \vec{n} \cdot \left(\mu \left(\nabla \vec{u}\right)^T + \lambda \mathrm{tr}\left(\nabla \vec{u}\right) \mathbb{I} - \left(\mu + \lambda\right) \nabla \vec{u} \right) dS$$

The left-hand side term, also known as the Laplacian term, is solved implicitly using a central difference scheme with a non-orthogonal correction. On the other hand, the right-hand side term is treated explicitly, and where cell gradients are evaluated by means of a least squares method. The schemes implemented in both sides of the equation ensure second-order accuracy.

A.4   Mesh update

Since the model uses a cell-centered finite volume method and the mesh movement is accomplished by updating the vertices, an interpolating function which translates displacements at the cell nodes to displacements at the vertices.

$$\vec{u}_p = \frac{\sum_c \omega_{\mathrm{pc}} \left[\vec{u}_c + \left(\vec{r}_p - \vec{r}_c\right) \cdot \left(\nabla \vec{u}\right)_c \right]}{\sum_c \omega_{\mathrm{pc}}}$$

where p indicates the point where the displacement is interpolated, and c represents the nodes (or cell centers) whose corresponding cell contains point p. The weighting factor ω_{pc} is:

$$\omega_{\mathrm{pc}} = \frac{1}{\|\vec{r}_p - \vec{r}_c\|}$$

Note that $\vec{u}_c$ is equivalent to the δy defined in Eq. 2.28.

Formulation differences

A special interest of the authors arose from the fact that the most commonly used sets of water vapour transport and energy equations found in the literature, namely the ones put forward by Tao *et al.* [1] and Le Gall *et al.* [2], and Na and Webb [3], seemed to differ from the set developed and implemented in the present study (see Eqs. 3.3 and 3.4). This section focuses on finding such differences, aiming to give clarity among them. First, the two formulations are presented. Then, the water vapour transport and the energy equations presented in this study are rearranged in order to match the terms of the other two formulations.

B.1 Most commonly used formulations

Tao *et al.* [1] and Le Gall *et al.* [2] stated:

$$\dot{m} + \frac{\partial \left(\rho_v \varepsilon_v \right)}{\partial t} = \nabla \cdot \left(D_{\text{eff}} \nabla \rho_v \right) \tag{B.1}$$

$$\nabla \cdot \left(\lambda_m \nabla T \right) + L_{\text{sv}} \dot{m} = \rho_{\text{fl}} c_{p,\text{fl}} \frac{\partial T}{\partial t} \tag{B.2}$$

Where $\dot{m} = \partial(\rho_i \varepsilon_i)/\partial t$. The effective diffusivity is defined as $D_{\text{eff}} \equiv \mu D_v$, and L_{sv} corresponds to the latent heat of sublimation. Later on, Na and Webb [3] proposed the following set of equations:

$$\frac{\partial \rho_{\text{fl}}}{\partial t} = \nabla \cdot \left(D_{\text{eff}} \rho_{\text{ha}} \nabla \left(\rho_v / \rho_{\text{ha}} \right) \right) \tag{B.3}$$

$$\nabla \cdot \left(\lambda_m \nabla T \right) + L_{\text{sv}} \frac{\partial \rho_{\text{fl}}}{\partial t} = \rho_{\text{fl}} c_{p,\text{fl}} \frac{\partial T}{\partial t} \tag{B.4}$$

B.2   The vapour transport equations

Tao's and Le Gall's Eq. B.1 can be easily compared to the general form of the vapour transport equation given in Eq. 3.3. Both equations match when ρ_{ha} is considered constant, so $\rho_{ha}D_{eff}\nabla Y_v \approx D_{eff}\nabla \rho_v$, and the convective term is neglected.

On the other hand, developing the LHS term of Na and Webb's Eq. B.3:

$$\frac{\partial \rho_{fl}}{\partial t} = \frac{\partial (\rho_v \varepsilon_v)}{\partial t} + \frac{\partial (\rho_i \varepsilon_i)}{\partial t} + \frac{\partial (\rho_{da}\varepsilon_v)}{\partial t} \tag{B.5}$$

From where an extra term, $\partial (\rho_{da}\varepsilon_v)/\partial t$, is being accounted. Note that depending on the value of the porosity, the former is between 2 and 3 orders of magnitude smaller than $\partial (\rho_i\varepsilon_i)/\partial t$.

B.3   The energy equations

In the following, a reference state of water in its solid state at a temperature T_{ref} is used, tipically $273.15K$.

Multiplying all terms of Eq. 3.3 by L_{sv}:

$$L_{sv}\nabla \cdot (\rho_v \vec{u}) = L_{sv}\nabla \cdot (\rho_{ha}D_{eff}\nabla Y_v) - L_{sv}\frac{\partial (\varepsilon_v \rho_v + (1-\varepsilon_v)\rho_i)}{\partial t} \tag{B.6}$$

Separating h_{ha} from the convective term of Eq. 3.4 in its sensible ($h_{ha,sens}$) and latent (L_{sv}) parts:

$$\frac{\partial}{\partial t}(\rho_m h_m) + \nabla \cdot (\rho_{ha}h_{ha,sens}\vec{u}) + L_{sv}\nabla \cdot (\rho_v \vec{u}) = \nabla \cdot (\lambda_m \nabla T)$$
$$+ \nabla \cdot [(h_v - h_{da})\rho_{ha}D_{eff}\nabla Y_v] \tag{B.7}$$

Substituting Eq. B.6 into Eq. B.7:

$$\frac{\partial}{\partial t}(\rho_m h_m) - L_{sv}\frac{\partial (\varepsilon_v \rho_v + (1-\varepsilon_v)\rho_i)}{\partial t} + \nabla \cdot (\rho_{ha}h_{ha,sens}\vec{u}) = \nabla \cdot (\lambda_m \nabla T)$$
$$+ \nabla \cdot [(h_v - h_{da})\rho_{ha}D_{eff}\nabla Y_v] - L_{sv}\nabla \cdot (\rho_{ha}D_{eff}\nabla Y_v) \tag{B.8}$$

Expressing $\rho_m h_m$ as $\rho_m h_m = \rho_{ha}\varepsilon_v h_{ha,sens} + \rho_v \varepsilon_v L_{sv} + \rho_i (1-\varepsilon_v)h_{i,sens}$ and rearranging the first two LHS terms of Eq. B.8:

$$\frac{\partial (\rho_{ha}\varepsilon_v h_{ha,sens} + \rho_i (1-\varepsilon_v)h_{i,sens})}{\partial t} - L_{sv}\frac{\partial (\rho_i (1-\varepsilon_v))}{\partial t} + \nabla \cdot (\rho_{ha}h_{ha,sens}\vec{u}) =$$
$$\nabla \cdot (\lambda_m \nabla T) + \nabla \cdot [(h_v - h_{da})\rho_{ha}D_{eff}\nabla Y_v] - L_{sv}\nabla \cdot (\rho_{ha}D_{eff}\nabla Y_v) \tag{B.9}$$

Applying some chain derivatives to the first LHS term of Eq. B.9, and assuming $dh_{\text{sens}} = c_p dT$ only for the humid air:

$$\left[\rho_{\text{ha}}\varepsilon_v c_{p,\text{ha}}\frac{\partial T}{\partial t} + \rho_i\left(1-\varepsilon_v\right)c_{p,i}\frac{\partial T}{\partial t}\right] + h_{\text{ha,sens}}\frac{\partial\left(\rho_{\text{ha}}\varepsilon_v\right)}{\partial t} + h_{i,\text{sens}}\frac{\partial\left(\rho_i\left(1-\varepsilon_v\right)\right)}{\partial t}$$
$$-L_{\text{sv}}\frac{\partial\left(\rho_i\left(1-\varepsilon_v\right)\right)}{\partial t} + \nabla\cdot\left(\rho_{\text{ha}}h_{\text{ha,sens}}\vec{u}\right) =$$
$$\nabla\cdot\left(\lambda_m\nabla T\right) + \nabla\cdot\left[\left(h_v - h_{\text{da}}\right)\rho_{ha}D_{\text{eff}}\nabla Y_v\right] - L_{\text{sv}}\nabla\cdot\left(\rho_{\text{ha}}D_{\text{eff}}\nabla Y_v\right)$$
$$(B.10)$$

Identifying $\rho_{\text{fl}}c_{p,\text{fl}}\partial T/\partial t$, using the equalty $\varepsilon_i = 1 - \varepsilon_v$, and rearranging the terms:

$$\rho_{\text{fl}}c_{p,\text{fl}}\frac{\partial T}{\partial t} + \nabla\cdot\left(\rho_{\text{ha}}h_{\text{ha,sens}}\vec{u}\right) + h_{\text{ha,sens}}\frac{\partial\left(\rho_{\text{ha}}\varepsilon_v\right)}{\partial t} =$$
$$\left(L_{\text{sv}} - h_{i,\text{sens}}\right)\frac{\partial\left(\rho_i\varepsilon_i\right)}{\partial t} + \nabla\cdot\left(\lambda_m\nabla T\right) \qquad (B.11)$$
$$+\nabla\cdot\left[\left(h_v - h_{\text{da}}\right)\rho_{ha}D_{\text{eff}}\nabla Y_v\right] - L_{\text{sv}}\nabla\cdot\left(\rho_{\text{ha}}D_{\text{eff}}\nabla Y_v\right)$$

Rewriting the convective term as $\nabla\cdot\left(\rho_{\text{ha}}h_{\text{ha,sens}}\vec{u}\right) = h_{\text{ha,sens}}\nabla\cdot\left(\rho_{\text{ha}}\vec{u}\right) + \rho_{\text{ha}}\vec{u}\cdot\nabla h_{\text{ha,sens}}$ and using the humid air mass conservation equation, which reads as:

$$\frac{\partial\left(\rho_{\text{ha}}\varepsilon_v\right)}{\partial t} + \nabla\cdot\left(\rho_{\text{ha}}\vec{u}\right) = -\frac{\partial\left(\rho_i\varepsilon_i\right)}{\partial t} \qquad (B.12)$$

The following expression of the energy equation is obtained:

$$\rho_{\text{fl}}c_{p,\text{fl}}\frac{\partial T}{\partial t} + \rho_{\text{ha}}\vec{u}\cdot\nabla h_{\text{ha,sens}} = \left(L_{\text{sv}} + h_{\text{ha,sens}} - h_{i,\text{sens}}\right)\frac{\partial\left(\rho_i\varepsilon_i\right)}{\partial t} \qquad (B.13)$$
$$+\nabla\cdot\left(\lambda_m\nabla T\right) + \nabla\cdot\left[\left(h_v - h_{\text{da}}\right)\rho_{ha}D_{\text{eff}}\nabla Y_v\right] - L_{\text{sv}}\nabla\cdot\left(\rho_{\text{ha}}D_{\text{eff}}\nabla Y_v\right)$$

Now, separating the water vapor enthalpy by its sensible and latent parts, and rewriting the gradient of humid air enthalpy in terms of the temperature:

$$\rho_{\text{fl}}c_{p,\text{fl}}\frac{\partial T}{\partial t} + \rho_{\text{ha}}c_{p,\text{ha}}\vec{u}\cdot\nabla T = \left(L_{\text{sv}} + h_{\text{ha,sens}} - h_{i,\text{sens}}\right)\frac{\partial\left(\rho_i\varepsilon_i\right)}{\partial t}$$
$$+\nabla\cdot\left(\lambda_m\nabla T\right) + \nabla\cdot\left[\left(h_{v,\text{sens}} + L_{\text{sv}} - h_{\text{da}}\right)\rho_{ha}D_{\text{eff}}\nabla Y_v\right] - L_{\text{sv}}\nabla\cdot\left(\rho_{\text{ha}}D_{\text{eff}}\nabla Y_v\right)$$
$$(B.14)$$

Finally, rewriting the gradient of the concentration in terms of the temperature, a final expression for the energy equation is obtained:

$$\rho_{\text{fl}}c_{p,\text{fl}}\frac{\partial T}{\partial t} + \rho_{\text{ha}}c_{p,\text{ha}}\vec{u}\cdot\nabla T = \left(L_{\text{sv}} + h_{\text{ha,sens}} - h_{i,\text{sens}}\right)\frac{\partial\left(\rho_i\varepsilon_i\right)}{\partial t}$$
$$+\nabla\cdot\left(\lambda_m\nabla T\right) + \nabla\cdot\left[\left(h_{v,\text{sens}} - h_{\text{da}}\right)\rho_{ha}D_{\text{eff}}\frac{\partial Y_v}{\partial T}\nabla T\right] \qquad (B.15)$$

Where:

$$(h_{v,\text{sens}} - h_{\text{da}}) \rho_{ha} D_{\text{eff}} \frac{\partial Y_v}{\partial T} = \rho_{ha} c_{p,\text{da}} D_{\text{eff}} \left(\frac{c_{p,v}}{c_{p,\text{da}}} - 1 \right) (T - T_{\text{ref}}) \frac{\partial Y_v}{\partial T} \qquad (B.16)$$

Given that the Lewis number is of the order of 1 for dry air, $\mathcal{O}(\lambda_m) \approx \mathcal{O}(\rho_{ha} c_{p,\text{da}} D_{\text{eff}})$ (inside the frost layer, λ_m would be one order higher). Moreover, $\mathcal{O}(c_{p,v}/c_{p,\text{da}} - 1) \approx 1$ and $\mathcal{O}((T - T_{\text{ref}}) \partial Y_v / \partial T) \approx 10^{-3}$. Overall, the second RHS term of Eq.B.15 is 4 orders of magnitude smaller than the first RHS term. Furthermore, one can observe that $\mathcal{O}(L_{\text{sv}}) = 2.6 \cdot 10^6$ and $\mathcal{O}(h_{\text{ha,sens}} - h_{i,\text{sens}}) \approx 10^3 - 10^4$.

Cancelling the low order terms and assuming a $\vec{u} \approx 0$ within the frost layer:

$$\rho_{\text{fl}} c_{p,\text{fl}} \frac{\partial T}{\partial t} = L_{\text{sv}} \frac{\partial (\rho_i \varepsilon_i)}{\partial t} + \nabla \cdot (\lambda_m \nabla T) \qquad (B.17)$$

From which Tao's and Le Gall's energy equation Eq. B.2 is found.

On the other hand, developing the term related to the released latent heat of Na and Webb's energy equation, Eq. B.4:

$$L_{\text{sv}} \frac{\partial \rho_{\text{fl}}}{\partial t} = L_{\text{sv}} \frac{\partial (\rho_{\text{ha}} \varepsilon_v)}{\partial t} + L_{\text{sv}} \frac{\partial (\rho_i \varepsilon_i)}{\partial t} \qquad (B.18)$$

From where an extra term, $L_{\text{sv}} \partial (\varepsilon_v \rho_{\text{ha}}) / \partial t$, is being considered. Note that depending on the value of the porosity, the former is between 2 and 3 orders of magnitude smaller than $L_{\text{sv}} \partial (\rho_i \varepsilon_i) / \partial t$.

B.4   Final comments

The formulation put forward by Tao *et al.* [1] and Le Gall *et al.* [2] arise from the original equations (Eqs.3.4 and 3.3) after applying certain simplifications. Those consist in neglecting the terms containing the velocity as well as the low-order-magnitude terms. Despite Na and Webb's [3] formulation seems less rigorous, it is possible that the fact of calculating one term less in the mass transport equation could make the computation more efficient.

References

[1] Y.-X. Tao, R.W. Besant, and K.S. Rezkallah. A mathematical model for predicting the densification and growth of frost on a flat plate. *International Journal of Heat and Mass Transfer*, 36(2):353–63, 1993.

[2] R. Le Gall, J.M. Grillot, and C. Jallut. Modelling of frost growth and densification. *International Journal of Heat and Mass Transfer*, 40(13):3177–87, 1997.

[3] Byeongchul Na and Ralph L. Webb. New model for frost growth rate. *International Journal of Heat and Mass Transfer*, 47:925–36, 2004.

Appendix C

Main publications in the context of this thesis

Journal Papers

- E. Bartrons, P. Galione and C-D. Pérez-Segarra, Fixed grid numerical modelling of frost growth and densification, *International Journal of Heat and Mass Transfer*, (under review).

- E. Bartrons, C. Oliet, E. Gutiérrez, A. Naseri and C.D. Pérez-Segarra, A finite volume method to solve the frost growth using dynamic meshes, *International Journal of Heat and Mass Transfer*, **124**, 615-628, 2018.

International Conference Papers

- E. Bartrons, P. Galione, G. Papakokkinos and C. D. Pérez-Segarra, Fixed-grid numerical modeling of frost formation, *23rd AIAA Computational Fluid Dynamics Conference*, 4505, 2017.

- E. Bartrons, C-D. Pérez-Segarra and C. Oliet, Frost Formation: Optimizing solutions under a finite volume approach, *Journal of Physics: Conference Series*, 745, 2016.